FLIGHT CONTROL SYSTEM DESIGN OF AN UNCOMMON QUADROTOR AERIAL VEHICLE

A THESIS SUBMITTED TO
THE GRADUATE SCHOOL OF NATURAL AND APPLIED SCIENCES
OF
MIDDLE EAST TECHNICAL UNIVERSITY

BY

MEHMET BASKIN

IN PARTIAL FULFILLMENT OF THE REQUIREMENTS
FOR
THE DEGREE OF DOCTOR OF PHILOSOPHY
IN
ELECTRICAL AND ELECTRONICS ENGINEERING

SEPTEMBER 2021

Approval of the thesis:

FLIGHT CONTROL SYSTEM DESIGN OF AN UNCOMMON QUADROTOR AERIAL VEHICLE

submitted by **MEHMET BASKIN** in partial fulfillment of the requirements for the degree of **Doctor of Philosophy in Electrical and Electronics Engineering Department, Middle East Technical University** by,

Prof. Dr. Halil Kalıpçılar
Dean, Graduate School of **Natural and Applied Sciences** _____

Prof. Dr. İlkay Ulusoy
Head of Department, **Electrical and Electronics Engineering** _____

Prof. Dr. Kemal Leblebicioğlu
Supervisor, **Electrical and Electronics Engineering, METU** _____

Examining Committee Members:

Prof. Dr. Mehmet Önder Efe
Computer Engineering, Hacettepe University _____

Prof. Dr. Kemal Leblebicioğlu
Electrical and Electronics Engineering, METU _____

Assoc. Prof. Dr. İlkay Yavrucuk
Aerospace Engineering, METU _____

Assist. Prof. Dr. Yakup Özkazanç
Electrical and Electronics Engineering, Hacettepe University _____

Assist. Prof. Dr. Mustafa Mert Ankaralı
Electrical and Electronics Engineering, METU _____

Date: 01.09.2021

I hereby declare that all information in this document has been obtained and presented in accordance with academic rules and ethical conduct. I also declare that, as required by these rules and conduct, I have fully cited and referenced all material and results that are not original to this work.

Name, Surname: Mehmet Baskın

Signature :

ABSTRACT

FLIGHT CONTROL SYSTEM DESIGN OF AN UNCOMMON QUADROTOR AERIAL VEHICLE

Baskın, Mehmet
Ph.D., Department of Electrical and Electronics Engineering
Supervisor: Prof. Dr. Kemal Leblebicioğlu

September 2021, 126 pages

In this thesis, design of a flight control system for an uncommon quadrotor aerial vehicle is discussed. This aerial vehicle consists of two counter-rotating big rotors on longitudinal axis to increase the lift capacity and flight endurance, and two counter-rotating small tilt rotors on lateral axis to stabilize the attitude.

Firstly, full nonlinear dynamic model of this vehicle is obtained by using Newton-Euler formulation. Later, derived approximate linear model around hover is statically decoupled to simplify the flight dynamics. Resulting diagonal model is mainly based on physical principles and it does not include dynamics such as uncertain parameters, sensor delays, flexible modes of the structure and inexact decoupling. Therefore, a system identification method is used, and more accurate model is estimated from flight tests when this vehicle is stabilized by PI controllers with sufficient performance and stability margins.

Secondly, relative importance of the parameters in the linear hover model is investigated. It is assumed that each parameter of the dynamic model has some uncertainty. Structured singular value sensitivity analysis determines the important parameters in terms of robust stability. Maximum tolerable uncertainties of parameters are also

computed.
High performance control design requires accurate model that is suitable for subsequent robust control design. Therefore, robust control criterion is considered during system identification step. System model is defined in terms of coprime factors which are identified by solving corresponding least squares problem using data-dependent orthonormal polynomials to achieve optimal numerical conditioning. Next, validation-based uncertainty modeling is used to compute the frequency dependent uncertainty upper bound. Using the uncertainty upper bound and specific coprime factorization of the stabilizing controller, robust-control-relevant model set is obtained which facilitates high performance robust controller synthesis.
Finally, performances of the PI controller with sufficient stability margins and the designed robust controller are analyzed. Attitude stabilization and torque disturbance rejection performances are compared. Results of several flight experiments show attitude control performance improvement with the designed robust controller compared to the standard PI controller.

Keywords: system identification, robust control, model uncertainty, attitude control, flight control, unmanned aerial vehicle, H_∞, model validation

ÖZ

YAYGIN OLMAYAN DÖRT ROTORLU BİR HAVA ARACI İÇİN UÇUŞ KONTROL SİSTEMİ TASARLANMASI

Baskın, Mehmet
Doktora, Elektrik ve Elektronik Mühendisliği Bölümü
Tez Yöneticisi: Prof. Dr. Kemal Leblebicioğlu

Eylül 2021 , 126 sayfa

Bu tezde, yaygın olmayan dört rotorlu bir hava aracı için uçuş kontrol sistemi tasarımı anlatılmıştır. Bu hava aracı kaldırma kapasitesini arttırmak için uzunlamasına eksende ters yönde dönen iki büyük rotordan ve yönelim kararlılığını sağlamak için yanlamasına eksende ters yönde dönen iki küçük eğilebilen rotordan oluşmaktadır.
İlk olarak Newton-Euler formülasyonu kullanılarak bu aracın tam doğrusal olmayan dinamik modeli elde edilmiştir. Sonra havada sabit konum çevresinde çıkarılan yakın doğrusal model statik olarak ayrılarak uçuş dinamikleri basitleştirilmiştir. Elde edilen diyagonal model temel olarak fiziksel prensiplere bağlıdır ve belirsiz parametreleri, algılayıcı gecikmelerini, yapının esnek modlarını ve hatalı ayırma gibi dinamikleri içermez. Bu nedenle sistem tanılama metodu kullanılmıştır ve daha doğru model bu araç yeterli performans ve kararlılık dereceleri veren PI denetleyiciler ile kararlı haldeyken yapılan uçuş testlerinden kestirilmiştir.
İkinci olarak, sabit konum doğrusal modelindeki parametrelerin önem dereceleri araştırılmıştır. Dinamik modeldeki her parametrenin belirli belirsizliği olduğu kabul edilmiştir. Yapılandırılmış tekil değer duyarlılık analizi gürbüz kararlılık bakımından

önemli olan parametreleri belirlemiştir. Parametrelerin tahammül edilebilir belirsizlikleri de hesaplanmıştır.
Yüksek performanslı denetleyici tasarımı için sonraki gürbüz denetleyici tasarımına uygun olan doğru model gereklidir. Bu nedenle sistem tanılama aşamasında gürbüz kontrol kriteri düşünülmüştür. Sistem modeli en uygun numerik şartlanma için veribağımlı birimdik polinomlar kullanılarak elde edilen doğrusal en küçük kareler probleminin çözümüyle kestirilen aralarında asal bölümlerle tanımlanmıştır. Sonra onaylama temelli belirsizlik modelleme yapılarak frekansa bağlı belirsizlik üst sınırı hesaplanmıştır. Belirsizlik üst sınırı ve kararlılık sağlayan denetleyicinin özel asal bölümleri kullanılarak yüksek performanslı denetleyici sentezini kolaylaştıran gürbüz kontrol amaçlı model set elde edilmiştir.
Son olarak yeterli kararlılık dereceleri veren PI denetleyici ile tasarlanan gürbüz denetleyicinin performansları analiz edilmiştir. Yönelim kararlılığı ve tork bozucu bastırma performansları karşılaştırılmıştır. Birçok uçuş deneyi tasarlanan gürbüz denetleyicinin PI denetleyici ile karşılaştırıldığında yönelim kontrol performansı artışı verdiğini göstermiştir.

Anahtar Kelimeler: sistem tanılama, gürbüz kontrol, model belirsizliği, yönelim kontrolü, uçuş kontrolü, insansız hava aracı, H_∞, model onaylama

To my family

ACKNOWLEDGMENTS

I would like to express my appreciation to my supervisor Prof. Dr. Kemal Leblebicioğlu for his helpful criticism, guidance and patience in the progress and preparation of this thesis.
I would like to thank my thesis committee members, Assoc. Prof. Dr. İlkay Yavrucuk and Assist. Prof. Dr. M. Mert Ankaralı for their valuable feedback and comments during committee meetings.
I would like to thank METU Electrical and Electronics Engineering Department faculty and staff for their help throughout my studies.
I would like to thank Dr. Gökhan Özdoğan, İ. Çağdaş Yılmaz and Raha Shabani for their help during experimental studies.
I would like to thank all my friends and colleagues who contributed to my thesis with their criticism and encouragement.
Finally, I am very grateful to members of my family for their support and encouragement during my study and my life.

TABLE OF CONTENTS

LIST OF TABLES

TABLES

LIST OF FIGURES

FIGURES

LIST OF ABBREVIATIONS

UAV	Unmanned aerial vehicles
VTOL	Vertical take off and landing
DC	Direct current
PID	Proportional-integral-derivative
LQ	Linear quadratic
ADRC	Active disturbance rejection control
FRF	Frequency response function
LFT	Linear fractional transformation
SISO	Single input single output
MIMO	Multiple input multiple output
RS	Robust stability
RP	Robust performance
RCF	Right coprime factorization
LCF	Left coprime factorization
LS	Least squares
DFT	Discrete Fourier transform
IID	Independent, identically distributed

LIST OF SYMBOLS

The following symbols will be used throughout the thesis.

$\mathcal{F}_E$	Earth inertial frame E
$\mathcal{F}_B$	Quadrotor body frame B
$\mathcal{F}_{P_i}$	i-th rotor-fixed frame P_i
$\mathcal{F}_{\bar{P}_i}$	i-th rotating rotor frame $\bar{P}_i$
R_B^E	Rotation matrix from $\mathcal{F}_B$ to $\mathcal{F}_E$
$R_{\bar{P}_i}^B$	Rotation matrix from $\mathcal{F}_{\bar{P}_i}$ to $\mathcal{F}_B$
$\xi = [x\ y\ z]^T$	Translational coordinates in the inertial frame
$\eta = [\phi\ \theta\ \psi]^T$	Orientation of the quadrotor in the inertial frame (roll, pitch and yaw angles, respectively)
V^B	Translational velocity of the quadrotor in the body frame
V^E	Translational velocity of the quadrotor in the inertial frame
k_{f_i}	Thrust coefficient of the i-th rotor
α_i	tilt angle of the i-th rotor about y_{P_i}, $i = 2, 4$
k_{d_i}	Drag coefficient of the i-th rotor
l_i^B	Distance from the center of gravity to i-th rotor, for big rotors, i.e., $i = 1, 3$, ($l_1^B = [\pm l_b\ 0\ l_{bh}]^T$), and for small rotors, i.e., $i = 2, 4$, ($l_2^B = [0\ \pm l_s\ l_{sh}]^T$)
g	Gravitational acceleration of Earth
I_n	An n-by-n identity matrix
$\text{diag}(a_1, \ldots, a_n)$	An n-by-n matrix with a_i's on the main diagonal and zeros elsewhere (a_i is the i-th main diagonal element)
A^T	Transpose of A

A^* or A^H	Complex conjugate transpose of A
A^{-1} and A^+	Inverse and pseudoinverse of A
μ	Structured singular value
μ_s	Skewed structured singular value
μ_g	Generalized structured singular value
$\mathbb{R}$ and $\mathbb{C}$	Fields of real and complex numbers
$\mathbb{Z}$	Set of integers
P_o	Actual plant
$\hat{P}$	Nominal model
P	Any linear time invariant system which may represent P_o, or $\hat{P}$
$\mathcal{P}$	Model set
C	Feedback controller
C^{RP}	Feedback controller which minimizes the worst-case performance
C^{exp}	Feedback controller used during system identification
C^{NP}	Feedback controller which minimizes the nominal performance
Δ_u	Perturbation block
$\mathcal{F}_u(M, Q)$	Upper LFT
$\mathcal{F}_l(M, Q)$	Lower LFT
$\mathcal{L}_\infty$	Banach space of matrix-valued (or scalar-valued) functions that are bounded on the imaginary axis
$\mathcal{H}_\infty$	Subspace of $\mathcal{L}_\infty$ with functions that are analytic and bounded in the open right-half plane
$\mathcal{RH}_\infty$	Real rational subspace of $\mathcal{H}_\infty$ which consists of all proper and real rational stable transfer matrices.
$J(P, C)$	Control criterion (performance)
$J_{WC}(\mathcal{P}, C)$	Worst-case performance
$\mathcal{P}^{\text{DY}}$	Dual-Youla model set
$\{\hat{N}, \hat{D}\}$	Right coprime factorization of $\hat{P}$

$\{N_o, D_o\}$	Right coprime factorization of P_o
$\{N_c, D_c\}$	Right coprime factorization of C^{exp}
$\mathcal{P}^{\text{RCR}}$	Robust-control-relevant model set
γ	norm bound of perturbation, i.e., $\|\Delta_u\|_\infty \leqslant \gamma$
Im(A)	Image (or range) space of A
Ker(A)	Kernel (or null) space of A
$\bar{\sigma}(A)$ and $\underline{\sigma}(A)$	The largest and the smallest singular values of A
f_{bw}	Gain cross-over frequency
L	The loop transfer function $L = PC$

Other symbols and terms will be defined locally for one chapter and they might be used differently in other chapters. This method is selected to adopt to common symbols and terms whenever possible.

CHAPTER 1

INTRODUCTION

Unmanned aerial vehicles (UAVs) have drawn a lot of interest in both academic research and commercial areas in the last decade. Among all UAVs, quadrotors have become the most common configuration due to vertical take off and landing (VTOL), hover in place and maneuverability abilities. The reduction of cost and complexity has increased the use of quadrotors in various military and civil applications [1, 2]. Apart from these favorable properties, quadrotors suffer from high energy consumption. Therefore, capability of power system have limited the usage of quadrotors in different applications.

Power source and efficiency of transferring that energy to air via rotors both limit flight endurance and payload capacity. Typical small commercial quadrotors have less than 20-minute flight endurance and payload size less than 1 kg [3, 4]. This is due to inadequate stored energy per unit mass of batteries to supply brushless DC motors. Since battery is the most influential component to quadrotor's weight, adding an extra battery to increase endurance also increases required power. In this respect, flight duration improvement of a common quadrotor configuration requires significant development of current battery technology. Since the improvement of batteries is a slow process, using alternative power source and increasing efficiency of lifting system have become an active research area.

For a typical multirotor, power requirement to maintain thrust over a rotor disc area changes exponentially with total weight and inverse of the rotor disc area [4, 5]. Consequently, quadrotors suffer from lower efficiency when compared to helicopters because of smaller rotor area in the given unit diameter footprint. On the other hand, mechanically complex rotor assemblies are fragile and require intensive maintenance. Therefore, interest in combining simple and robust quadrotor structure and efficiency

of helicopters has increased recently.

The triangular quadrotor introduced in [4] uses large rotor in the center to provide lift and canted three small rotors for control and counter torque. Even if 15 percent efficiency improvement is reported, this configuration gives degraded hover attitude control performance due to uncompensated gyroscopic torque of the main rotor when compared to a standard quadrotor [6, 7].

Using hydrocarbon fuel as an alternative power source significantly outperforms the battery powered propulsion system, and it gives relatively large flight endurance. In [8], coaxial inverting thruster using two gasoline engines is placed at the center of a standard quadrotor. In this case, gyroscopic and counter torques of engines are compensated; however, the coaxial rotors loose some of their efficiencies. This efficiency loss may be dramatic if large propellers are used at slow rotational speed [9]. In [10], variable pitch rotors are powered from a gasoline engine is reported. This configuration requires a complex drivetrain and four variable pitch rotors. These two configurations both improve the flight duration significantly. In addition, four-gasoline engine and four-combined electrical motor-gasoline engine configurations are reported in [11] and [12], respectively. These quadrotors are designed to carry very large payloads, and their cost is relatively high due to four gasoline engines.

From control theory point of view, a plenty of different control techniques have been introduced in the past years. Nested control loops for position and attitude was proved to be successful for standard quadrotors in different projects. PD type attitude controller and PID type position controller have become the most popular selection [5, 13, 14]. However, both PID and LQ type controllers guarantee stability around hover position where the quadrotor model is approximately linear. Next, it was shown that nonlinear control techniques such as backstepping, sliding-mode [15], feedback linearization [16], nonlinear $\mathcal{H}_\infty$ control [17] and ADRC [18] outperform linear methods in the presence of strong disturbances [19]. Later, to increase the operating range further from hover position and to stabilize the system under parameter variations robust and adaptive controllers are developed [20, 21].

1.1 Summary of contributions

Key contributions made in this thesis can be summarized as following:

- An uncommon quadrotor configuration is proposed to increase the efficiency and hence flight endurance compared to a standard quadrotor.

- Structured singular value (μ) sensitivity and skewed-μ analyses are used for the first time for a multirotor to analyze the effects of uncertain parameters and to determine their maximum allowable deviations in terms of closed loop stability.

- Estimation of a system model in flight by an identification method is not commonly used in aerospace applications. In this study, approximate linear model of the proposed quadrotor prototype is estimated from flight tests. During these tests, vehicle is stabilized around hover position, excitation signals are injected into control loops, and corresponding responses are measured.

- Robust-control-relevant identification is applied for a multirotor platform. This procedure gives an uncertain model set which facilitates high performance robust controller synthesis. To the author's knowledge, previous works do not investigate this uncommon method for an aerospace application.

- Parametric identification is not performed in a numerically optimal manner previously for an aerospace application. In this thesis, parameters are estimated accurately by solving optimally conditioned linear least squares problem. This study is the first application of this method for an unmanned vehicle.

- Validation-based uncertainty modeling is used for the first time for a multirotor platform.

- Skewed-μ synthesis is not commonly used in practical applications for robust control. However, this method is more suitable to robust control synthesis compared to the standard μ synthesis. Therefore, skewed-μ synthesis is applied for a multirotor platform successfully.

Figure 1.1: Prototype of the uncommon quadrotor configuration in flight

1.1.1 An uncommon quadrotor configuration

Inspired by the previous works, an uncommon quadrotor configuration is suggested to address the uncompensated gyroscopic torque problem for a single large rotor and low efficiency problem for coaxial large rotors. Therefore, two large rotors are placed on the longitudinal axis which are counter-rotating to minimize their gyroscopic and rotor drag torques. Since almost all weight of the device is lifted with large rotors, relatively small counter-rotating rotors on the lateral axis are selected for attitude control. The alternate rotors are not counter-rotating to minimize rotor drag and gyroscopic torques in this configuration unlike a standard case. Therefore, small rotors are equipped with tilt mechanism to gain the control of yaw motion. This configuration resembles the Boeing CH-47 Chinook; however, instead of a complex swashplate mechanism, two tiltable small rotors exist for attitude control.

Since almost equal weight is carried with two rotors having sufficiently large disc area, efficiency improvement can be obtained when compared to a standard quadrotor. Moreover, replacing large electrical motors with gasoline engines significantly improves the payload capacity and flight endurance with lower cost than the four-gasoline engine configuration discussed in [11, 12].

In this thesis, battery powered propulsion system composed of two large and two tilt mechanism integrated small electrical motors are used. Gasoline engine replacement for the large motors and efficiency analysis of this vehicle are left for future research. In this respect, this uncommon configuration is planned to combine the mechanical

simplicity of a quadrotor and efficiency of a tandem rotor helicopter. Figure 1.1 shows the proposed quadrotor prototype in flight experiment.

1.1.2 μ sensitivity and skewed-μ analyses

In the majority of the previous works, controllers are designed using dynamic model based on physical principles. In this case, bounds on model parameters are widely used, and a controller which gives sufficient performance under these parameter variations is aimed. But, required robustness may not be achieved if variations in these parameters are large. In that case, uncertainty in some parameters should be reduced. Therefore, important parameters for robust stability or performance should be determined using μ sensitivities. Skewed-μ analysis can be used to determine the maximum allowable uncertainty in parameters that are difficult to estimate.

1.1.3 System identification from flight tests

For a quadrotor aerial vehicle, flight controller is usually designed based on ideal dynamic model. Time delay of the gyroscopes, dynamics of rotor speed control, coupling effects due to inexact rotor mixing matrix, possible parasitic nonlinearities and flexible modes of the structure are not considered generally. Therefore, more accurate model of this vehicle is needed to improve the closed loop performance.
Estimating thrust and drag coefficients by static thrust tests, and inertia matrix from pendulum tests are commonly used [22]. Only a handful of studies discuss the identification of parameters or models from flight experiments for all UAVs. Such uncommon examples are reported in [23] and [24] for a model helicopter and a standard quadrotor, respectively.
In this thesis, system identification is performed in actual operational conditions around hover. Closed loop identification experiments are used while the quadrotor is stabilized by a controller. Frequency response function (FRF) of the attitude dynamics are obtained by applying several multisine experiments. Flight tests and FRFs are used to estimate the nominal model and various uncertainty sources that require for robust control formulation.

1.1.4 Robust-control-relevant identification

When a robust control method is used, selection of nominal model and uncertainty structure is very important to achieve high robust performance. In other words, uncertain model set should facilitate high robust performance. Commonly used additive and multiplicative type uncertainties usually lead to conservative control design. Therefore, during system identification and uncertainty modeling, robust control criterion is minimized. For that, coprime factor based dual-Youla-Kucera uncertainty structure is beneficial [25, 26]. For that particular model, nominal model identification and quantification of model uncertainty jointly minimize the robust control criterion with respect to the uncertain model set. In this way, resulting control synthesis can be performed in a non-conservative manner, and similar high performance can be obtained for the entire model set, as opposed to separate identification and control design. This method has been proved to be very effective for obtaining high performance control loops in motion control applications recently [27, 28]. Herein, this method is successfully applied for attitude control problem for the first time.

1.1.5 Numerically reliable identification

Robust-control-relevant nominal model identification problem is usually ill-conditioned if standard monomials are used. Therefore, coprime factors of nominal model can not be estimated accurately for this basis. For that reason, data-dependent orthonormal polynomials are used to obtain optimally conditioned linear least squares problem. By solving it, more accurate model can be obtained compared to standard monomials. This estimate and orthonormal polynomials are also used in the subsequent Gaus-Newton iterations. In this way, resulting nonlinear least squares problem also remains close to optimal. Therefore, accuracy of the estimate can be improved using Gaus-Newton algorithm.

In [29], this method is introduced for plant model estimation of single-input single-output (SISO) systems. In this thesis, this method is extended to coprime factors identification and multiple-input multiple-output (MIMO) cases, and modified formulations are given.

1.1.6 Validation-based uncertainty modeling

Nominal model should be accompanied by minimum uncertainty such that uncertain model and measured outputs from true system are consistent. However, this problem is ill-posed since correctly allocating model residuals between perturbation and disturbance is not clear. Pessimistic model validation methods where all nominal model residual is attributed to uncertainty may give overly conservative design as reported in [30] for motion control application. On the other hand, optimistic approaches where all residual is attributed to additive disturbance may lead to instability due to too small uncertainty acceptance. This problem is solved by applying the validation-based uncertainty modeling procedure introduced in [31]. Therefore, minimum uncertainty is computed such that measured outputs from the true system and uncertain model are consistent.

In aerospace applications, validation-based uncertainty modeling is rarely used. Only one study reported in [32] for a model helicopter is known by the author. In this thesis, model validation procedure is applied for the prototype vehicle, and uncertainty in the model is quantified successfully.

1.1.7 Skewed-μ synthesis

In robust control methods, uncertain model and required robustness are already determined before the subsequent controller synthesis. However, standard μ synthesis optimizes robustness and performance at the same time. Therefore, this method is not suitable when the required robustness is already known. Therefore, skewed-μ synthesis is used for robust controller design.

1.2 Organization of thesis

The thesis is organized as follows:

Chapter 2

The nonlinear dynamic model of the proposed quadrotor configuration is obtained by using Newton-Euler formulation. Herein, aerodynamic effects such as thrust change due to large angle of attack and high speed, blade flapping and interference effects are neglected, and only principal dynamics are used during modeling. Since planned usage of this vehicle is at slow velocities around hover, this assumption is reasonable and these effects can be considered as disturbance sources.

Chapter 3

For controller design purposes, linear approximation of the full nonlinear model around hover position is derived. Herein, resulting model is very similar to a usual quadrotor, with the exception of the rotor mixing (decoupling) matrix. This simplified and reduced model is used during both PID and robust attitude controller designs. Next, control structures used for quadrotors are explained. Cascade control structures for attitude and position control are introduced. Since the control method depends on nested loops, high performance position control inherently requires high performing inner attitude control loop. Therefore, attitude control problem and the proposed solution which is the main motivation of this thesis are discussed.

Chapter 4

In this Chapter, flight controller is designed for a proposed quadrotor model based on manuel loop shaping principles. For this closed loop configuration, important uncertain parameters for robust stability in the dynamic model are investigated using μ sensitivities. Later, tolerable uncertainty bound for different parameter configurations are computed using skewed-μ analysis. Maximum allowable perturbations in the parameters which are difficult or expensive to estimate are calculated.

Chapter 5

Robust-control-relevant identification and its main motivation are explained in detail. Dual-Youla-Kucera uncertainty structure is constructed with specific coprime factors of nominal model and stabilizing controller. For that specific structure, it is shown that nominal model identification and quantification of model uncertainty together give robust-control-relevant model set. Then, computation method of these specific

coprime factors of the stabilizing controller is explained. Next, identification technique of nominal model coprime factors is discussed using data-dependent orthonormal polynomials to achieve optimal numerical conditioning. After that, finding an accurate nominal model is investigated by solving resulting optimally conditioned linear least squares problem.

Chapter 6

Typical parametric identification problem is converted into a weighted least squares optimization problem. Problem is first formulated according to single variate case. Next, extension of this formulation to parameter estimation of multivariable systems and coprime factors are also explained. Importance of the numerical conditioning of the optimization problem in estimating accurate parameters is discussed. The optimization problem is converted into optimally conditioned one to obtain more accurate model. Therefore, to reach optimal numerical conditioning of the least squares problem, data-dependent orthonormal polynomials with respect to data-dependent discrete inner product are introduced. Derivation of these orthonormal block polynomials is discussed in detail. Subsequent Gaus-Newton algorithm for the original nonlinear least squares problem is introduced.

Chapter 7

Validation-based uncertainty modeling method is discussed. This method determines the minimum uncertainty upper bound such that measured outputs from the true system and the uncertain model are consistent. Formulation of the model validation problem and its solution method are discussed in detail. Computed uncertainty is later used in constructing uncertain model set and designing robust controller.

Chapter 8

This chapter is reserved for a visualization method of the uncertain model set. Bode magnitude diagram construction techniques for multivariable as well as single variate case are discussed. This method uses standard, generalized and skewed structured singular values. Definitions of these structured singular values are given. Then, corresponding upper and lower Bode magnitude bounds of uncertain models, and their computation methods are introduced.

Chapter 9

Using the dual-Youla-Kucera uncertainty structure, model uncertainty and performance weights, robust control problem is formulated. Then, skewed-μ synthesis

based robust controller design method is introduced. The solution method of standard μ synthesis is modified for the solution of skewed-μ type problem. Using this method, skewed-μ synthesis can be performed with the available software developed for the standart μ synthesis.

Chapter 10

This chapter is allocated to investigate the constructed prototype of the proposed vehicle. Hardware and software architectures of this prototype are introduced in detail.

Chapter 11

Various experimental results are illustrated. Firstly, FRF of the attitude dynamics around hover is obtained by applying several multisine tests when the vehicle is stabilized with PI rate controller with sufficient robustness margins. Weighting filters are determined to satisfy desired bandwidths for attitude rate control. Coprime factors of nominal model are estimated. Next, coprime factors of the controller are computed. Robust-control-relevant set is constructed using these coprime factors and calculated model uncertainty. Later, this uncertain model set is visualized using Bode diagrams. Theoretical results of control designs are listed. Performances of the PI controller and the designed robust controller are analyzed. Attitude stabilization and torque disturbance rejection performances are compared. Results of several flight experiments show attitude control performance improvement with the designed robust controller compared to the standard PI controller.

Chapter 12

In this chapter, important observations and findings are discussed. Conclusion and some future works are also explained.

CHAPTER 2

DYNAMICAL MODEL

As in the standard case, the proposed quadrotor configuration can be viewed as a connection of five rigid bodies, quadrotor body B, and four rotor groups P_i attached to it. These consist of big rotors on the longitudinal axis corresponding to $i = 1, 3$ and small rotors equipped with tilting mechanism on the lateral axis corresponding to $i = 2, 4$. The main motivation of this chapter is to drive the equations of motion for this system. The standard quadrotor modeling procedures followed in [1, 13, 33] and methods reported in [34, 35, 36] for tilting propeller configurations are specifically extended and tailored to meet the needs of the proposed vehicle configuration.

2.1 Preliminary definitions

Let $\mathcal{F}_E : \{O_E; x_E, y_E, z_E\}$ be an earth inertial frame and $\mathcal{F}_B : \{O_B; x_B, y_B, z_B\}$ be a quadrotor body frame attached to its center of gravity. Moreover, rotor-fixed frames which are selected as parallel to each other and body frame are given by $\mathcal{F}_{P_i} : \{O_{P_i}; x_{P_i}, y_{P_i}, z_{P_i}\},\ i = 1, 2, 3, 4$. The orientation of second and forth rotors are changed by rotation with respect to rotor-fixed frame around y_{P_i} by an angle of α_i. This rotation creates a new rotating frame for small rotors as shown in Figure 2.1, and they are represented by $\mathcal{F}_{\bar{P}_i} : \{O_{\bar{P}_i}; x_{\bar{P}_i}, y_{\bar{P}_i}, z_{\bar{P}_i}\},\ i = 2, 4$. To balance the gyroscopic and counter torques in hover, rotating directions of similar type motors must be opposite. In this respect, rotor 1 and 2 revolve in clockwise (CW) direction, and rotor 3 and 4 revolve in counter clockwise (CCW) direction.

Let the vector $\mathsf{q} = [\xi^T\ \eta^T]^T$ denote the generalized coordinates where $\xi = [x\ y\ z]^T$ denotes the translational coordinates in the inertial frame and three Euler angles $\eta =$

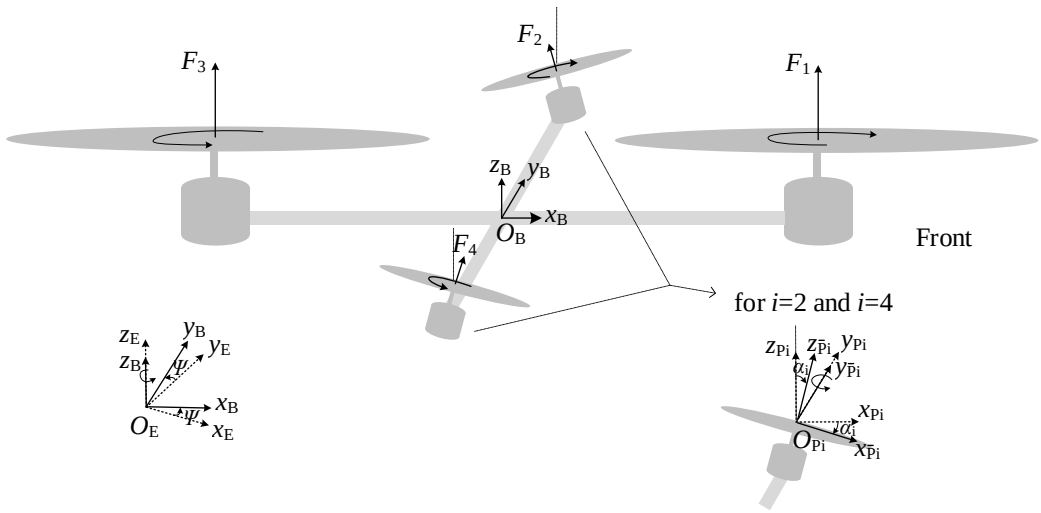

Figure 2.1: Suggested quadrotor configuration

$[\phi\ \theta\ \psi]^T$ denotes the orientation of the quadrotor. Roll angle ϕ determines the rotation around the x-axis, pitch angle θ determines the rotation around the y-axis, and yaw angle ψ determines the rotation around the z-axis. Then, the overall rotation matrix from body frame to inertial frame can be computed from three consecutive rotations as $R_B^E = R_Z(\psi)R_Y(\theta)R_X(\phi)$ which is given by (2.1) where $sx = \sin(x)$ and $cx = \cos(x)$. Since this rotation matrix is orthonormal, the equalities $(R_B^E)^{-1} = R_E^B = (R_B^E)^T$ are satisfied.

$$R_B^E = \begin{bmatrix} c\psi c\theta & -s\psi c\phi + c\psi s\theta s\phi & s\psi s\phi + c\psi s\theta c\phi \\ s\psi c\theta & c\psi c\phi + s\psi s\theta s\phi & -c\psi s\phi + s\psi s\theta c\phi \\ -s\theta & c\theta s\phi & c\theta c\phi \end{bmatrix} \tag{2.1}$$

Moreover, let $R_{\bar{P}_i}^{P_i}$ be the rotation matrix from rotating rotor frame $\mathcal{F}_{\bar{P}_i}$ to rotor-fixed frame $\mathcal{F}_{P_i}$ for $i = 2, 4$. This rotation matrix given in (2.2) also equals to $R_{\bar{P}_i}^B$ since the body fixed frame $\mathcal{F}_B$ and rotor fixed frame $\mathcal{F}_{\bar{P}_i}$ are parallel.

$$R_{\bar{P}_i}^{P_i} = R_{\bar{P}_i}^B = \begin{bmatrix} c\alpha_i & 0 & s\alpha_i \\ 0 & 1 & 0 \\ -s\alpha_i & 0 & c\alpha_i \end{bmatrix} \tag{2.2}$$

The relation between body frame angular rates $[p\ q\ r]^T$ and rates of Euler angles $[\dot{\phi}\ \dot{\theta}\ \dot{\psi}]^T$ is given by (2.3) where $tx = \tan(x)$ [33].

$$\begin{bmatrix} \dot{\phi} \\ \dot{\theta} \\ \dot{\psi} \end{bmatrix} = \begin{bmatrix} 1 & s\phi t\theta & c\phi t\theta \\ 0 & c\phi & -s\phi \\ 0 & s\phi/c\theta & c\phi/c\theta \end{bmatrix} \begin{bmatrix} p \\ q \\ r \end{bmatrix} \tag{2.3}$$

2.2 Equations of motion

The motion equations of a rigid body are obtained by using Newton-Euler formulation as

$$m\dot{V}^B + \Omega \times mV^B = F^B \ , \tag{2.4}$$

$$I\dot{\Omega} + \Omega \times I\Omega = \Gamma^B \ , \tag{2.5}$$

where F^B and Γ^B are the total force and torque applied to center of gravity, and m is the mass of the quadrotor. $\Omega = [p\ q\ r]^T$ is the body frame angular rate, $V^B = [\dot{x}^B\ \dot{y}^B\ \dot{z}^B]^T$ is the translational velocity of the quadrotor, and I is the moments of inertia about the body-fixed frame $\mathcal{F}_B$.

2.2.1 Translational motion

Body frame: The tilt motion of the small rotor creates thrust components affecting translational and rotational motion given by (2.6), and for the fixed rotor, the thrust is obtained by (2.7) where $F_i^{\bar{P}} = [0\ 0\ k_{f_i} w_i^2]^T$ is the thrust generated by the corresponding rotor.

$$F_i^B = R_{\bar{P}_i}^B F_i^{\bar{P}_i},\ i = 2, 4 \tag{2.6}$$

$$F_i^B = F_i^{\bar{P}_i},\ i = 1, 3 \tag{2.7}$$

The translational motion of a quadrotor is represented by (2.8) where $G^E = [0\ 0\ -g]^T$ is the gravity vector, and T^B is the total thrust vector (2.9).

$$m\dot{V}^B + \Omega \times mV^B = (R_B^E)^T mG^E + T^B \tag{2.8}$$

$$T^B = \sum_{i=1}^{4} F_i^B \tag{2.9}$$

Inertial frame: Translational dynamics in the inertial frame can be obtained by (2.10) since the centrifugal forces are nullified where $V^E = \dot{\xi}$.

$$m\dot{V}^E = mG^E + R_B^E T^B \tag{2.10}$$

2.2.2 Rotational motion

The Γ^B term in (2.5) is composed of some torque components which are discussed in this section.

Actuators torque: Actuators torque can be obtained by (2.11) where $l_1^B = [l_b\ 0\ l_{bh}]^T$, $l_2^B = [0\ l_s\ l_{sh}]^T$, $l_3^B = [-l_b\ 0\ l_{bh}]^T$, $l_4^B = [0\ -l_s\ l_{sh}]^T$ are distances from the center of gravity to rotors.

$$\Gamma_A^B = \sum_{i=1}^{4} l_i^B \times F_i^B \tag{2.11}$$

Gyroscopic torque: Gyroscopic torque due to rotors is given by (2.12), and it is rewritten as (2.13) where I_{R_b} and I_{R_s} is the inertia of big and small rotors, respectively, and w_i is the speed of the corresponding rotor.

$$\Gamma_G^B = \sum_{i=1}^{4} I_{R_i}(\Omega \times \bar{W}_i^B) \tag{2.12}$$

$$\Gamma_G^B = I_{R_b}\begin{bmatrix} p \\ q \\ r \end{bmatrix} \times \begin{bmatrix} 0 \\ 0 \\ w_3 - w_1 \end{bmatrix} + I_{R_s}\begin{bmatrix} p \\ q \\ r \end{bmatrix} \times \left(R_{\bar{P}_2}^B \begin{bmatrix} 0 \\ 0 \\ -w_2 \end{bmatrix} + R_{\bar{P}_4}^B \begin{bmatrix} 0 \\ 0 \\ w_4 \end{bmatrix} \right) \tag{2.13}$$

Rotor drag (counter) torque: Drag torque of the rigid rotors about the center of mass of the vehicle is modeled by

$$\Gamma_D^B = \sum_{i=1}^{4} R_{\bar{P}_i}^B D_i^{\bar{P}_i}\ , \tag{2.14}$$

where $D_i^{\bar{P}} = [0\ 0\ -\sigma_i k_{d_i} w_i^2]^T$ is the counter-rotating torque generated about the $z_{\bar{P}_i}$ axis where $\sigma_i \in \{-1, 1\}$ denotes the direction of rotor while -1 and 1 correspond to negative and positive rotation around $z_{\bar{P}_i}$ axis, respectively.

It is assumed that the quadrotor has symmetric structure and its inertia matrix is taken

as

$$I = \begin{bmatrix} I_{xx} & 0 & \\ 0 & I_{yy} & 0 \\ 0 & 0 & I_{zz} \end{bmatrix} . \tag{2.15}$$

Finally, from (2.5) and (2.10), the overall motion equations (2.16) and (2.17) of the quadrotor are derived where $\Gamma^B = \Gamma^B_A + \Gamma^B_D - \Gamma^B_G$.

$$\ddot{\xi} = G^E + \frac{1}{m} R^E_B T^B \tag{2.16}$$

$$\dot{\Omega} = I^{-1}(-\Omega \times I\Omega + \Gamma^B) \tag{2.17}$$

Moreover, rate of the Euler angles can be obtained from body frame rates as

$$\begin{aligned} \dot{\phi} &= p + s\phi t\theta \; q + c\phi t\theta \; r \; , \\ \dot{\theta} &= c\phi \; q - s\phi \; r \; , \\ \dot{\psi} &= \frac{s\phi \; q + c\phi \; r}{c\theta} \; . \end{aligned} \tag{2.18}$$

2.3 Additional aerodynamic effects

In this thesis, aerodynamic effects such as thrust change due to large angle of attack and high speed, blade flapping and interference effects are neglected, and only principal dynamics are used during modeling. Since planned usage of this device is at slow velocities around hover, these assumptions are reasonable, and these effects can be considered as disturbances to be minimized by attitude controllers [5].

CHAPTER 3

MOTION CONTROL FOR THE PROPOSED QUADROTOR

The full nonlinear dynamic model derived in the previous chapter is suitable for simulation of the quadrotor motion in space even if some secondary aerodynamic effects are neglected in the model. However, especially rotational motion equations are fairly complex for control purposes. Therefore, reduced model which is more suitable to control design is needed. Firstly, it is assumed that bandwidth of rotor speed control is sufficiently high such that transients on w_i are neglected. In this way, electrical motor dynamics may not be considered, w_i's can be considered as control inputs instead of motor torques [35]. For a quadrotor in slow flight conditions, the second order inertial and gyroscopic terms are rather smaller than the forces and torques generated by propeller actuation. Therefore, these second order terms are considered as disturbances that need to be canceled by the controller. Therefore, the following simplified rotational motion equation is used for controller design purpose where the third term $(-\Gamma_G^B)$ is neglected, and $\Gamma^B = \Gamma_A^B + \Gamma_D^B$ is used.

$$\dot{\Omega} = I^{-1}\Gamma^B \tag{3.1}$$

Finally, solving translational motion equations in (2.16) and simplified rotational equations in (3.1), the following motion equations are obtained.

$$\begin{aligned}
\ddot{x} &= \frac{((s\phi s\psi + c\phi c\psi s\theta)(k_{f_b}w_1^2 + k_{f_s}c\alpha_2 w_2^2 + k_{f_b}w_3^2 + k_{f_s}c\alpha_4 w_4^2))}{m} \\
&+ \frac{c\psi c\theta k_{f_s}(s\alpha_2 w_2^2 + s\alpha_4 w_4^2)}{m} \\
\ddot{y} &= -\frac{((c\psi s\phi - c\phi s\psi s\theta)(k_{f_b}w_1^2 + k_{f_s}c\alpha_2 w_2^2 + k_{f_b}w_3^2 + k_{f_s}c\alpha_4 w_4^2)}{m} \\
&+ \frac{c\theta s\psi k_{f_s}(s\alpha_2 w_2^2 + s\alpha_4 w_4^2)}{m} \\
\ddot{z} &= \frac{(c\phi c\theta(k_{f_b}w_1^2 + k_{f_s}c\alpha_2 w_2^2 + k_{f_b}w_3^2 + k_{f_s}c\alpha_4 w_4^2))}{m} - \frac{(s\theta k_{f_s}(s\alpha_2 w_2^2 + s\alpha_4 w_4^2)}{m} - g
\end{aligned} \tag{3.2}$$

$$
\begin{aligned}
\dot{p} &= \frac{k_{d_s} w_2^2 s\alpha_2 - k_{d_s} w_4^2 s\alpha_4 + k_{f_s} l_s w_2^2 c\alpha_2 - k_{f_s} l_s w_4^2 c\alpha_4}{I_{xx}} \\
\dot{q} &= \frac{-k_{f_b} l_b w_1^2 + k_{f_s} l_{sh} s\alpha_2 w_2^2 + k_{f_b} l_b w_3^2 + k_{f_s} l_{sh} s\alpha_4 w_4^2}{I_{yy}} \\
\dot{r} &= \frac{k_{d_b} w_1^2 - k_{d_b} w_3^2 + k_{d_s} w_2^2 c\alpha_2 - k_{d_s} w_4^2 c\alpha_4 - k_{f_s} l_s w_2^2 s\alpha_2 + k_{f_s} l_s w_4^2 s\alpha_4}{I_{zz}}
\end{aligned}
\tag{3.3}
$$

These equations can be written in a compact form as given in (3.4) and (3.5) to simplify the analysis during linearization where $w = [w_1^2\ w_2^2\ w_3^2\ w_4^2]^T$ are the manipulated variables.

$$
\ddot{\xi} = \begin{bmatrix} 0 \\ 0 \\ -g \end{bmatrix} + \frac{1}{m} R_B^E F(\alpha) w \tag{3.4}
$$

$$
\dot{\Omega} = I^{-1} \tau(\alpha) w \tag{3.5}
$$

$F(\alpha)$ and $\tau(\alpha)$ in the above equations are given as below.

$$
\begin{aligned}
F(\alpha) &= \begin{bmatrix} 0 & k_{f_s} s\alpha_2 & 0 & k_{f_s} s\alpha_4 \\ 0 & 0 & 0 & 0 \\ k_{f_b} & k_{f_s} c\alpha_2 & k_{f_b} & k_{f_s} c\alpha_4 \end{bmatrix} \\
\tau(\alpha) &= \begin{bmatrix} 0 & k_{d_s} s\alpha_2 + k_{f_s} l_s c\alpha_2 & 0 & -k_{d_s} s\alpha_4 - k_{f_s} l_s c\alpha_4 \\ -k_{f_b} l_b & k_{f_s} l_{sh} s\alpha_2 & k_{f_b} l_b & k_{f_s} l_{sh} s\alpha_4 \\ k_{d_b} & k_{d_s} c\alpha_2 - k_{f_s} l_s s\alpha_2 & -k_{d_b} & -k_{d_s} c\alpha_4 + k_{f_s} l_s s\alpha_4 \end{bmatrix}
\end{aligned}
\tag{3.6}
$$

3.1 Linearization of the model in hover

The relation between rates of Euler angles and body rates in (2.18), dynamic equations (3.4) and (3.5), manipulated variables $u = [w^T\ \alpha^T]^T$ where $\alpha = [\alpha_2\ \alpha_4]^T$ and states $x = [(V^E)^T\ \eta^T\ \Omega^T]^T$ are used to obtain linearized model of the quadrotor in hover conditions. It basically originates from Taylor series of a nonlinear model around x_{eq} and u_{eq}, and it is obtained by dropping all but first-order terms in the expansion [37].

3.1.1 Translational motion

The local linearization can be obtained by expanding (3.4) around x_{eq} and u_{eq} where $\delta\eta$ and δu denote the perturbation from η_{eq} and u_{eq}.

$$\delta\ddot{\xi} = \frac{1}{m}\frac{\partial}{\partial\eta}\left(R_B^E F(\alpha)w\right)\Big|_{x_{eq},u_{eq}}\delta\eta + \frac{1}{m}R_B^E\frac{\partial}{\partial u}\left(F(\alpha)w\right)\Big|_{x_{eq},u_{eq}}\delta u \tag{3.7}$$

Let $\tilde{f} = F(\alpha)w$ and $(R_B^E)_i$ be the ith column of the matrix and $\tilde{f}_i$ be the ith entry of the vector. Then, (3.7) can be simplified and corresponding matrices can be derived.

$$A_{trans} = \frac{1}{m}\sum_{i=1}^{3}\frac{\partial(R_B^E)_i}{\partial\eta}\tilde{f}_i\Big|_{x_{eq},u_{eq}} \tag{3.8}$$

$$B_{trans} = \frac{1}{m}R_B^E\left[F(\alpha) \quad \textstyle\sum_{i=1}^{4}\frac{\partial(F(\alpha))_i}{\partial\alpha}w_i\right]\Big|_{x_{eq},u_{eq}} \tag{3.9}$$

3.1.2 Rotational motion

Applying the similar procedure to (3.5), following results are obtained for rotational motion.

$$\dot{\Omega} = I^{-1}\frac{\partial}{\partial u}\left(\tau(\alpha)w\right)\Big|_{x_{eq},u_{eq}}\delta u \tag{3.10}$$

$$B_{rot} = I^{-1}\left[\tau(\alpha) \quad \textstyle\sum_{i=1}^{4}\frac{\partial(\tau(\alpha))_i}{\partial\alpha}w_i\right]\Big|_{x_{eq},u_{eq}} \tag{3.11}$$

3.1.3 Overall linearized model

The linearization is obtained around equilibrium at hover position where $u = [w^T\ \alpha^T]^T = [w_{eq}\ 0\ 0]^T$ and states $x = [(V^E)^T\ \eta^T\ \Omega^T]^T = [0\ 0\ 0\ 0\ 0\ \psi\ 0\ 0\ 0]^T$. For linearized system at these conditions, rates of Euler angles and body frame rates are equal $\dot{\eta} = \Omega$. Finally, the overall linearized model (3.12) is reached.

$$\begin{bmatrix}\delta\dot{V}^E\\ \delta\dot{\eta}\\ \delta\dot{\Omega}\end{bmatrix} = \begin{bmatrix}0 & A_{trans} & 0\\ 0 & 0 & I\\ 0 & 0 & 0\end{bmatrix}\begin{bmatrix}\delta V^E\\ \delta\eta\\ \delta\Omega\end{bmatrix} + \begin{bmatrix}B_{trans}\\ 0\\ B_{rot}\end{bmatrix}\begin{bmatrix}\delta w\\ \delta\alpha_2\\ \delta\alpha_4\end{bmatrix} \tag{3.12}$$

The submatrices in (3.12) can be written below where $T = (k_{f_b} w_1^2 + k_{f_s} w_2^2 + k_{f_b} w_3^2 + k_{f_s} w_4^2)$ is the total thrust component in z-axis at hover conditions.

$$
\begin{aligned}
A_{trans} &= \frac{1}{m} \begin{bmatrix} s\psi\, T & c\psi\, T & 0 \\ -c\psi\, T & s\psi\, T & 0 \\ 0 & 0 & 0 \end{bmatrix} \\
B_{trans} &= \frac{1}{m} \begin{bmatrix} 0 & 0 & 0 & 0 & k_{f_s} w_{eq2} c\psi & k_{f_s} w_{eq4} c\psi \\ 0 & 0 & 0 & 0 & k_{f_s} w_{eq2} s\psi & k_{f_s} w_{eq4} s\psi \\ k_{f_b} & k_{f_s} & k_{f_b} & k_{f_s} & 0 & 0 \end{bmatrix} \\
B_{rot} &= I^{-1} \begin{bmatrix} 0 & k_{f_s} l_s & 0 & -k_{f_s} l_s & k_{d_s} w_{eq2} & -k_{d_s} w_{eq4} \\ -k_{f_b} l_b & 0 & k_{f_b} l_b & 0 & k_{f_s} l_{sh} w_{eq2} & k_{f_s} l_{sh} w_{eq4} \\ k_{d_b} & k_{d_s} & -k_{d_b} & -k_{d_s} & -k_{f_s} l_s w_{eq2} & k_{f_s} l_s w_{eq4} \end{bmatrix}
\end{aligned}
\tag{3.13}
$$

Similar to a common configuration, stabilization of the proposed quadrotor around hover position requires control of translational motion in z-axis and rotational motions. Then, following reduced equation can be obtained from (3.12) where $\bar{\xi} = z$.

$$
\begin{aligned}
\begin{bmatrix} \delta\ddot{\bar{\xi}} \\ \delta\dot{\Omega} \end{bmatrix} &= \begin{bmatrix} m^{-1} & 0 \\ 0 & I^{-1} \end{bmatrix} \begin{bmatrix} k_{f_b} & k_{f_s} & k_{f_b} & k_{f_s} & 0 & 0 \\ 0 & k_{f_s} l_s & 0 & -k_{f_s} l_s & k_{d_s} w_{eq2} & -k_{d_s} w_{eq4} \\ -k_{f_b} l_b & 0 & k_{f_b} l_b & 0 & k_{f_s} l_{sh} w_{eq2} & k_{f_s} l_{sh} w_{eq4} \\ k_{d_b} & k_{d_s} & -k_{d_b} & -k_{d_s} & -k_{f_s} l_s w_{eq2} & k_{f_s} l_s w_{eq4} \end{bmatrix} \begin{bmatrix} \delta w \\ \delta\alpha_2 \\ \delta\alpha_4 \end{bmatrix} \\
&= A \begin{bmatrix} \delta w \\ \delta\alpha_2 \\ \delta\alpha_4 \end{bmatrix}
\end{aligned}
\tag{3.14}
$$

Therefore, nonlinear quadrotor model is approximated locally as (3.15), where $\delta\bar{x} = [\delta\dot{z}\ \delta\Omega^T]^T$ and $\delta u = [\delta w^T\ \delta\alpha^T]^T$.

$$
\begin{aligned}
\bar{x} &= \bar{x}_{eq} + \delta\bar{x} \\
u &= u_{eq} + \delta u
\end{aligned}
\tag{3.15}
$$

3.2 Controllability and stabilization

Since control mapping matrix A in (3.14) is of rank 4, selected 4 degrees of freedom (DoF), namely translational motion in z-axis and rotational motions in roll, pitch

and yaw axes, can be controlled independently. The following control law (3.16) ensures the control of these 4 DoF where A^+ denotes the pseudoinverse of A which is computed as (3.17).

$$\underbrace{\begin{bmatrix} \delta w \\ \delta\alpha_2 \\ \delta\alpha_4 \end{bmatrix}}_{\delta u} = A^+ \underbrace{\begin{bmatrix} \delta\ddot{\bar{\xi}}_r \\ \delta\dot{\Omega}_r \end{bmatrix}}_{\delta\bar{x}_r} \tag{3.16}$$

$$A^+ = A^T(AA^T)^{-1} \tag{3.17}$$

Main aim of the controller is to satsify $\delta\ddot{\bar{\xi}} = \delta\ddot{\bar{\xi}}_r$ and $\delta\dot{\Omega} = \delta\dot{\Omega}_r$ for the linearized quadrotor model. Therefore, proportional derivative (PD) control law (3.18) can be used for translational motion part.

$$\delta\ddot{\bar{\xi}}_r = \delta\ddot{\bar{\xi}}_d + K_{p1}(\delta\dot{\bar{\xi}}_d - \delta\dot{\bar{\xi}}) + K_{p2}(\delta\bar{\xi}_d - \delta\bar{\xi}) \tag{3.18}$$

If diagonal positive definite matrices K_{p1} and K_{p2} define Hurwitz polynomials, the position error converges to 0 exponentially.
Similarly, orientation tracking can be controlled by using PD laws (3.19) since $\delta\dot{\eta} = \delta\Omega$ for the linearized quadrotor model in hover.

$$\delta\dot{\Omega}_r = \delta\dot{\Omega}_d + K_{w1}(\delta\Omega_d - \delta\Omega) + K_{w2}(\delta\eta_d - \delta\eta) \tag{3.19}$$

If diagonal positive definite matrices K_{w1} and K_{w2} define Hurwitz polynomials, the orientation error converges to 0 exponentially.

3.2.1 Translational motions in x and y axes

As discussed in the previous section, translational motions in x and y axes are coupled to other states due to inherent underactuation. Therefore, control in x and y axes is performed by controlling roll and pitch angles. The following equations from (3.12) can be used to control the vehicle in these axes.

$$\begin{aligned} \delta\ddot{x} &= (s\psi\phi + c\psi\theta)\frac{T}{m} \\ \delta\ddot{y} &= -(c\psi\phi - s\psi\theta)\frac{T}{m} \end{aligned} \tag{3.20}$$

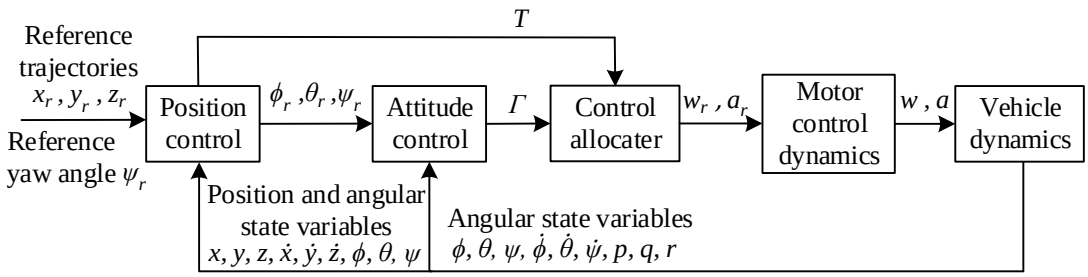

Figure 3.1: Control structure

In hover, $T = mg$ is satisfied, and roll and pitch angle reference values can be obtained as below by manipulating (3.20).

$$\begin{aligned} \phi_r &= \frac{\delta\ddot{x}_r\, s\psi_r - \delta\ddot{y}_r\, c\psi_r}{g} \\ \theta_r &= \frac{\delta\ddot{x}_r\, c\psi_r + \delta\ddot{y}_r\, s\psi_r}{g} \end{aligned} \tag{3.21}$$

According to acceleration reference in x and y axes, corresponding roll and pitch angle references are created and followed for good trajectory tracking.

3.3 Quadrotor control

A hierarchical control strategy commonly used for quadrotors is also applicable to the proposed configuration. In the lowest level, rotor speed and tilt angle control loops present. Generally, these loops have very high bandwidth and their transients can be neglected. However, in this thesis, combined motor control and vehicle dynamics are estimated from identification tests. In the second level, attitude control loops exist to track desired angles. At the top level, position controllers exist which determines required Euler angles according to desired position commands [1, 38]. This cascade control structure which includes these levels is illustrated in Figure 3.1.

3.3.1 Quadrotor attitude controller design

If PID based control is not sufficient, higher performance can be obtained by using model based control techniques. Statically decoupled model can be used which essentially converges to first order mass and inertia lines in frequency domain for trans-

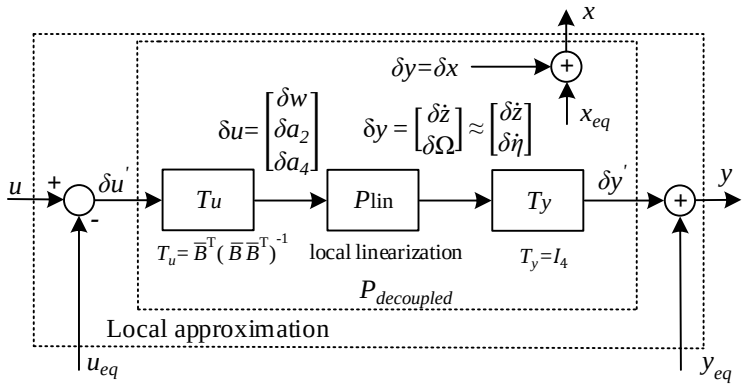

Figure 3.2: Decoupled linearized plant model

lational and rotational motions, respectively. This can be achieved by manipulating equation (3.22).

$$\begin{bmatrix} \delta\ddot{\xi} \\ \delta\dot{\Omega} \end{bmatrix} = \begin{bmatrix} m^{-1} & 0 \\ 0 & I^{-1} \end{bmatrix} \underbrace{\begin{bmatrix} k_{f_b} & k_{f_s} & k_{f_b} & k_{f_s} & 0 & 0 \\ 0 & k_{f_s} l_s & 0 & -k_{f_s} l_s & k_{d_s} w_{eq2} & -k_{d_s} w_{eq4} \\ -k_{f_b} l_b & 0 & k_{f_b} l_b & 0 & k_{f_s} l_{sh} w_{eq2} & k_{f_s} l_{sh} w_{eq4} \\ k_{d_b} & k_{d_s} & -k_{d_b} & -k_{d_s} & -k_{f_s} l_s w_{eq2} & k_{f_s} l_s w_{eq4} \end{bmatrix}}_{\bar{B}} \begin{bmatrix} \delta w \\ \delta\alpha_2 \\ \delta\alpha_4 \end{bmatrix} \tag{3.22}$$

$$\begin{aligned} T_u &= \bar{B}^T (\bar{B}\bar{B}^T)^{-1} \\ T_y &= I_4 \end{aligned} \tag{3.23}$$

By selecting input decoupling matrix T_u and output decoupling matrix T_y as in (3.23), the decoupled model can be obtained as shown in Figure 3.2. Therefore, ideal decoupled model in (3.24) that is composed of mass and inertia lines are obtained where $\delta u = T_u\ \delta u'$ and $\delta y' = T_y\ \delta y = \delta y = [\delta\dot{z}\ \delta\Omega^T]^T$.

$$P_{decoupled}(s) : \delta u' \rightarrow \delta y' = \begin{bmatrix} \frac{1}{m\ s} & 0 & 0 & 0 \\ 0 & \frac{1}{I_{xx}\ s} & 0 & 0 \\ 0 & 0 & \frac{1}{I_{yy}\ s} & 0 \\ 0 & 0 & 0 & \frac{1}{I_{zz}\ s} \end{bmatrix} \tag{3.24}$$

However, due to inexact decoupling, parasitic nonlinearities, rate gyro sensor delay, flexible modes of a structure and other negligible dynamics the model differs from the ideal. In this thesis, actual plant model will be obtained by using multisine excitation signal while the vehicle is stabilized by a controller in hover. Later, the difference of

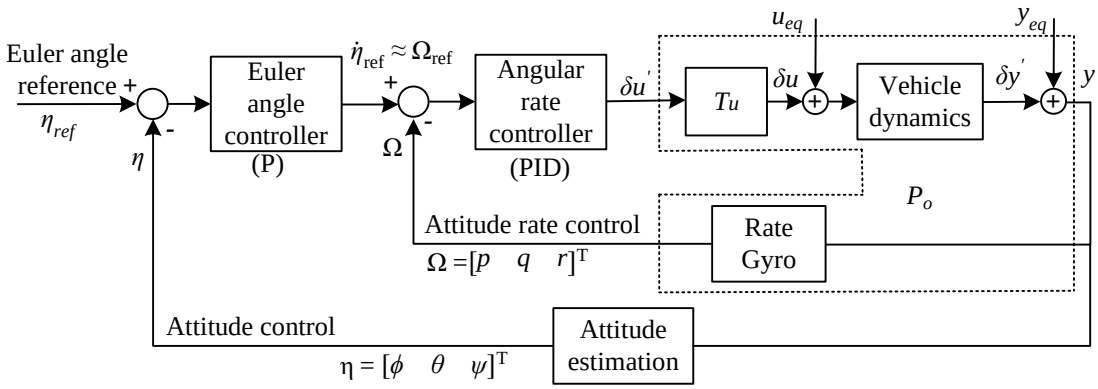

Figure 3.3: Cascade control structure for attitude control

the actual model from the ideal decoupled model will be analyzed, and the difference will be used during uncertainty modeling stage.

Although a single angle controller is able to control the quadrotor attitude, using cascaded structure as depicted in Figure 3.3 has certain advantages. Firstly, tuning of cascade loop is much simpler compared to a single controller tuning. Since the inner loops are composed of inertia lines (only one integrator in each loop), finding correct controller is simpler. This also holds for the outer loop, since angle controller equivalently deals with one integrator dynamics. Next, achievable bandwidth of the rate loop is much larger, compared to angle loop. Therefore, high performance inner rate loop can be designed which minimizes the effects of nonlinear dynamics. Performance can be further improved if higher sampling rate is used for the inner loop. Therefore, the benefit of dual sampling rate can be received if cascade structure is preferred [39].

The accuracy of the attitude control is directly related to inner rate control loop performance if the cascade structure in Figure 3.3 is used. Therefore, designing high performance rate loop is the main motivation in this thesis. Since model based robust control technique will be used, the equivalent model P_o in Figure 3.3 for the inner loop is needed. This model will be obtained from flight tests when the quadrotor is stabilized by manually tuned PI rate and P angle controllers.

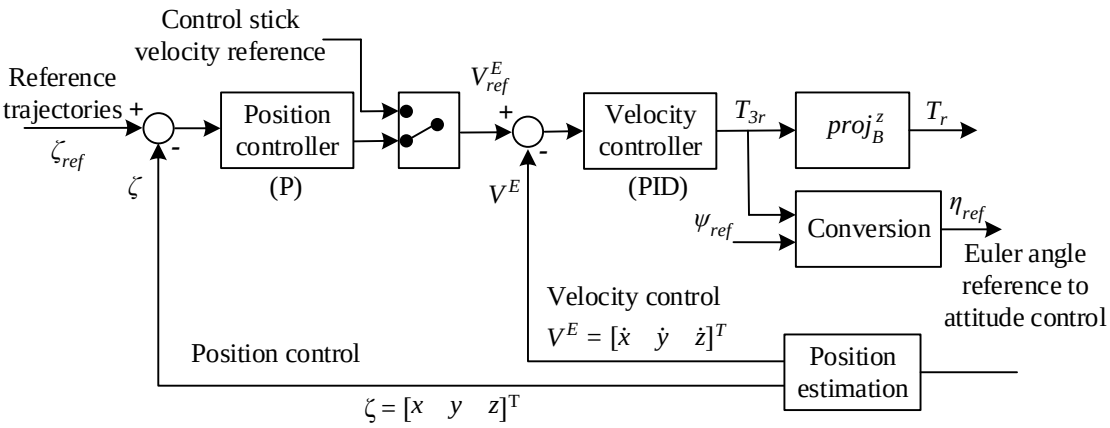

Figure 3.4: Cascade control structure for position control

3.3.2 Quadrotor position controller design

Similar to the attitude control, position control is also formed from nested loops as depicted in Figure 3.4. As discussed in the previous section, the performance of the position loop is directly related to performance of the inner attitude loop. The main motivation of this thesis is to design very high performance robust controller for attitude stabilization. Therefore, translational dynamics are controlled by manually tuned PID and P type controllers which give relatively good performance as shown in Figure 3.4, and special attention is paid for the attitude control case.

CHAPTER 4

ALLOWABLE PARAMETRIC UNCERTAINTY IN CLOSED LOOP FOR THE UNCOMMON QUADROTOR MODEL

In this chapter, which uncertain parameters in the proposed quadrotor model are most critical in terms of robust stability is investigated using μ sensitivities. Later, skewed-μ analysis determines maximum possible uncertainty bounds for model parameters that are difficult to identify accurately.

4.1 Introduction

Mathematical model which is accompanied by an uncertainty model is generally used for control design purpose. If system identification methods are preferred, suitable robust control relevant nominal model with suitable uncertainty representation is needed. By using least squares fitting to experimental data, nominal model can be obtained. Later, model validation method for different input/output measurements determines an uncertainty bound. These methods are used in the following chapters to design flight controller for the proposed quadrotor. If system identification methods are not used, model based on physical principles becomes major selection. In this case, bounds on model parameters are supplied as reported in [40, 41, 42] for a flight mechanics modeling, in [43, 44] for a land vehicle modeling and in [45] for a power system modeling of an electric aircraft. In this chapter, this method is applied to the uncommon quadrotor example.

Understanding which parameters mostly disturb the closed loop stability and performance is essential for robust control. Traditionally, open loop eigenvalue sensitivity analysis is used. However, important parameters for open loop may be completely

different from closed loop after a controller is designed. Moreover, closed loop eigenvalue sensitivity analysis may also provide inadequate information. Closed loop μ sensitivity analysis is useful procedure to determine the parameters that limit the closed loop stability. In addition, some of the parameters in the model are much more difficult to estimate. Therefore, this analysis also determines the maximum allowable uncertainty in these parameters without violating closed loop stability. This is mostly valuable in aerospace control applications where there are large uncertainties in the parameters, and identification tests are difficult and expensive [41]. In this chapter, μ sensitivity and skewed-μ methods are used to determine important parameters and their allowable uncertainty level for closed loop stability for an uncommon quadrotor vehicle in hover conditions.

4.2 Uncertain quadrotor model

Dynamical model of the proposed quadrotor configuration is obtained in Chapter 3 by linearizing nonlinear model in hover conditions. This model is composed of three rotational equations in roll, pitch and yaw axes, and one translational equation in z-axis. There are eight states: roll, pitch and yaw angles $\delta\eta = [\delta\phi\ \delta\theta\ \delta\psi]^T$ all in radian, body frame angular velocities $\delta\Omega = [\delta p\ \delta q\ \delta r]^T$ in radian/second, translational position and velocity in z-axis δz (in meter) and δV_z (in meter/second), respectively. Control is performed through variation in rotor speeds $\delta w = [\delta w_1\ \delta w_2\ \delta w_3\ \delta w_4]^T$ and tilt angle of small rotors $\delta\alpha_2$ and $\delta\alpha_4$. The outputs of this model are $\delta\eta$ corresponding to Euler angles in roll, pitch and yaw axes, and δz corresponding to local position in z-axis. Resulting linearized model in hover for a rigid uncommon quadrotor is given below.

$$\begin{bmatrix} \delta\dot{\Omega} \\ \delta\ddot{z} \end{bmatrix} = \begin{bmatrix} I^{-1} & 0 \\ 0 & m^{-1} \end{bmatrix} \begin{bmatrix} 0 & k_{f_s} l_s & 0 & -k_{f_s} l_s & k_{d_s} w_{eq2} & -k_{d_s} w_{eq4} \\ -k_{f_b} l_b & 0 & k_{f_b} l_b & 0 & k_{f_s} l_{sh} w_{eq2} & k_{f_s} l_{sh} w_{eq4} \\ k_{d_b} & k_{d_s} & -k_{d_b} & -k_{d_s} & -k_{f_s} l_s w_{eq2} & k_{f_s} l_s w_{eq4} \\ k_{f_b} & k_{f_s} & k_{f_b} & k_{f_s} & 0 & 0 \end{bmatrix} \begin{bmatrix} \delta w \\ \delta\alpha_2 \\ \delta\alpha_4 \end{bmatrix} \tag{4.1}$$

$$\delta\dot{\eta} = \delta\Omega \tag{4.2}$$

It is assumed that parameters in this model have 10 percent uncertainty with respect to their nominal values. To give an example, $I_{xx} = \bar{I}_{xx}(1+\sigma_c\delta_1)$ where $\bar{I}_{xx}$ is a nominal value, $\sigma_c = 0.1$ is the percentage of uncertainty and $-1 < \delta_1 < 1$ is the perturbation of this parameter. Uncertain parameters are I_{xx}, I_{yy}, I_{zz}, m, k_{f_s}, l_s, w_{eq2}, w_{eq4}, k_{d_s}, k_{f_b}, l_b, l_{sh} and k_{d_b}, and they are associated with perturbations δ_1, δ_2, δ_3, δ_4, δ_5, δ_6, δ_7, δ_8, δ_9, δ_{10}, δ_{11}, δ_{12} and δ_{13}, respectively.

4.3 Finding LFT representaion

Linear fractional transformation (LFT) plays a central role in robustness analysis and robust control synthesis. Therefore, resulting closed loop should be represented with a standard $M(s)-\Delta(s)$ structure where $M(s)$ contains the dynamics of nominal model and relations of perturbations to closed loop. On the other hand, $\Delta(s)$ is constructed such that it includes all uncertainty blocks. Various LFT representations for different uncertainty structures are investigated in [40, 46]. In this section, general affine state space uncertainty is reviewed.

4.3.1 General affine state space uncertainty

In this section, it is assumed that uncertain model is represented by a state space model with unknown coefficients. Then, main aim is to compute LFT representation with respect to uncertain parameter matrix. Assume a linear system G_δ has the following state space representation, and k uncertain parameters $\delta_1,\ \delta_2,\ \ldots,\ \delta_k$ enter the state space equations in an affine way.

$$\begin{aligned} \dot{x} &= (A + \sum_{i=1}^{k} \delta_i \hat{A}_i)x + (B + \sum_{i=1}^{k} \delta_i \hat{B}_i)u \\ y &= (C + \sum_{i=1}^{k} \delta_i \hat{C}_i)x + (D + \sum_{i=1}^{k} \delta_i \hat{D}_i)u \end{aligned} \tag{4.3}$$

In this representation, A and $\hat{A}_i \in \mathbb{R}^{n\times n}$, B and $\hat{B}_i \in \mathbb{R}^{n\times n_u}$, C and $\hat{C}_i \in \mathbb{R}^{n_y\times n}$, and D and $\hat{D}_i \in \mathbb{R}^{n_y\times n_u}$. State space equations are composed of nominal model represented with state space matrices (A, B, C, D) and effects of uncertainties determined by state space matrices (A_i, B_i, C_i, D_i) for $\delta_i \in [-1\ \ 1],\ i = 1, \ldots, k$. This uncertain

model should be described via LFT so that it can be used in robustness analysis. Corresponding M_δ matrix for perturbation matrix Δ_p can be found by using following method [46].

$$\Delta_p = \text{diag}(\delta_1 I, \delta_2 I, \ldots, \delta_k I) \tag{4.4}$$

Obtaining LFT with the smallest possible size of repeated blocks is essential. For that reason, let q_i denote the rank of matrix

$$P_i := \begin{bmatrix} \hat{A}_i & \hat{B}_i \\ \hat{C}_i & \hat{D}_i \end{bmatrix} \in \mathbb{R}^{(n+n_y)\times(n+n_u)} \tag{4.5}$$

for each $i = 1, \ldots, k$. Then, it is possible to write P_i as

$$P_i = \begin{bmatrix} L_i \\ W_i \end{bmatrix} \begin{bmatrix} R_i \\ Z_i \end{bmatrix}^*, \tag{4.6}$$

where $L_i \in \mathbb{R}^{n\times q_i}$, $W_i \in \mathbb{R}^{n_y\times q_i}$, $R_i \in \mathbb{R}^{n\times q_i}$ and $Z_i \in \mathbb{R}^{n_u\times q_i}$. Therefore, the following equation can be obtained

$$\delta_i P_i = \begin{bmatrix} L_i \\ W_i \end{bmatrix} \begin{bmatrix} \delta_i I_{q_i} \end{bmatrix} \begin{bmatrix} R_i \\ Z_i \end{bmatrix}^*, \tag{4.7}$$

and resulting M_δ can be found as

$$M_\delta = \underbrace{\begin{bmatrix} A & B \\ C & D \end{bmatrix}}_{M_{22}} + \underbrace{\begin{bmatrix} L_i & \ldots & L_k \\ W_i & \ldots & W_k \end{bmatrix}}_{M_{21}} \underbrace{\begin{bmatrix} \delta_1 I_{q_1} & & \\ & \ddots & \\ & & \delta_k I_{q_k} \end{bmatrix}}_{\Delta_p} \underbrace{\begin{bmatrix} R_1^* & Z_1^* \\ \vdots & \vdots \\ R_k^* & Z_k^* \end{bmatrix}}_{M_{12}} \tag{4.8}$$

which can be written as an upper LFT as

$$M_\delta = \mathcal{F}_u\left(\begin{bmatrix} 0 & M_{12} \\ M_{21} & M_{22} \end{bmatrix}, \Delta_p\right). \tag{4.9}$$

Resulting state space uncertainty can be represented as in Figure 4.1 by changing the input order of x and u to the LFT where

$$\begin{aligned} B_2 &= \begin{bmatrix} L_1 & \ldots & L_k \end{bmatrix} \\ D_{12} &= \begin{bmatrix} W_1 & \ldots & W_k \end{bmatrix} \\ C_2 &= \begin{bmatrix} R_1 & \ldots & R_k \end{bmatrix}^* \\ D_{21} &= \begin{bmatrix} Z_1 & \ldots & Z_k \end{bmatrix}^* \\ D_{22} &= 0 \end{aligned}$$

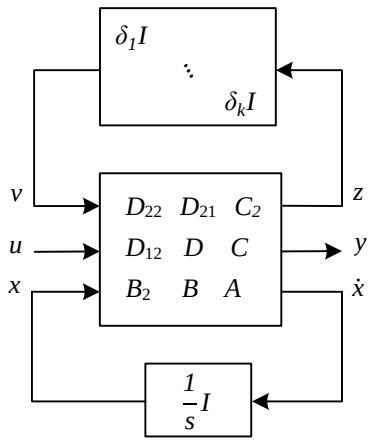

Figure 4.1: LFT representation of state space uncertainty

and

$$G_\delta(\Delta) = \mathcal{F}_l\left(\mathcal{F}_u\left(\begin{bmatrix} 0 & \bar{M}_{12} \\ \bar{M}_{21} & \bar{M}_{22} \end{bmatrix}, \Delta_p\right), \frac{1}{s}I\right) , \tag{4.10}$$

where

$$\left[\begin{array}{c|c} 0 & \bar{M}_{12} \\ \hline \bar{M}_{21} & \bar{M}_{22} \end{array}\right] = \left[\begin{array}{c|cc} D_{22} & D_{21} & C_2 \\ \hline D_{12} & D & C \\ B_2 & B & A \end{array}\right] . \tag{4.11}$$

4.4 LFT representation of uncertain parameters in denominator

When an uncertain parameter is in the denominator, δ_i could not enter state space equations in an affine way. For quadrotor case, $1/I_{xx}$, $1/I_{yy}$, $1/I_{zz}$ and $1/m$ are in this form. These parameters can be represented as a LFT in δ_i as below.

$$\frac{1}{I_{xx}} = \frac{1}{\bar{I}_{xx}(1+\sigma_c\delta_1)} = \frac{1}{\bar{I}_{xx}} - \frac{\sigma_c}{\bar{I}_{xx}}\delta_1(1+\sigma_c\delta_1)^{-1} \tag{4.12}$$

$$\mathcal{F}_u\left(\begin{bmatrix} -\sigma_c & 1 \\ \frac{-\sigma_c}{\bar{I}_{xx}} & \frac{1}{\bar{I}_{xx}} \end{bmatrix}, \delta_1\right) = \frac{1}{\bar{I}_{xx}} - \frac{\sigma_c}{\bar{I}_{xx}}\delta_1(1+\sigma_c\delta_1)^{-1} \tag{4.13}$$

Therefore, with upper LFT of $M_1 = \begin{bmatrix} -\sigma_c & 1 \\ \frac{-\sigma_c}{\bar{I}_{xx}} & \frac{1}{\bar{I}_{xx}} \end{bmatrix}$ with respect to δ_1, $\frac{1}{I_{xx}}$ can be represented where the uncertain parameter is $I_{xx} = \bar{I}_{xx}(1+\sigma_c\delta_1)$. These transforma-

tions together with state space uncertainty are needed to compute overall LFT of the quadrotor model.

4.5 LFT representation of proposed quadrotor model

Uncertain proposed quadrotor model can be represented as a cascade connection of two LFTs corresponding to state space uncertainty and uncertain parameters in the denominator. These systems can be summarized as below.

System 1:

$$\underbrace{\begin{bmatrix} \delta\ddot{\eta} \\ \delta\ddot{z} \end{bmatrix}}_{\dot{x}} = \underbrace{\begin{bmatrix} 0 & k_{f_s}l_s & 0 & -k_{f_s}l_s & k_{d_s}w_{eq2} & -k_{d_s}w_{eq4} \\ -k_{f_b}l_b & 0 & k_{f_b}l_b & 0 & k_{f_s}l_{sh}w_{eq2} & k_{f_s}l_{sh}w_{eq4} \\ k_{d_b} & k_{d_s} & -k_{d_b} & -k_{d_s} & -k_{f_s}l_s w_{eq2} & k_{f_s}l_s w_{eq4} \\ k_{f_b} & k_{f_s} & k_{f_b} & k_{f_s} & 0 & 0 \end{bmatrix}}_{B_1} \underbrace{\begin{bmatrix} \delta w \\ \delta\alpha_2 \\ \delta\alpha_4 \end{bmatrix}}_{u}$$

$$y = x \tag{4.14}$$

System 2:

$$\underbrace{\begin{bmatrix} \delta\dot{\eta} \\ \delta\dot{z} \end{bmatrix}}_{\dot{x}} = \underbrace{\begin{bmatrix} I^{-1} & 0 \\ 0 & m^{-1} \end{bmatrix}}_{B_2} \underbrace{\begin{bmatrix} \delta\dot{\ddot{\eta}} \\ \delta\dot{\ddot{z}} \end{bmatrix}}_{u}$$

$$y = x \tag{4.15}$$

Using cascade connection of LFTs as shown in Figure 4.2, resulting LFT with respect to $\Delta_u = \text{diag}(\Delta_M, \Delta_N)$ can be obtained [47].

$$M_c = \left[\begin{array}{cc|c} M_{11} & M_{12}N_{12} & M_{12}N_{22} \\ 0 & N_{11} & N_{12} \\ \hline M_{21} & M_{22}N_{21} & M_{22}N_{22} \end{array}\right] \tag{4.16}$$

Here, N results from the uncertain System 1 (4.14), and M results from the uncertain System 2 (4.15). Perturbation blocks Δ_M and Δ_N are given as

$$\Delta_M = \text{diag}(\delta_1,\ \delta_1,\ \delta_3,\ \delta_4)\ , \tag{4.17}$$

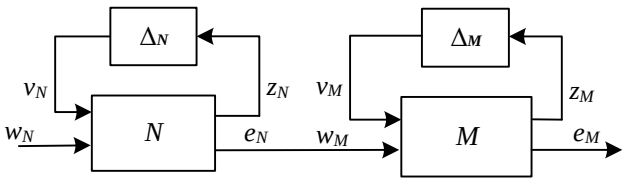

Figure 4.2: Cascade connection of LFTs

$$\Delta_N = \text{diag}(\delta_5 I_4,\ \delta_6 I_2,\ \delta_7 I_3,\ \delta_8 I_3,\ \delta_9 I_2,\ \delta_{10} I_2,\ \delta_{11},\ \delta_{12},\ \delta_{13})\ . \tag{4.18}$$

Resulting cascaded LFT which includes $M_c - \Delta_u$ is the overall uncertain model of the proposed quadrotor configuration. For control design purpose, system model is statically decoupled by using input decoupling (rotor mixing) matrix $T_u = \bar{B}_1^T(\bar{B}_1\bar{B}_1^T)^{-1}$ as shown in Figure 4.5. Therefore, the 4×4 model from $\delta u'$ to δy is obtained. Input decoupling matrix is fixed and calculated by using nominal values of the parameters. Therefore, for nominal case, the following transfer matrix that includes second order inertia and mass lines are obtained.

$$P_{nominal}(s) : \delta u' \rightarrow \delta y = \begin{bmatrix} \frac{1}{I_{xx}\ s^2} & 0 & 0 & 0 \\ 0 & \frac{1}{I_{yy}\ s^2} & 0 & 0 \\ 0 & 0 & \frac{1}{I_{zz}\ s^2} & 0 \\ 0 & 0 & 0 & \frac{1}{m\ s^2} \end{bmatrix} \tag{4.19}$$

This decoupled uncertain model set which is constructed by perturbing each uncertain parameter by 10 percent is visualized by following the method in Chapter 8. The first 3×3 part of the set corresponds to rotational motion, and it is shown in Figure 4.3. Since translational motion in z-axis and rotational motions are inherently decoupled, only 4th diagonal element is given in Figure 4.4. Remaining elements are zero, and they are not shown.

Closed loop system is constructed using manual loop shaping controller based on PI and lead filter as depicted in Figure 4.5.

Remark 4.1. System 1 in (4.14) has multiplication of uncertain parameters, e.g., $k_{f_s} l_s$. These are not suitable for an affine state space uncertainty, and they should be represented with a cascade connection of LFTs corresponding to each uncertain parameter. Therefore, high order perturbations in these multiplications are neglected

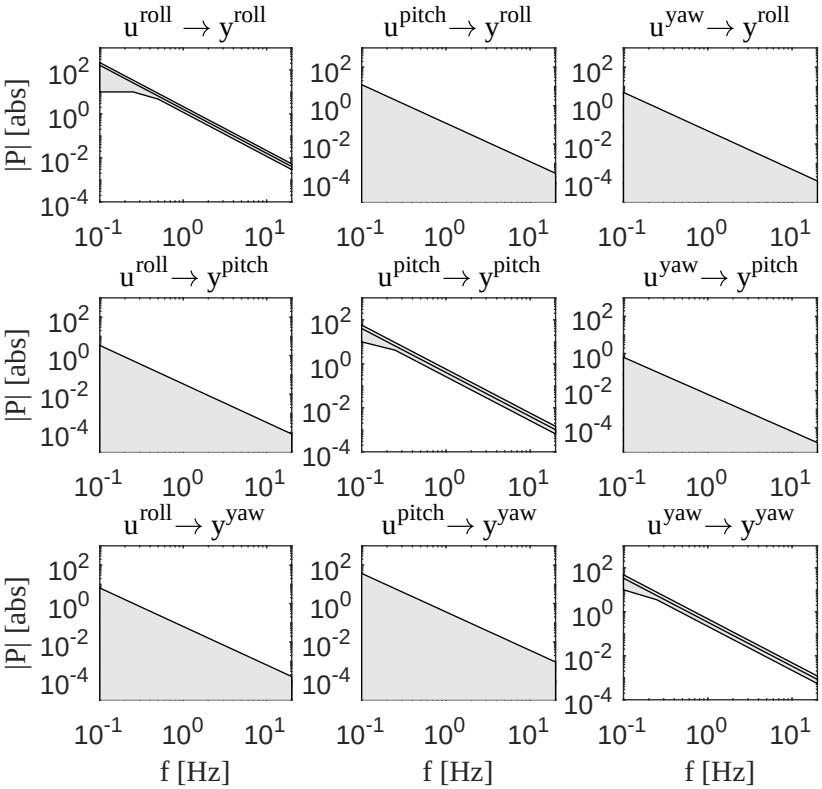

Figure 4.3: Rotational motion part: Magnitudes of nominal model (solid black), uncertain model set (shaded).

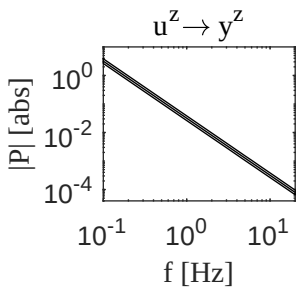

Figure 4.4: Translational motion in z-axis part: Magnitudes of nominal model (solid black), uncertain model set (shaded).

to obtain uncertain model easily using state space uncertainty without causing large error.

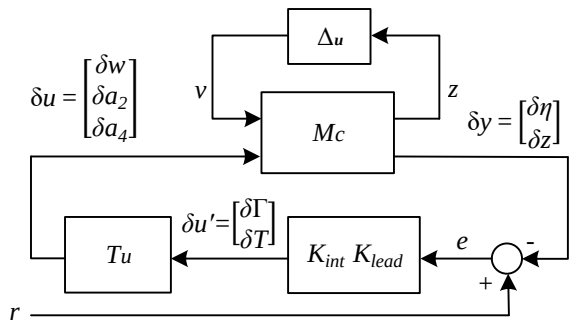

Figure 4.5: Feedback configuration for uncertain system

Similar simplifications as given below are also used for other multiplications of uncertain parameters.

$$\begin{aligned} k_{f_s} l_s &= \left(\bar{k}_{f_s}(1+\sigma_c\delta_5)\right)\left(\bar{l}_s(1+\sigma_c\delta_6)\right) \\ &= \bar{k}_{f_s}\bar{l}_s + \bar{k}_{f_s}\bar{l}_s(\sigma_c\delta_5 + \sigma_c\delta_6 + \sigma_c^2\delta_5\delta_6) \\ &\approx \bar{k}_{f_s}\bar{l}_s + \bar{k}_{f_s}\bar{l}_s(\sigma_c\delta_5 + \sigma_c\delta_6) \end{aligned} \tag{4.20}$$

Similarly, multiplication of three uncertain parameters, e.g., $k_{f_s} l_{sh} w_{eq2}$ is approximated as below.

$$k_{f_s} l_{sh} w_{eq2} \approx \bar{k}_{f_s}\bar{l}_{sh}\bar{w}_{eq2} + \bar{k}_{f_s}\bar{l}_{sh}\bar{w}_{eq2}(\sigma_c\delta_4 + \sigma_c\delta_7 + \sigma_c\delta_{12}) \tag{4.21}$$

4.6 Sensitivity analysis of the proposed quadrotor

Standard quadrotor configuration and proposed configuration both have zero state transition matrix A in the state space equations. Since A matrix is not affected from perturbed parameters, standard open loop eigenvalue sensitivity analysis fails to provide any result. Therefore, closed loop eigenvalue sensitivity analysis is more suitable for this case. Therefore, suitable controller is needed for both closed loop eigenvalue and μ sensitivity analyses. Controller is designed using manual loop shaping principles as described in [48, 49]. As discussed previously, axes of the plant decouple with the rotor mixing matrix. Therefore, controller for each axis can be designed separately. Following procedure can be readily applied to all axes. Firstly, suitable bandwidth which corresponds to crossover frequency f_{bw} is selected. Since each diagonal entry of the decoupled plant is of double-Integrator type, sufficient phase

lead is required. This is satisfied using a lead filter $K_{lead} = p_{lead}\frac{\frac{s}{2\pi\frac{1}{3}f_{bw}}+1}{\frac{s}{2\pi 3 f_{bw}}+1}$. p_{lead} is adjusted to satisfy $|GK_{lead}(2\pi f_{bw})| = 1$. With the lead filter, compensated loop satisfies -1 slope in the crossover region which is essential for sufficient robustness. Next, for command tracking and disturbance rejection, PI controller is added with integral cut-off at $f_{bw}/5$ to keep the phase margin unaffected due to zero at $f_{bw}/5$, i.e., $K_{int} = \frac{s+2\pi\frac{f_{bw}}{5}}{s}$. $K = K_{int}K_{lead}$ is the resulting controller for one axis. In this way, 42° phase margin and infinite gain margin are achieved in each channel. Selected f_{bw} is 2 Hz for roll and pitch axes of rotational motion. For yaw axis, f_{bw} is selected as 0.4 Hz. For translational motion in z-axis, 0.25 Hz is aimed. Overall diagonal (decentralized) multiple input multiple output (MIMO) controller is obtained by putting single input single output (SISO) controllers at the diagonal entries according to axis order. This controller is used during closed loop sensitivity analysis.

Parameters of the proposed quadrotor are selected as in Table 4.1 which is the modified version of the standard quadrotor parameters in [38].

Closed loop eigenvalue sensitivity is performed using average of the eigenvalue sensitivities as

Table 4.1: Physical parameters of the proposed quadrotor configuration

Total weight of the vehicle	m	$0.8\ kg$
Gravitational acceleration	g	$9.81\ m/s^2$
Moment of inertia along x-axis	I_{xx}	$15.67 \times 10^{-3}\ kgm^2$
Moment of inertia along y-axis	I_{yy}	$62.68 \times 10^{-3}\ kgm^2$
Moment of inertia along z-axis	I_{zz}	$75.20 \times 10^{-3}\ kgm^2$
Big arm length of the quadrotor	l_b	$0.6\ m$
Small arm length of the quadrotor	l_s	$0.3\ m$
Thrust factor of big rotor	k_{f_b}	$769.28 \times 10^{-7}\ N/(rad/s)^2$
Thrust factor of small rotor	k_{f_s}	$192.32 \times 10^{-7}\ N/(rad/s)^2$
Drag factor of big rotor	k_{d_b}	$16.012 \times 10^{-7}\ Nm/(rad/s)^2$
Drag factor of small rotor	k_{d_s}	$4.003 \times 10^{-7}\ Nm/(rad/s)^2$
Small rotor speed in hover	$w_{eq2},\ w_{eq4}$	$(110)^2\ (rad/s)^2$
Distance from the mass center to small rotor along z-axis	l_{sh}	$0.03\ m$

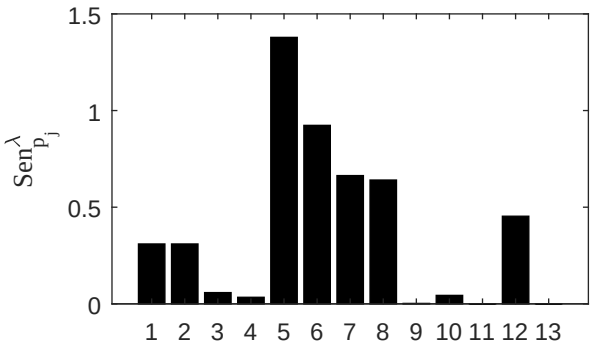

Figure 4.6: Closed loop eigenvalue sensitivity analysis

$$Sen^{\lambda}_{p_j} = \frac{1}{16}\sum_{i=1}^{16} Sen^{\lambda_i}_{p_j} \tag{4.22}$$

for each parameter where the sensitivity of the ith eigenvalue $\lambda_i,\ i = 1, \ldots, 16$ to variations in the jth parameter $p_j,\ j = 1, \ldots, 13$ is defined as

$$Sen^{\lambda_i}_{p_j} = \frac{\partial \lambda_i(p)}{\partial p_j} \approx \frac{|\lambda_i(p + \Delta p_j) - \lambda_i(p)|}{\Delta p_j}\ . \tag{4.23}$$

16 closed loop eigenvalues result from combination of 8 plant and 8 controller eigenvalues. Figure 4.6 shows the eigenvalue sensitivities for each uncertain parameter when $\delta_j = 1$ which corresponds to 10 percent perturbation in each uncertain parameter. According to eigenvalue sensitivity analysis, uncertain parameters k_{f_s}, l_s, w_{eq2}, w_{eq4} and l_{sh} (i.e., δ_5, δ_6, δ_7, δ_8 and δ_{12}) have rather large effects on closed loop eigenvalues. In addition, I_{xx} and I_{yy} (i.e., δ_1 and δ_2) have equal effects on closed loop dynamics since controller is designed to obtain equal closed loop performance in roll and pitch axes. On the other hand, effects of I_{zz}, m, k_{d_s}, k_{f_b}, l_b and k_{d_b} (i.e., δ_3, δ_4, δ_9, δ_{10}, δ_{11} and δ_{13}) to this closed loop are small. Different controller selection may change the sensitivities; however, the relative importances of the parameters remain the same if similar control performances are aimed for all axes.

The aim of the sensitivity analysis is to measure a change in a system behavior due to parameter perturbations. In eigenvalue sensitivity analysis, a system behavior is determined by a change in eigenvalues. If a system behavior is determined by a structured singular value μ, relative importance of uncertain parameters on system robustness can be found using μ sensitivities. Robust performance [50] and robust stability [41] can be selected for μ sensitivity analysis. Following tests determine robust stability (RS) and robust performance (RP) for the system depicted in Figure 4.7 where M is

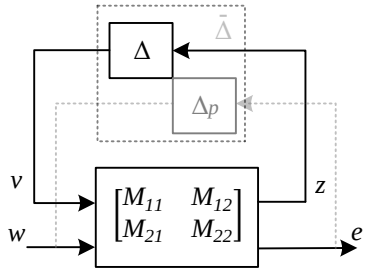

Figure 4.7: M - Δ block structure

internally stable [51].

$$\text{RS} \Leftrightarrow \mu_{\Delta}(M_{11}) < 1,\ \forall w \tag{4.24}$$

$$\text{RP} \Leftrightarrow \mu_{\bar{\Delta}}(M) < 1,\ \forall w,\ \bar{\Delta} = \text{diag}(\Delta, \Delta_p) \tag{4.25}$$

For RP, μ sensitivity of the jth parameter p_j is defined as

$$Sen^{\mu}_{p_j} = \frac{\partial \mu(M)}{\partial p_j} \approx \frac{\mu(M_\epsilon) - \mu(M)}{\Delta p_j}\ , \tag{4.26}$$

where M_ϵ denotes a perturbed system, and Δp_j denotes a percentage change of an associated normalized parameter. For that, each $\delta_i I_i$ is multiplied by a_i, where each a_i is real and nominally one except for the jth perturbed scalar $a_j = 1 + \epsilon$. Therefore, following matrix is useful.

$$a = \text{diag}(I_1,\ I_2,\ \ldots,\ a_j I_j,\ \ldots,\ I_{k-1},\ I_k) \tag{4.27}$$

Instead of using $a\Delta$ for original M, a can be absorbed into M, and perturbed system M_ϵ is obtained for original Δ.

$$M_\epsilon = \begin{bmatrix} aM_{11} & aM_{12} \\ M_{21} & M_{22} \end{bmatrix} \tag{4.28}$$

Positive ϵ corresponds to non-decreasing function $\mu(M_\epsilon)$ which implies that μ sensitivities are always non-negative.

Similarly, for RS, μ sensitivity of the jth parameter p_j is defined as

$$Sen^{\mu}_{p_j} = \frac{\partial \mu(M_{11})}{\partial p_j} \approx \frac{\mu(aM_{11}) - \mu(M_{11})}{\Delta p_j}\ . \tag{4.29}$$

In this Chapter, variations of the parameters to robust stability is investigated, and the definition (4.29) is used.

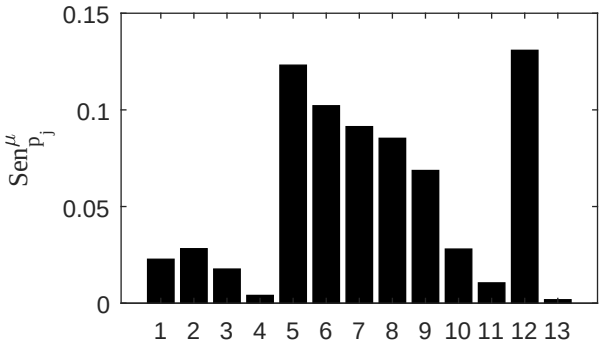

Figure 4.8: μ sensitivity analysis

Remark 4.2. In practice, μ lower or upper bound is used instead of μ since exact calculation of μ is NP-hard [52]. Upper bound gives (possibly conservative) maximum allowable size of uncertainty to satisfy robustness requirements, whereas lower bound gives the smallest uncertainty which violates robustness requirements. During μ sensitivity analysis, upper bound is used since the computation of upper bound is convex, i.e., only minimum is global. Using μ upper bound in sensitivity analysis can give different values from exact sensitivity values; however, the relative importances of the uncertain parameters on robust stability or performance are not affected [41, 50, 53].

μ sensitivities are calculated by using a mixed upper-bound μ algorithm [54] and perturbing each normalized parameter by 0.5 which corresponds to 5 percent (0.5 σ_c = 0.05) deviation of original parameter from the nominal value. Figure 4.8 shows the μ sensitivities for each uncertain parameter. Uncertain parameters k_{f_s}, l_s, w_{eq2}, w_{eq4}, k_{d_s} and l_{sh} (i.e., δ_5, δ_6, δ_7, δ_8, δ_9 and δ_{12}) are more important in terms of robust stability. These parameters were also important in terms of closed loop eigenvalues except k_{d_s} and l_{sh} which were less important for closed loop eigenvalue sensitivity. Importances of the remaining parameters on robust stability and closed loop eigenvalue sensitivity differ. Therefore, traditional eigenvalue sensitivity analysis may fail to find critical parameters in terms of closed loop stability. In the next section, allowable level of uncertainty for each parameter will be investigated. Skewed-μ analysis will be used for that purpose [41]. Knowledge of parameters that are difficult to obtain will be used while combining parameters which will be perturbed and fixed as discussed in the next section.

4.7 Control oriented uncertainty modeling

Skewed structured singular value, $\mu_{s,\bar{\Delta}}$, of a matrix M with respect to uncertain matrix $\bar{\Delta}$,

$$\bar{\Delta} = \begin{bmatrix} \Delta_v & 0 \\ 0 & \Delta_f \end{bmatrix} , \tag{4.30}$$

is defined as

$$\mu_{s,\bar{\Delta}} = \left(\min\{\bar{\sigma}(\Delta_v) \mid \bar{\sigma}(\Delta_f) \leq 1,\ \det(I - M\bar{\Delta}) = 0\}\right)^{-1} . \tag{4.31}$$

Skewed structured singular value is valuable if some partitions of the uncertainty block are already known, and minimization is performed over the unknown parts. In this section, $\mu_{s,\bar{\Delta}}$ is used to find maximum allowable size of uncertainty block Δ_v without violating robust stability when the remaining part $\bar{\sigma}(\Delta_f) \leq 1$, i.e., parameters in this portion are allowed to vary in $\sigma_c = 0.1 = 10\%$. In this way, maximum possible perturbations of the parameters which are difficult or costly to estimate can be found, while remaining parameters are within 10% bound.

In the uncommon quadrotor dynamic model, thrust constants k_{f_s} and k_{f_b}, rotor drag constants k_{d_s} and k_{d_b} and square of small rotor speeds in hover w_{eq2} and w_{eq4} are the parameters which are most difficult and costly to estimate. In addition, variations of these parameters are large since these parameters are affected from environmental conditions and battery voltage. Therefore, maximum allowable perturbations for these parameters, k_{f_s}, w_{eq2}, w_{eq4}, k_{d_s}, k_{f_b} and k_{d_b} (i.e., δ_5, δ_7, δ_8, δ_9, δ_{10} and δ_{13}), are investigated while remaining parameters are kept within 10% uncertainty bound. Similarly, maximum allowable perturbations for k_{f_s}, k_{f_b}, k_{d_s} and k_{d_b} (i.e., δ_5, δ_9, δ_{10} and δ_{13}) are also analyzed by assuming that w_{eq2} and w_{eq4} can be estimated online during hovering. Initial uncertainty bounds for all normalized parameters are 10% corresponding to $\sigma_c = 0.1$. During this analysis, mixed lower-bound skewed-μ algorithm in [54] is used.

Six models are selected such that Δ_f and Δ_v are constructed with different combinations of uncertain parameters. In model 1, all uncertain parameters are in Δ_v which turns skewed-μ into standard μ lower bound computation. Model 2, 3, 4 and 5 are constructed by increasing the number of parameters which are easy to estimate or measure in Δ_f. In addition to the parameters that are easy to estimate, w_{eq2} and w_{eq4}

Table 4.2: Models for skewed-μ analysis

Model	Δ_f	Δ_v
1	$\{-\}$	$\{\delta_1, \delta_2, \delta_3, \delta_4, \delta_5, \delta_6, \delta_7, \delta_8, \delta_9, \delta_{10}, \delta_{11}, \delta_{12}, \delta_{13}\}$
2	$\{\delta_1, \delta_3\}$	$\{\delta_2, \delta_4, \delta_5, \delta_6, \delta_7, \delta_8, \delta_9, \delta_{10}, \delta_{11}, \delta_{12}, \delta_{13}\}$
3	$\{\delta_1, \delta_2, \delta_3, \delta_4\}$	$\{\delta_5, \delta_6, \delta_7, \delta_8, \delta_9, \delta_{10}, \delta_{11}, \delta_{12}, \delta_{13}\}$
4	$\{\delta_1, \delta_2, \delta_3, \delta_4, \delta_6, \delta_{11}\}$	$\{\delta_5, \delta_7, \delta_8, \delta_9, \delta_{10}, \delta_{12}, \delta_{13}\}$
5	$\{\delta_1, \delta_2, \delta_3, \delta_4, \delta_6, \delta_{11}, \delta_{12}\}$	$\{\delta_5, \delta_7, \delta_8, \delta_9, \delta_{10}, \delta_{13}\}$
6	$\{\delta_1, \delta_2, \delta_3, \delta_4, \delta_6, \delta_7, \delta_8, \delta_{11}, \delta_{12}\}$	$\{\delta_5, \delta_9, \delta_{10}, \delta_{13}\}$

(i.e., δ_7 and δ_8) are also placed in Δ_f in model 6, and allowable perturbation for the remaining parameters are computed. These six models are illustrated in Table 4.2.

In Table 4.3, worst-case parameter combinations for all six models are given using mixed lower-bound skewed-μ algorithm in [54]. Relative uncertainty bounds between different uncertain parameters corresponding to six models are illustrated. In Table 4.3, values given in bold correspond to six parameters which are the most difficult to identify.

It is observed that model 1, 2 and 3 result in a similar destabilizing perturbation norm. For example, when δ_1, δ_2, δ_3 and δ_4 are in Δ_f, worst-case perturbation occurs at $\bar{\sigma}_c = 2.90$. This corresponds to allowable 29% uncertainty ($\bar{\sigma}_c \sigma_c = 0.29$) for δ_5, δ_6, δ_7, δ_8, δ_9, δ_{10}, δ_{11}, δ_{12} and 28.5% uncertainty for δ_{13} for robust stability. In this model 3 case, I_{xx}, I_{yy} and I_{zz} have 10% percent allowable uncertainty. However, worst-case performance occurs when $\delta_4 = 0.001$. This illustrates that 0.01% uncertainty in m is tolerable. As given in model (4.1), remaining uncertain parameters in Δ_v are divided by I_{xx}, I_{yy}, I_{zz} and m. Therefore, allowable perturbations for I_{xx}, I_{yy}, I_{zz} and m tend to be smaller when allowable perturbations in the remaining parameters increase. Table 4.3 shows that worst-case perturbations of models occur when some of the allowable uncertainties are small for I_{xx}, I_{yy}, I_{zz} and m which are in the denominator. On the contrary, norms of the remaining parameters in the numerator are maximized. Therefore, to tolerate large uncertainties in the remaining parameters, these physical parameters should be measured accurately.

Table 4.3: Worst-case parameter combinations for skewed-μ analysis models

Model	δ_1	δ_2	δ_3	δ_4	δ_5	δ_6	δ_7	δ_8	δ_9	δ_{10}	δ_{11}	δ_{12}	δ_{13}
1	-2.77	-2.89	2.74	0.07	**-2.90**	-2.90	**2.90**	**-2.90**	**2.90**	**2.90**	2.90	-2.90	**-2.83**
2	-1.00	2.90	-1.00	0.001	**-2.90**	-2.90	**2.90**	**-2.90**	**2.90**	**2.90**	2.90	-2.90	**-2.85**
3	-1.00	1.00	-1.00	0.001	**-2.90**	-2.90	**2.90**	**-2.90**	**2.90**	**2.90**	2.90	-2.90	**-2.85**
4	0.17	-0.73	0.43	0.18	**-3.33**	-0.79	**-3.33**	**-3.33**	**2.64**	**-3.33**	-1.00	-3.33	**3.33**
5	0.23	0.95	-0.99	0.001	**-3.93**	-1.00	**3.93**	**-3.93**	**3.93**	**3.93**	1.00	-1.00	**-2.62**
6	0.02	0.99	-0.99	0.001	**-6.14**	-1.00	**1.00**	**-1.00**	**6.14**	**6.14**	1.00	-1.00	**-6.14**

When δ_6 and δ_{11} are added to Δ_f corresponding to model 4, tolerable uncertainty rises to 3.33. In other words, $(\bar{\sigma}_c\sigma_c = 3.33 \times 0.1)$ 33.3% uncertainty is allowed for k_{f_s}, w_{eq2}, w_{eq4}, k_{f_b}, l_{sh}, k_{d_b} and 26.4% for k_{d_s}. For this case, I_{xx}, I_{yy}, I_{zz}, m , l_s and l_b are need to known with 1.7%, 7.3%, 4.3%, 1.8%, 7.9% and 10% error, respectively. In model 5, l_{sh} is added to Δ_f part, and allowed perturbation in the remaining parameters rises to 39.3% except k_{d_b} which is limited to 26.2%. In model 6, 61.4% uncertainty in k_{f_s}, k_{f_b}, k_{d_s} and k_{d_b} are tolerable, if I_{xx}, I_{yy}, I_{zz}, m , l_s, w_{eq2}, w_{eq4}, l_b and l_{sh} are known with 0.2%, 9.9%, 9.9%, 0.01%, 10%, 10%, 10%, 10% and 10% error, respectively. Therefore, by reducing the uncertainties in easily measurable parameters, large variations in the remaining uncertain parameters which are difficult or expensive to identify are allowed.

4.8 Comments

As shown in Figure 4.3, parameter perturbations induce significant dynamics at the off-diagonal elements of statically decoupled plant model with constant input decoupling matrix T_u. Worst-case perturbations usually occur when these coupling dynamics destabilize the corresponding axis. If larger variations in the parameters are desired, coupling effects due to perturbations should be analyzed carefully. In addition, finding easily measurable parameters with very small uncertainty allows larger variations in the remaining parameters. In this way, effort and budget required to obtain parameters that are difficult to estimate can be reduced.

CHAPTER 5

COMBINED IDENTIFICATION AND ROBUST CONTROL

In this chapter, robust-control-relevant identification problem is introduced. Estimating nominal model and constructing robust-control-relevant model are explained by following the outline in [27].

5.1 Problem formulation

During problem formulation following notations are used. The notation P is used to denote any linear time invariant system which may represent the actual plant P_o, or the nominal model $\hat{P}$. Moreover, $\mathcal{P}$ and C denote the model set and the feedback controller respectively. Finally, $\mathcal{H}_\infty$-norm based performance measure selection gives a control criterion $J(P, C)$ as

$$J(P, C) = \|WT(P, C)V\|_\infty \tag{5.1}$$

where $W = \text{diag}(W_y, W_u)$ and $V = \text{diag}(V_2, V_1)$ are bistable weighting filters and transfer matrix $T(P, C)$ is the mapping defined as (5.2) corresponding to feedback configuration in Figure 5.1.

$$T(P, C) : \begin{bmatrix} r_2 \\ r_1 \end{bmatrix} \rightarrow \begin{bmatrix} y \\ u \end{bmatrix} = \begin{bmatrix} P \\ I \end{bmatrix} (I + CP)^{-1} \begin{bmatrix} C & I \end{bmatrix} \tag{5.2}$$

The aim of the norm-based control design is to find and optimal controller C^{opt} such that following performance cost is minimized.

$$C^{\text{opt}} = \arg\min_C J(P_o, C) \tag{5.3}$$

Since P_o is unknown, the optimal controller (5.3) can not be found. In order to represent the actual plant dynamics accurately, a model set $\mathcal{P}$ is constructed such that

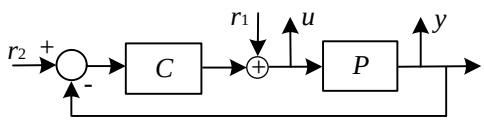

Figure 5.1: Feedback configuration

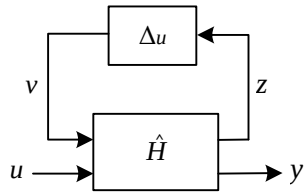

Figure 5.2: Model set

$$P_o \in \mathcal{P}. \tag{5.4}$$

Then, the worst-case performance for this model set $\mathcal{P}$ is defined as

$$J_{WC}(\mathcal{P}, C) = \sup_{P \in \mathcal{P}} J(P, C). \tag{5.5}$$

Robust control design aims to minimize this worst-case performance criterion.

$$C^{\text{RP}} = \arg\min_{C} J_{WC}(\mathcal{P}, C) \tag{5.6}$$

Then, the following performance bound for the true plant P_o is the basis for joint identification and robust control [27, 55].

$$J(P_o, C^{\text{RP}}) \leqslant J_{WC}(\mathcal{P}, C^{\text{RP}}) \tag{5.7}$$

The performance guaranteed by (5.7) depends on the shape and size of the model set $\mathcal{P}$, and it is structured using upper linear fractional transformation (LFT) as

$$\mathcal{P} = \left\{ P \mid P = \mathcal{F}_u(\hat{H}, \Delta_u), \Delta_u \in \mathbf{\Delta_u} \right\} \tag{5.8}$$

where the upper LFT is defined as

$$\mathcal{F}_u(\hat{H}, \Delta_u) = \hat{H}_{22} + \hat{H}_{21}\Delta_u(I - \hat{H}_{11}\Delta_u)^{-1}\hat{H}_{12}. \tag{5.9}$$

$\hat{H}$ which is shown in Figure 5.2 essentially contains the nominal model $\hat{P}$ and the uncertainty structure. In addition, $\mathcal{H}_\infty$-norm-bounded perturbation $\Delta_u \in \mathbf{\Delta_u} \subseteq \mathcal{RH}_\infty$ in (5.10) is considered [25, 55].

$$\mathbf{\Delta_u} = \{\Delta_u \in \mathcal{RH}_\infty \mid \|\Delta_u\|_\infty \leqslant \gamma\} \tag{5.10}$$

Therefore, low complexity model set $\mathcal{P}$ which leads to non-conservative control design and small performance bound (5.7) is needed. Specific coprime factor based approach eventually satisfies these two requirements [26, 56].

5.2 Robust-control-relevant identification

The minimization of performance bound (5.7) can not be solved explicitly, and the value of $J_{WC}(\mathcal{P}, C^{\text{RP}}(\mathcal{P}))$ mainly depends on the shape and size of $\mathcal{P}$. However, separate nominal model identification and uncertainty modeling steps can be used jointly to reach approximate solution [27].

5.2.1 Uncertainty structure for robust control

Robust-control-relevant model set should give a small bound (5.7) for high robust performance. Therefore, the following identification criterion selection is considered.

$$\min_{\mathcal{P}} J_{WC}(\mathcal{P}, C^{\text{exp}}) \tag{5.11}$$
$$\text{subject to (5.4)}$$

Herein, C^{exp} denotes the controller which is used during identification experiment. Criterion (5.11) is reasonable since it includes both control objective $J_{WC}(\mathcal{P}, C)$ and experimental conditions regarding the stabilization of the system with C^{exp} during identification experiment. It can also be considered as a minimization of an upper bound for the resulting control synthesis as

$$J_{WC}(\mathcal{P}, C^{\text{RP}}) \leq J_{WC}(\mathcal{P}, C^{\text{exp}}) \ . \tag{5.12}$$

If the difference between these two values in (5.12) is large, C^{exp} and $\mathcal{P}$ can be updated iteratively by solving (5.6) and (5.11) similar to the iterative identification methods introduced in [57, 58]. Since iterative identification and control using model set gives monotonically improved performance, the effect of initial controller usage C^{exp} instead of C^{RP} is greatly reduced after several iterations [25]. In this thesis, similar performances for C^{RP} and initial controller C^{exp} are assumed, and no iteration is used. In other words, (5.11) is minimized only once for the initial controller C^{exp}.

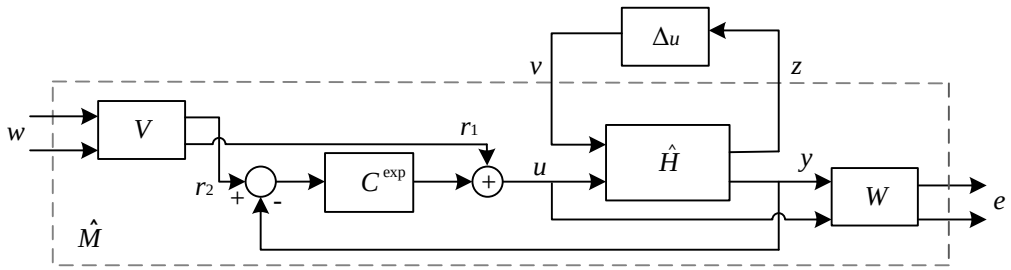

Figure 5.3: General control structure for worst-case performance evaluation

The uncertainty structure selection is important to simplify the minimization of (5.11). Let the LFT description of $\mathcal{P}$ is augmented with weights and C^{exp} as in Figure 5.3. Then, worst-case performance evaluation leads to the following equation.

$$\begin{aligned} J_{WC}(\mathcal{P}, C^{\text{exp}}) &= \sup_{\Delta_u \in \mathbf{\Delta_u}} \|\mathcal{F}_u(\hat{M}, \Delta_u)\|_\infty \\ &= \sup_{\Delta_u \in \mathbf{\Delta_u}} \|\hat{M}_{22} + \hat{M}_{21}\Delta_u(I - \hat{M}_{11}\Delta_u)^{-1}\hat{M}_{12}\|_\infty \end{aligned} \tag{5.13}$$

Selection of the model set which is composed of plants stabilized by C^{exp} simplifies (5.13) and gives bounded performance. This is achieved by using dual-Youla-Kucera uncertainty structure (5.14) which requires coprime factorization approach.

Right coprime factorization (RCF) of $\hat{P}$ is denoted by the pair $\{\hat{N}, \hat{D}\}$ if $\hat{D}$ is invertible, $\hat{N}, \hat{D} \in \mathcal{RH}_\infty$, $\hat{P} = \hat{N}\hat{D}^{-1}$, and $\exists X_r, Y_r \in \mathcal{RH}_\infty$ satisfying Bezout identity $X_r\hat{D} + Y_r\hat{N} = I$. Similarly, it is assumed that the stabilizing controller C^{exp} has a RCF $\{N_c, D_c\}$.

$$\mathcal{P}^{\text{DY}} = \left\{ P \mid P = (\hat{N} + D_c\Delta_u)(\hat{D} - N_c\Delta_u)^{-1}, \Delta_u \in \mathbf{\Delta_u} \right\} \tag{5.14}$$

Associated with Figure 5.2, this model set can be illustrated as in Figure 5.4. Therefore, this structure has the LFT representation (5.15), and upper LFT of it gives the model set (5.14).

$$\hat{H}^{\text{DY}} = \left[\begin{array}{c|c} \hat{D}^{-1}N_c & \hat{D}^{-1} \\ \hline \hat{P}N_c + D_c & \hat{P} \end{array}\right] \tag{5.15}$$

Evaluation of $\hat{H}^{\text{DY}}$ in the feedback connection shown in Figure 5.3 gives a LFT representation (5.16).

$$\hat{M}^{\text{DY}}(\hat{P}, C^{\text{exp}}) = \left[\begin{array}{c|c} 0 & (\hat{D} + C^{\text{exp}}\hat{N})^{-1}\begin{bmatrix} C^{\text{exp}} & I \end{bmatrix} V \\ \hline W\begin{bmatrix} D_c \\ -N_c \end{bmatrix} & WT(\hat{P}, C^{\text{exp}})V \end{array}\right] \tag{5.16}$$

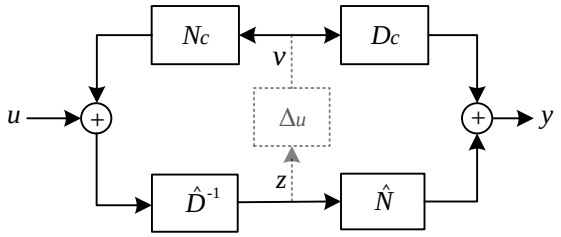

Figure 5.4: LFT representation of the set defined by (5.14)

Therefore, worst-case performance (5.11) reduces to an affine function in Δ_u and becomes bounded.

$$J_{WC}(\mathcal{P}^{\text{DY}}, C^{\text{exp}}) = \sup_{\Delta_u \in \mathbf{\Delta_u}} \|\hat{M}_{22} + \hat{M}_{21}\Delta_u\hat{M}_{12}\|_\infty \tag{5.17}$$

Even if bounded performance is reached, the minimization of (5.17) is not clear due to existence of frequency dependent $\hat{M}_{21}$ and $\hat{M}_{12}$ terms. This can be further simplified in the next sections by selecting specific coprime factorization of C^{exp} [25].

5.2.2 Nominal model identification

Minimization of (5.11) is achieved by first identifying nominal model $\hat{P}$ according to certain criteria, followed by an uncertainty modeling step. Therefore, control-relevant nominal modeling requires tight model set such that designed and achieved performance are close to each other. The triangle equality is the basis of the nominal model identification criterion [58, 59].

$$J(P_o, C) \leq J(\hat{P}, C) + \|W(T(P_o, C) - T(\hat{P}, C))V\|_\infty \tag{5.18}$$

The first term on the right is related to model based control design, whereas the second term corresponds to a performance degradation term since the controller C is designed for $\hat{P}$ instead of P_o. This performance degradation term is evaluated for the controller C^{exp} that is used during identification experiment to find a nominal model suitable to (5.11). Therefore, nominal model identification aims to minimize the following criterion.

$$\min_{\hat{P}} \|W(T(P_o, C^{\text{exp}}) - T(\hat{P}, C^{\text{exp}}))V\|_\infty \tag{5.19}$$

Dual-Youla-Kucera based uncertainty structure requires coprime factors of $\hat{P}$. In fact, specific coprime factorization introduced in [56] connects nominal model identification (5.19) and identification of these coprime factors.

Let $\{\tilde{N}_e, \tilde{D}_e\}$ be a left coprime factorization (LCF) of $[C^{\text{exp}} V_2 \; V_1]$ with a co-inner numerator, i.e., $\tilde{N}_e \tilde{N}_e^* = I$, where $\tilde{N}_e = [\tilde{N}_{e,2} \; \tilde{N}_{e,1}]$. This type of coprime factorization can be obtained directly by following the procedures in [60, 46] when C^{exp}, V_1 and V_2 are known. Then, robust-control-relevant identification criterion (5.19) reduces to a robust-control-relevant coprime factor identification problem as

$$\min_{\hat{N},\hat{D}} \|W \left(\begin{bmatrix} N_o \\ D_o \end{bmatrix} - \begin{bmatrix} \hat{N} \\ \hat{D} \end{bmatrix} \right) \tilde{N}_e\|_\infty \; , \tag{5.20}$$
$$\text{subject to } \hat{N}, \hat{D} \in \mathcal{RH}_\infty$$

where $\{\hat{N}, \hat{D}\}$ and $\{N_o, D_o\}$ denote the coprime factors for $\hat{P}$ and P_o respectively, and they are defined as [56]

$$\begin{bmatrix} N \\ D \end{bmatrix} = \begin{bmatrix} P \\ I \end{bmatrix} (\tilde{D}_e + \tilde{N}_{e,2} V_2^{-1} P)^{-1} \; . \tag{5.21}$$

Since $\tilde{N}_e$ is coinner that does not affect the $\mathcal{H}_\infty$-norm, it can be omitted from (5.20). The original problem is approximately solved at a discrete frequency grid $w_i \in \Omega$ of finite time experiment. By using the appropriate parametrization θ for $[\hat{N}^T(\theta) \; \hat{D}^T(\theta)]^T$, the problem can be reduced to (5.22), where the solution minimizes a lower bound of the $\mathcal{H}_\infty$ norm of (5.20).

$$\min_{\theta} \; \max_{w_i \in \Omega} \bar{\sigma} \left(W \left(\begin{bmatrix} N_o(w_i) \\ D_o(w_i) \end{bmatrix} - \begin{bmatrix} \hat{N}(\theta, w_i) \\ \hat{D}(\theta, w_i) \end{bmatrix} \right) \right) \tag{5.22}$$
$$\text{subject to } \hat{N}, \hat{D} \in \mathcal{RH}_\infty$$

$T(P_o, C^{\text{exp}})$ can be obtained from frequency response estimation. Therefore, from (5.19) and (5.20), nonparametric estimate of $\{N_o, D_o\}$ can be obtained as

$$\begin{bmatrix} \tilde{N}_o \\ \tilde{D}_o \end{bmatrix} = \tilde{T}(P_o, C^{\text{exp}}) V \tilde{N}_e^* \; , \tag{5.23}$$

where $\tilde{T}(P_o, C^{\text{exp}})$ and $\{\tilde{N}_o, \tilde{D}_o\}$ denote the nonparametric estimates. Estimates $\{\tilde{N}_o, \tilde{D}_o\}$ are used during minimization of (5.22) instead of true $\{N_o, D_o\}$.

5.2.2.1 Optimization problem

To solve this optimization problem, first a suitable parametrization is needed such that $\hat{N}, \hat{D} \in \mathcal{RH}_\infty$ and $\{\hat{N}, \hat{D}\}$ must be a RCF. Therefore, the following parametrization is introduced in [55, 56]

$$\begin{bmatrix} \hat{N}(\theta) \\ \hat{D}(\theta) \end{bmatrix} = \begin{bmatrix} B(\theta) \\ A(\theta) \end{bmatrix} (\tilde{D}_e A(\theta) + \tilde{N}_{e,2} V_2^{-1} B(\theta))^{-1} , \tag{5.24}$$

where $B \in \mathbb{R}^{n_y \times n_u}[z]$ and $A \in \mathbb{R}^{n_u \times n_u}[z]$ are polynomial matrices. Therefore, $\hat{P}$ is parametrized as a right matrix fraction description (MFD) and satisfy

$$\hat{P}(\theta) = \hat{N}(\theta)\hat{D}(\theta)^{-1} = B(\theta)A(\theta)^{-1}, \tag{5.25}$$

where the MFDs are parametrized linearly in the parameters as (5.26).

$$\text{vec}\left(\begin{bmatrix} B(\theta) \\ A(\theta) \end{bmatrix}\right) = \sum_j \varphi_j \theta_j \tag{5.26}$$

This polynomial vector is linear in parameters $\theta = [\theta_0^T\ \theta_1^T \ldots]^T$ and $\theta_j \in \mathbb{R}^{(n_y+n_u)n_u \times 1}$ and $\varphi_j \in \mathbb{R}^{(n_y+n_u)n_u \times (n_y+n_u)n_u}[z]$.

Finally, the non-smooth and non-convex optimization problem is converted to non-linear least squares problem using Lawson's algorithm for $\mathcal{L}_\infty$ approximation [61] as discussed in [62].

Algorithm 5.1. Set $\theta^{\langle 0 \rangle} = 0$ and $w_i^{\langle 0 \rangle} = \frac{1}{n_w}$, where n_w is the number of frequency in Ω. Iterate over k until the algorithm converges to a solution.

$$\theta^{\langle k \rangle} = \arg\min_\theta \sum_i w_i^{\langle k \rangle} \|\epsilon_i(\theta)\|_F^2 \tag{5.27}$$

$$\text{where } w_i^{\langle k \rangle} = \frac{\bar{\sigma}\left(\epsilon_i(\theta^{\langle k \rangle})\right) w_i^{\langle k-1 \rangle}}{\sum_i \bar{\sigma}\left(\epsilon_i(\theta^{\langle k \rangle})\right) w_i^{\langle k-1 \rangle}} \tag{5.28}$$

The nonlinear least squares problem (5.27) is solved by using Lawson's algorithm, and sequence of weighting functions $w_i^{\langle k \rangle}$ are used to minimize (5.20). Finally, the problem is reduced to nonlinear least squares problem,

$$\sum_i \|W_h^{\langle k \rangle} \circ \left(W\left(\begin{bmatrix} N_o \\ D_o \end{bmatrix} - \begin{bmatrix} \hat{N}(\theta) \\ \hat{D}(\theta) \end{bmatrix}\right)\right)\|_F^2 \tag{5.29}$$

where $\circ$ denote the Hadamard product, an element-by-element multiplication, and elements of $W_h^{\langle k \rangle}$ are equal to $\sqrt{w_i^{\langle k \rangle}}$. Using the following rules from Kronecker calculus and parametrization (5.24), (5.29) can be written as [55, 63, 64]

- $\diamond$ $\|A\|_F = \|\text{vec}(A)\|_2$
- $\diamond$ $\text{vec}(ABC) = (C^T \otimes A)\text{vec}(B)$
- $\diamond$ $\text{vec}(A \circ B) = \text{diag}(\text{vec}(A))\text{vec}(B)$

$$\sum_i \|W_{\text{lsq},i}^{\langle k \rangle}(\theta)\text{vec}\left(\begin{bmatrix} B(\theta) \\ A(\theta) \end{bmatrix}\right)\|_2^2 \,, \tag{5.30}$$

where

$$\begin{aligned} W_{\text{lsq},i}^{\langle k \rangle}(\theta) = \text{diag}\left(\text{vec}(W_h^{\langle k \rangle})\right) \Bigg(& \left[(\tilde{D}_e A(\theta) + \tilde{N}_{e,2} V_2^{-1} B(\theta))^{-1}\right]^T \\ & \otimes \left[W\left(\begin{bmatrix} N_o \tilde{N}_{e,2} V_2^{-1} & N_o \tilde{D}_e \\ D_o \tilde{N}_{e,2} V_2^{-1} & D_o \tilde{D}_e \end{bmatrix} - I\right)\right]\Bigg). \end{aligned} \tag{5.31}$$

The nonlinear least squares problem (5.30) can be approximately solved by applying Sanathanan-Koerner iterations [65]. This idea is used by introducing a new iteration index $\langle f \rangle$ which gives

$$\sum_i \|W_{\text{lsq},i}^{\langle k \rangle}(\theta^{\langle f-1 \rangle})\text{vec}\left(\begin{bmatrix} B(\theta^{\langle f \rangle}) \\ A(\theta^{\langle f \rangle}) \end{bmatrix}\right)\|_2^2. \tag{5.32}$$

Consequently, the nonlinear least squares problem (5.29) is recast as an iteratively solvable linear least squares problem

$$\min_{\theta^{\langle f \rangle}} \|W_{\text{lsq}}^{\langle k \rangle}(\theta^{\langle f-1 \rangle})\Phi\theta^{\langle f \rangle}\|_2^2 \,, \tag{5.33}$$

where

$$W_{\text{lsq}}^{\langle k \rangle} = \text{diag}\left(W_{\text{lsq},1}^{\langle k \rangle},\ W_{\text{lsq},2}^{\langle k \rangle},\ \ldots\right), \tag{5.34}$$

$$\Phi = [\ \varphi(w_1)^T\ \varphi(w_2)^T\ \ldots]^T. \tag{5.35}$$

If the estimate of the SK iterations is further used as an initial estimate in the subsequent Gauss-Newton optimization step, the numerical conditioning of the problem becomes important. Standard monomial basis selection for Φ generally gives very large condition number $\kappa(.) = \frac{\bar{\sigma}(.)}{\underline{\sigma}(.)}$ of the matrix $W_{\text{lsq}}^{\langle k \rangle}\Phi$, and accurate solution can

not be found. This problem can be resolved by selecting polynomial basis that are orthonormal with respect to data-dependent inner product (5.36) [55].

$$\langle \varphi_m, \varphi_l \rangle_{W\text{lsq}} = \sum_i \varphi_m(w_i)^* \, W_{\text{lsq},i}^{\langle k \rangle^*} \, W_{\text{lsq},i}^{\langle k \rangle} \, \varphi_l(w_i) \tag{5.36}$$

This selection makes $\kappa(W_{\text{lsq}}^{\langle k \rangle}\Phi) = 1$ and leads to optimally conditioned problem. These orthonormal polynomials can be computed efficiently by following the procedure described in [29] which is an extension of the method suggested in [66, 67]. When the result of the SK iterations is used as an initial estimate, the Gauss-Newton iterations remain close to optimal for the nonlinear least squares problem (5.30), and accurate parametric coprime factors can be obtained.

5.3 Robust-control-relevant model set

In this section, the final step of the robust-control-relevant identification is discussed. Firstly, (W_u, W_y)-normalized coprime factorization satisfying (5.37) of C^{exp} is needed [25].

$$\begin{bmatrix} W_u N_c \\ W_y D_c \end{bmatrix}^* \begin{bmatrix} W_u N_c \\ W_y D_c \end{bmatrix} = I \tag{5.37}$$

This factorization can be obtained by first finding normalized coprime factors $\{\bar{N}, \bar{D}\}$ of $W_u C W_y^{-1}$ as discussed in [46]. Then, $\{N_c, D_c\} = \{W_u^{-1}\bar{N}, W_y^{-1}\bar{D}\}$ gives the (W_u, W_y)-normalized coprime factors of C^{exp}. Finally, the robust-control-relevant model set $\mathcal{P}^{\text{RCR}}$ is derived from dual-Youla uncertainty structure (5.14) with a specific choice of $\{\hat{N}, \hat{D}\}$ in (5.21) and $\{N_c, D_c\}$ in (5.37) as

$$\mathcal{P}^{\text{RCR}} = \left\{ P \mid P \in \mathcal{P}^{\text{DY}}, \{\hat{N}, \hat{D}\} \text{ satisfies (5.21)} \, , \, \{N_c, D_c\} \text{ satisfies (5.37)} \right\}. \tag{5.38}$$

The LFT representation given in (5.16) for the feedback connection in Figure 5.3 is now updated for these particular coprime factors as

$$\hat{M}^{\text{RCR}} = \left[\begin{array}{c|c} 0 & \begin{bmatrix} \tilde{N}_{e,2} & \tilde{N}_{e,1} \end{bmatrix} \\ \hline \begin{bmatrix} W_y D_c \\ -W_u N_c \end{bmatrix} & WT(\hat{P}, C^{\text{exp}})V \end{array} \right]. \tag{5.39}$$

When the worst-case performance in (5.17) is evaluated for $\mathcal{P}^{\text{RCR}}$, it leads to

$$J_{WC}(\mathcal{P}^{\text{RCR}}, C^{\text{exp}}) = \sup_{\Delta_u \in \mathbf{\Delta_u}} \|M_{22}^{\text{RCR}} + M_{21}^{\text{RCR}} \Delta_u M_{12}^{\text{RCR}}\|_\infty \tag{5.40}$$

$$\leqslant \|M_{22}^{\text{RCR}}\|_\infty + \sup_{\Delta_u \in \mathbf{\Delta_u}} \|M_{21}^{\text{RCR}} \Delta_u M_{12}^{\text{RCR}}\|_\infty \tag{5.41}$$

$$= J(\hat{P}, C^{\text{exp}}) + \gamma \,. \tag{5.42}$$

Norm preserving properties of M_{12}^{RCR} and M_{21}^{RCR} give the result (5.42). It shows that uncertainty bound γ directly affects the worst-case performance $J_{WC}(\mathcal{P}^{\text{RCR}}, C^{\text{exp}})$. In other words, nominal model identification (5.19) for the uncertain model $\mathcal{P}^{\text{RCR}}$ (5.38) and quantification of model uncertainty Δ_u together give the robust-control-relevant model set in terms of (5.11) [27, 68].

If arbitrary coprime factorizations are used while constructing model set $\mathcal{P}^{\text{DY}}$, norm-preserving properties of M_{12}^{DY} and M_{21}^{DY} do not hold. Therefore, resulting $J_{WC}(\mathcal{P}^{\text{DY}}, C^{\text{exp}})$ may be large, and conservatism may exist in the identification step [27].

CHAPTER 6

NUMERICALLY RELIABLE IDENTIFICATION USING DATA-DEPENDENT ORTHONORMAL POLYNOMIALS

Typical parametric identification problem can be converted into a weighted least squares (LS) optimization problem. Therefore, numerical conditioning of the problem determines the accuracy of least squares estimation. It is well known that as the frequency grid, number of input-output size and order of estimation become large, problem turns into ill-conditioned form when the standard monomial basis is used. Therefore, polynomial basis should be constructed considering problem specific data. To reach optimal numerical conditioning of the least squares problem, data-dependent orthonormal polynomials are introduced in [29] which is an extension of the method suggested in [66, 67]. In this chapter, firstly this method which is developed for single-input single-output (SISO) systems is reviewed. Later, this method is modified for coprime factors identification and multiple-input multiple-output (MIMO) cases. One can also construct polynomial basis by following alternative techniques introduced in [69, 70] to improve the numerical conditioning of the resulting LS problem.

6.1 Problem formulation

6.1.1 Frequency domain system identification

In Chapter 5, least squares approximations $\{\hat{N}(z), \hat{D}(z)\}$ of frequency response functions (FRF) $\{N_o, D_o\}$ are needed. However, problem is formulated for more general case, where identified FRF is P_o and LS approximant is $\hat{P}(z)$. Moreover, identification of SISO systems is considered to simplify the presentation. Next, problem formulation is extended for identification of MIMO systems. Required modifications

to a SISO system solution method are clarified to apply it to a MIMO system case. Let $\{z_k = e^{j\alpha_k}\}_{k=1}^m$ be a set of ordered complex nodes on the unit circle satisfying $0 < \alpha_1 < ... < \alpha_m < \pi$. In addition, $P_o(z_k)$ is FRF of the system, and $W(z_k)$ is the corresponding weight set. Model $\hat{P}(z)$ is parametrized as

$$\hat{P}(z,\theta) = \frac{\hat{N}(z,\theta)}{\hat{D}(z,\theta)} \tag{6.1}$$

where $\hat{N}(z,\theta), \hat{D}(z,\theta) \in \mathbb{R}[z]$ are parametrized linearly using polynomial basis functions $\{\varphi_j\}_{j=0}^l$ as

$$\begin{bmatrix} \hat{D}(z,\theta) \\ \hat{N}(z,\theta) \end{bmatrix} = \sum_{j=0}^{l} \varphi_j \theta_j = \begin{bmatrix} \varphi_0 & \varphi_1 & ... & \varphi_l \end{bmatrix} \theta \tag{6.2}$$

where $\theta_j \in \mathbb{R}^{2\times 1}$, $\varphi_j \in \mathbb{R}^{2\times 2}[z]$ and $\theta = [\theta_0^T \ \theta_1^T \dots \ \theta_l^T]^T$. Then, weighted LS approximation to P_o can be obtained by minimizing the following error criterion [29].

$$\begin{aligned} &\arg\min_{\hat{P}} = \|W(P_o - \hat{P})\|_2^2 := \\ &\arg\min_{\theta} \sum_{k=1}^{m} \left[\left(P_o(z_k) - \frac{\hat{N}(z_k,\theta)}{\hat{D}(z_k,\theta)} \right)^* W(z_k)^* \, W(z_k) \left(P_o(z_k) - \frac{\hat{N}(z_k,\theta)}{\hat{D}(z_k,\theta)} \right) \right] \end{aligned} \tag{6.3}$$

Since (6.3) is nonlinear in $\hat{D}(z_k,\theta)$, it is not easy to solve. This problem can be approximately solved by applying Sanathanan-Koerner (SK) iterations [65]. This idea is used by introducing iteration index $\langle f \rangle$ which gives a new error criterion as

$$\arg\min_{\theta} \sum_{k=1}^{m} = \| \frac{W(z_k)}{\hat{D}(z_k,\theta^{\langle f-1 \rangle})} \begin{bmatrix} P_o(z_k) & -1 \end{bmatrix} \begin{bmatrix} \hat{D}(z_k,\theta^{\langle f \rangle}) \\ \hat{N}(z_k,\theta^{\langle f \rangle}) \end{bmatrix} \|_2^2. \tag{6.4}$$

LS problem (6.4) is now linear in $[\hat{D}(z_k,\theta^{\langle f \rangle}) \ \hat{N}(z_k,\theta^{\langle f \rangle})]^T$, and it can be solved more easily. SK iterations can be initialized by choosing $\hat{D}(\theta^{\langle 0 \rangle}) = 1$.

6.1.2 Numerically reliable identification

The polynomial least squares problem (6.4) is equivalent to finding the solution of the following linear least squares problem

$$W_{\text{lsq}} \Phi_{l-1} \theta = W_{\text{lsq}} b \ , \tag{6.5}$$

where $\theta = [\ \theta_0^T\ \theta_1^T\ \ldots\ \theta_{l-1}^T\ ]^T$, θ_l is determined to satisfy monic denumerator polynomial $\hat{D}(z)$ to avoid trivial solution,

$$\Phi_{l-1} = \begin{bmatrix} \varphi_0(z_1) & \varphi_1(z_1) & \ldots & \varphi_{l-1}(z_1) \\ \varphi_0(z_2) & \varphi_1(z_2) & \ldots & \varphi_{l-1}(z_2) \\ \vdots & \vdots & & \vdots \\ \varphi_0(z_m) & \varphi_1(z_m) & \ldots & \varphi_{l-1}(z_m) \end{bmatrix}, \tag{6.6}$$

$$b = \Big[(\varphi_l(z_1)\ \theta_l)^T \quad (\varphi_l(z_2)\ \theta_l)^T \quad \ldots \quad (\varphi_l(z_m)\ \theta_l)^T\Big]^T\ , \tag{6.7}$$

$$W_{\text{lsq}} = \text{diag}\,(w_1, w_2, ..., w_m)\,, \tag{6.8}$$

$$w_k = \left(\frac{W(z_k)}{\hat{D}(z_k, \theta^{\langle f-1\rangle})}[P_o(z_k)\ -1]\right), \tag{6.9}$$

which depends on weights W_{lsq} and basis functions Φ_{l-1}. The matrix $W_{\text{lsq}}\Phi_{l-1}$ can be very ill-conditioned depending on the basis functions. It is notoriously ill-conditioned if monomial basis $\varphi_j(z) = I_2\ z^j$ is used giving Vandermonde matrix (6.10), and it degrades identification algorithm performance.

$$\Phi_{l-1} = \begin{bmatrix} I_2 & I_2\ z_1 & I_2\ z_1^2 & \ldots & I_2\ z_1^{l-1} \\ I_2 & I_2\ z_2 & I_2\ z_2^2 & \ldots & I_2\ z_2^{l-1} \\ \vdots & \vdots & & \vdots & \\ I_2 & I_2\ z_m & I_2\ z_m^2 & \ldots & I_2\ z_m^{l-1} \end{bmatrix} \tag{6.10}$$

Well-conditioned $W_{\text{lsq}}\Phi_{l-1}$ can be obtained by considering problem data in W_{lsq} while selecting basis functions. In other words, data-dependent basis functions should be used. If basis functions that are orthonormal with respect to certain data-dependent inner product are used, the optimal conditioning of $W_{\text{lsq}}\Phi_{l-1}$ can be achieved [29, 70].

6.2 Data-dependent orthonormal polynomials

As stated previously, polynomial basis selection is important for numerical conditioning of the LS problems. In this respect, using data-dependent inner product to construct the basis is essential. This section specifically deals with data-dependent discrete inner product and polynomial basis construction method.

6.2.1 Discrete orthonormal polynomials

Orthonormal block polynomials (OBPs) are defined as a set of block polynomials $\{\varphi_j(z)\}_{j=0}^{l} \in \mathbb{C}^{2\times 2}[z]$ that are orthonormal with respect to data-dependent inner product in (6.11)

$$\langle \varphi_p, \varphi_q \rangle = \sum_{k=1}^{m} \varphi_p(z_k)^H \; w_k^H \; w_k \; \varphi_q(z_k) = \delta_{pq} \; I_2 \; , \tag{6.11}$$

where δ_{pq} is the Kronecker delta function, $\{w_k\}_{k=1}^{m} \in \mathbb{C}^{1\times 2}$, and degree of $\varphi_j(z)$ is j.

$$\Phi_{l-1}^H W_{\text{lsq}}^H W_{\text{lsq}} \Phi_{l-1} = I_{2l} \tag{6.12}$$

Therefore, (6.12) is obtained which indicates the unitary matrix $W_{\text{lsq}}\Phi_{l-1}$ and $\kappa(W_{\text{lsq}}\Phi_{l-1}) = 1$, which is the aim of the numerically reliable identification.

6.2.2 Estimation of real-rational transfer functions

For physical system modeling mapping between real inputs and real outputs requires transfer functions with real coefficients. Polynomials $\{\hat{N}(z), \hat{D}(z)\}$ should also have real coefficients. This is assured by selecting basis polynomials $\varphi_j(z)$ with real coefficients. Polynomials with real coefficients satisfy

$$\varphi(z_k^*) = \varphi(z)^*. \tag{6.13}$$

Therefore, following equality follows (6.11) for real polynomials.

$$\langle \varphi_p, \varphi_q \rangle^* = \sum_{k=1}^{m} \varphi_p(z_k^*)^H \; (w_k^H \; w_k)^* \; \varphi_q(z_k^*) = \delta_{pq} \; I_2 \tag{6.14}$$

Therefore, it is required to add the nodes $\{z_k^*\}_{k=1}^{m}$ and corresponding weights $\{w_k^*\}_{k=1}^{m}$ to original problem. Then, corresponding discrete inner product for real OBPs $\{\varphi_j(z)\}_{j=0}^{l} \in \mathbb{R}^{2\times 2}[z]$ for m nodes $\{z_k\}_{k=1}^{m}$ and weights $\{w_k\}_{k=1}^{m}$ is defined as [29]

$$\langle \varphi_p, \varphi_q \rangle = 2 \text{ Re } \left\{ \sum_{k=1}^{m} \varphi_p(z_k)^H \; w_k^H \; w_k \; \varphi_q(z_k) \right\}. \tag{6.15}$$

6.3 Polynomial recurrence relations

Set of OBPs $\{\varphi_j(z)\}_{j=0}^{l}$ can be computed using three-term-recurrence relations

$$\varphi_j(z) = \left(z\varphi_{j-1}(z) + \tilde{\varphi}_{j-1}(z)\,\Gamma_j\right)\,\Sigma_j^{-1}, \tag{6.16}$$

$$\tilde{\varphi}_j(z) = \left(z\varphi_{j-1}(z)\,\Gamma_j^T + \tilde{\varphi}_{j-1}(z)\right)\,\hat{\Sigma}_j^{-T}, \tag{6.17}$$

where $\Gamma_j, \Sigma_j, \hat{\Sigma}_j \in \mathbb{R}^{2\times 2}$ are predetermined recursion parameters. The recursion is initialized with $\varphi_0 = \tilde{\varphi}_0 = \Sigma_0^{-1}$. Since coefficients are real, resulting OBPs $\{\varphi_j(z)\}_{j=0}^{l} \in \mathbb{R}^{2\times 2}[z]$ are satisfied. These recursion coefficients ,$\Gamma_j, \Sigma_j, \hat{\Gamma}_j, \hat{\Sigma}_j \in \mathbb{R}^{2\times 2}$, are block Schur parameters satisfying the following proposition [29]

$$\begin{bmatrix} -\Gamma_j & \hat{\Sigma}_j \\ \Sigma_j & \hat{\Gamma}_j \end{bmatrix}^T \begin{bmatrix} -\Gamma_j & \hat{\Sigma}_j \\ \Sigma_j & \hat{\Gamma}_j \end{bmatrix} = I_4\ , \tag{6.18}$$

where Σ_j is an upper triangular matrix having positive diagonal elements. When Γ_j is known, remaining parameters can be obtained. Σ_j can be obtained as follows using (6.18)

$$\Sigma_j = \text{chol}(I_2 - \Gamma_j^T\Gamma_j)\ , \tag{6.19}$$

where $L = \text{chol}(A)$ denotes the Cholesky factorization of A satisfying $LL^T = A$. Other block Schur blocks, $\hat{\Gamma}_j$ and $\hat{\Sigma}_j$ are found using singular value decomposition of $[-\Gamma_j^T\ \Sigma_j^T]$ as described in [29]. Since V is unitary and parameters are real, proposition (6.18) holds for this decomposition.

$$USV^T = \begin{bmatrix} I_2 \end{bmatrix} \begin{bmatrix} I_2 & 0_2 \end{bmatrix} \begin{bmatrix} -\Gamma_j & \hat{\Sigma}_j \\ \Sigma_j & \hat{\Gamma}_j \end{bmatrix}^T = \begin{bmatrix} -\Gamma_j^T & \Sigma_j^T \end{bmatrix} \tag{6.20}$$

In the next section, inverse eigenvalue problem is introduced for nodes $\{z_k\}_{k=1}^{m}$ and weights $\{w_k\}_{k=1}^{m}$ to find block Schur parameters.

6.4 Hessenberg recurrence matrix

Polynomial recurrance relations (6.16) and (6.17) indicate that OBPs are linearly independent due to degree constraint, i.e., degree of $\varphi_j(z)$ is j. Therefore the block

polynomial $z\varphi_{k-1}(z)$ can be written as a linear combination of the polynomials $\{\varphi_j(z)\}_{j=0}^{k}$ as

$$z\varphi_{k-1}(z) = \eta_{k,k-1}\varphi_k(z) + ... + \eta_{0,k-1}\varphi_0(z) \tag{6.21}$$

where $\eta_{\times,\times} \in \mathbb{R}^{2\times 2}$ and $\eta_{k,k-1}$ is upper triangular with positive diagonal elements due to degree constraint. Equation (6.21) can be written in a matrix form as

$$z\begin{bmatrix}\varphi_0(z) & ... & \varphi_{k-1}(z)\end{bmatrix} = \begin{bmatrix}\varphi_0(z) & ... & \varphi_k(z)\end{bmatrix} H_{2(k+1)\times 2k} \tag{6.22}$$

Evaluation of (6.22) on the nodes gives

$$Z\Phi_{m-1} = \Phi_{m-1}H, \tag{6.23}$$

where $Z \in \mathbb{C}^{2m\times 2m}$ is defined as (6.24) and $H \in \mathbb{R}^{2m\times 2m}$ is an upper 2×2-block Hessenberg matrix and it satisfies $H_{i,j} = 0\ \forall\ i \geq j+3$. Moreover, 2nd subdiagonal of H is strictly positive, i.e., $H_{i+2,i} > 0$ for $i = 1, ..., 2m-2$ [29, 70]. Recurrence coefficients should be derived from H to compute OBPs.

6.5 Inverse eigenvalue problem

Please note that node z_k^* and corresponding weight tuple w_k^* are added to the original problem to derive real polynomials. Let the node matrix $Z \in \mathbb{C}^{2m\times 2m}$ and the weight matrix $W \in \mathbb{C}^{2m\times 2}$ be defined as

$$Z = \text{diag}(z_1,\ z_1^*,\ z_2,\ z_2^*, ...,\ z_m,\ z_m^*), \tag{6.24}$$

$$W = [w_1^T\ w_1^H\ w_2^T\ w_2^H\ ...\ w_m^T\ w_m^H]^T. \tag{6.25}$$

Then, there exist a unitary matrix $Q \in \mathbb{C}^{2m\times 2m}$ satisfying the inverse eigenvalue problem as [29, 67]

$$\begin{bmatrix} I_2 & \\ & Q^H \end{bmatrix} \left[\begin{array}{c|c} 0_2 & W^T \\ \hline W & Z \end{array}\right] \begin{bmatrix} I_2 & \\ & Q \end{bmatrix} = \left[\begin{array}{c|cc} 0_2 & \Sigma_0^T & 0_{2\times(2m-2)} \\ \hline \Sigma_0 & & \\ 0_{(2m-2)\times 2} & & H \end{array}\right]. \tag{6.26}$$

Since all nodes are on the unit circle, Z is unitary matrix. Therefore, $H \in \mathbb{R}^{2m\times 2m}$ is unitary Hessenberg matrix, and it can be decomposed into its elementary block-Givens-reflectors as [29, 71]

$$H = G_1\, G_2 \ldots\, G_{m-1}\, \bar{G}_m\ , \tag{6.27}$$

where G_j is defined as

$$G_j = I_{2(j-1)} \oplus \begin{bmatrix} -\Gamma_j & \hat{\Sigma}_j \\ \Sigma_j & \hat{\Gamma}_j \end{bmatrix} \oplus I_{2m-2(j+1)} \ , \tag{6.28}$$

$$\bar{G}_m = I_{2m-2} \oplus -\Gamma_m \ ,$$

where $\Gamma_j, \Sigma_j, \hat{\Sigma}_j, \hat{\Gamma}_j \in \mathbb{R}^{2\times 2}$ are block Schur parameters and $\oplus$ denotes direct sum defined as

$$A \oplus B = \begin{bmatrix} A & 0 \\ 0 & B \end{bmatrix} \ . \tag{6.29}$$

6.6 Computation of OBPs

Inverse eigenvalue problem (6.26) can be solved by matrix zeroing operations. Each column of initial node-weight matrix can be converted into block-Hessenberg form using Householder reflections. Therefore, series of Householder reflections form the unitary matrix Q.

6.6.1 Obtaining required real block-Schur parameters

In the previous section, node z_k^* and corresponding weight tuple w_k^* are added to the original problem to enforce real block-Schur parameters. Instead of dealing with complex node and weight matrices, real matrices can be introduced into (6.26) by introducing unitary matrix R_0

$$R_0 = I_m \otimes \frac{1}{\sqrt{2}} \begin{bmatrix} 1 & j \\ 1 & -j \end{bmatrix} , \tag{6.30}$$

where $\otimes$ denotes the Kronecker product and $j = \sqrt{-1}$. Corresponding unitary similarity transform is defined as

$$\left[\begin{array}{c|c} 0_2 & W_{real}^T \\ \hline W_{real} & Z_{real} \end{array}\right] = \begin{bmatrix} I_2 & \\ & R_0^H \end{bmatrix} \left[\begin{array}{c|c} 0_2 & W^T \\ \hline W & Z \end{array}\right] = \begin{bmatrix} I_2 & \\ & R_0 \end{bmatrix} , \tag{6.31}$$

where $Z_{real} \in \mathbb{R}^{2m\times 2m}$ and $W_{real} \in \mathbb{R}^{2m\times 2}$ are defined as

$$Z_{real} = \begin{bmatrix} \begin{bmatrix} \cos\alpha_1 & -\sin\alpha_1 \\ \sin\alpha_1 & \cos\alpha_1 \end{bmatrix} & & \\ & \ddots & \\ & & \begin{bmatrix} \cos\alpha_m & -\sin\alpha_m \\ \sin\alpha_m & \cos\alpha_m \end{bmatrix} \end{bmatrix}, \tag{6.32}$$

$$W_{real} = \sqrt{2}\ \left[\text{Re}\{w_1^T\}\ \text{Im}\{w_1^T\}\ ...\ \text{Re}\{w_m^T\}\ \ \text{Im}\{w_m^T\}\right]^T, \tag{6.33}$$

where $z_k = e^{j\alpha_k}$ and w_k defined in (6.9). 2×2-block Hessenberg matrix can be obtained from real node-weight matrix (6.32) by real zeroing operations [29].

Let $M \in \mathbb{R}^{k\times k}$ be a matrix to be considered. Element $M_{i,j}$ for $i \geq j+1$, can be zeroed by applying similarity transform GMG, where symmetric Givens reflector G is defined as

$$G = \begin{bmatrix} I_{i-2} & & & \\ & -a & b & \\ & b & a & \\ & & & I_{k-i}, \end{bmatrix}. \tag{6.34}$$

$$a = -M_{i-1,j}/\sqrt{M_{i-1,j}^2 + M_{i,j}^2}$$

$$b = M_{i,j}/\sqrt{M_{i-1,j}^2 + M_{i,j}^2}$$

After Hessenberg matrix is obtained with Givens reflections, block Schur parameters can be derived by applying following method.

First two-columns of H and G_1 are equal as shown in (6.35).

$$H = G_1\, G_2 \ldots\, \bar{G}_m = G_1\, G' = \left[\begin{array}{c|c} -\Gamma_1 & ... \\ \Sigma_1 & ... \\ 0_{(2m-4)\times 2} & ... \end{array}\right], \tag{6.35}$$

Premultiplying unitary H with G_1^H gives a new unitary matrix H_2' as

$$G_1^H\ H = G' = \left[\begin{array}{c|c} I_2 & 0_{2\times(2m-2)} \\ \hline 0_{(2m-2)\times 2} & H_2' \end{array}\right]. \tag{6.36}$$

H_2' has the same block structure as H except for the reduced dimensions.

$$H_2' = \left[\begin{array}{c|c} -\Gamma_2 & \dots \\ \Sigma_2 & \dots \\ 0_{(2m-6)\times 2} & \dots \end{array}\right] , \tag{6.37}$$

Therefore, the same method can also be obtained for H_2'. For each new H_j', new block Schur parameters Γ_j and Σ_j can be extracted. Since Γ_j and Σ_j satisfy (6.19) at this point, (6.20) is used to derive remaining parameters $\hat{\Gamma}_j$ and $\hat{\Sigma}_j$. When all block Schur parameters are available, OBPs are obtained using recurrence relations (6.16) and (6.17).

6.6.2 Remarks

Remark 6.1. Alternative efficient computation method of OBPs is discussed in [29]. As the frequency grid, number of input-output size and order of estimation become large, this fast method reduces the total estimation time.

Remark 6.2. m node frequency grid $\{z_k = e^{j\alpha_k}\}_{k=1}^{m}$, m OBPs $\{\varphi_j\}_{j=0}^{m-1}$ can be obtained by deriving m block Schur parameters $\{\Gamma_j, \Sigma_j, \hat{\Gamma}_j, \hat{\Sigma}_j\}_{j=1}^{m}$ from Hessenberg matrix $H \in \mathbb{R}^{2m\times 2m}$. However, order of estimation l is usually too small compared to number of node m.

$$\begin{bmatrix} \hat{D}(z,\theta) \\ \hat{N}(z,\theta) \end{bmatrix} = \sum_{j=0}^{l} \varphi_j \theta_j \tag{6.38}$$

Therefore, only $l+1$ OBPs $\{\varphi_j\}_{j=0}^{l}$ are sufficient. Instead of calculating whole Hessenberg matrix H, only $2l$ column calculation can be adequate to find l block Schur parameters resulting in $l+1$ OBPs. This significantly reduces the total estimation time.

Finally, the solution of LS problem (6.5) can be found premultiplying this equation by $(W_{\text{lsq}}\Phi)^H$ and using the equality (6.12) as

$$\theta = \Phi^H W_{\text{lsq}}^H W_{\text{lsq}} b \, . \tag{6.39}$$

6.7 Extension to MIMO systems

Model $\hat{P}(z)$ is parametrized using polynomial matrix fraction descriptions (MFD), where only right matrix fraction descriptions (RMFD) are used to simplify the notation as

$$\hat{P}(z,\theta) = \hat{N}(z,\theta)\hat{D}(z,\theta)^{-1}\ , \tag{6.40}$$

where $\hat{N}(z,\theta) \in \mathbb{R}^{n_y \times n_u}[z]$ and $\hat{D}(z,\theta) \in \mathbb{R}^{n_u \times n_u}[z]$ where n_y and n_u are the dimensions of output and input, respectively. MFDs are parametrized linearly in the parameters as (6.41)

$$\text{vec}\left(\begin{bmatrix}\hat{D}(z,\theta)\\ \hat{N}(z,\theta)\end{bmatrix}\right) = \sum_j \varphi_j \theta_j, \tag{6.41}$$

where $\varphi_j \in \mathbb{R}^{(n_y+n_u)n_u \times (n_y+n_u)n_u}[z]$ and $\theta_j \in \mathbb{R}^{(n_y+n_u)n_u \times 1}$. Then, weighted LS approximation to P_o can be obtained by minimizing the following error criterion [64, 72]

$$\arg\min_{\theta} \sum_{k=1}^{m} \|W_h \circ \left(W\left(P_o(z_k) - \hat{N}(z_k,\theta)\hat{D}(z_k,\theta)^{-1}\right)\right)\|_F^2. \tag{6.42}$$

Since (6.42) is nonlinear in $\hat{D}(z_k,\theta)$, SK iterations can be used to eliminate this nonlinearity as

$$\arg\min_{\theta} \sum_{k=1}^{m} \|W_h \circ \left(W\left(\begin{bmatrix}P & -I\end{bmatrix}\begin{bmatrix}\hat{D}(z_k,\theta)\\ \hat{N}(z_k,\theta)\end{bmatrix}\hat{D}(z_k,\theta^{\langle f-1\rangle})^{-1}\right)\right)\|_F^2. \tag{6.43}$$

- ◇ $\|A\|_F = \|\text{vec}(A)\|_2$
- ◇ $\text{vec}(ABC) = (C^T \otimes A)\text{vec}(B)$
- ◇ $\text{vec}(A \circ B) = \text{diag}(\text{vec}(A))\text{vec}(B)$

Using the facts given above from Kronecker calculus, (6.43) can be written as

$$\sum_{k=1}^{m} \|W_{\text{lsq},k}(\theta^{\langle f-1\rangle})\text{vec}\left(\begin{bmatrix}\hat{D}(z_k,\theta^{\langle f\rangle})\\ \hat{N}(z_k,\theta^{\langle f\rangle})\end{bmatrix}\right)\|_2^2\ . \tag{6.44}$$

where

$$W_{\text{lsq},k}(\theta^{\langle f-1\rangle}) = \text{diag}\left(\text{vec}(W_h)\right)\left(\hat{D}(z_k,\theta^{\langle f-1\rangle})^{-T} \otimes W(z_k)\begin{bmatrix}P_o(z_k) & -I\end{bmatrix}\right). \tag{6.45}$$

Consequently, the nonlinear least squares problem (6.42) is recast as the following iteratively solvable linear least squares problem

$$\min_{\theta^{\langle f\rangle}} \|W_{\text{lsq}}(\theta^{\langle f-1\rangle})\Phi\theta^{\langle f\rangle}\|_2^2\ , \tag{6.46}$$

where

$$W_{\text{lsq}} = \text{diag}\left(W_{\text{lsq},1},\ W_{\text{lsq},2},\ ...\right), \tag{6.47}$$

$$\Phi = [\ \varphi(z_1)^T\ \varphi(z_2)^T\ ...]^T. \tag{6.48}$$

For this case, node matrix is modified as $Z \in \mathbb{C}^{2n_y n_u m \times 2n_y n_u m}$ and weight matrix $W \in \mathbb{C}^{2n_y n_u m \times (n_y+n_u)n_u}$ as

$$Z = \text{diag}(\underbrace{z_1,\ z_1, ...,\ z_1}_{n_y n_u}, \underbrace{z_1^*,\ z_1^*, ...,\ z_1^*}_{n_y n_u}, ..., \underbrace{z_m,\ z_m, ...,\ z_m}_{n_y n_u}, \underbrace{z_m^*,\ z_m^*, ...,\ z_m^*}_{n_y n_u}), \tag{6.49}$$

$$W = [W_{\text{lsq},1}^T\ W_{\text{lsq},1}^H\ ...\ W_{\text{lsq},m}^T\ W_{\text{lsq},m}^H]^T. \tag{6.50}$$

where $W_{\text{lsq},j} \in \mathbb{C}^{n_y n_u \times (n_y+n_u)n_u}$. Real node matrix $Z_{real} \in \mathbb{C}^{2n_y n_u m \times 2n_y n_u m}$ and weight matrix $W_{real} \in \mathbb{C}^{2n_y n_u m \times (n_y+n_u)n_u}$ can be obtained as below using suitable unitary similarity transform

$$Z_{real} = \text{diag}\left(\bar{Z}_1, ..., \bar{Z}_m\right), \tag{6.51}$$

where

$$\begin{aligned} \bar{Z}_k &= \left(\begin{bmatrix} \cos\alpha_k & -\sin\alpha_k \\ \sin\alpha_k & \cos\alpha_k \end{bmatrix} \otimes I_{n_y n_u} \right) \\ &= \left[\begin{array}{c|c} \cos\alpha_k\ I_{n_y n_u} & -\sin\alpha_k\ I_{n_y n_u} \\ \hline \sin\alpha_k\ I_{n_y n_u} & \cos\alpha_k\ I_{n_y n_u} \end{array} \right]_{2n_y n_u \times 2n_y n_u}, \end{aligned} \tag{6.52}$$

$$W_{real} = \sqrt{2}\ \left[\text{Re}\{W_{\text{lsq},1}^T\}\ \text{Im}\{W_{\text{lsq},1}^T\}\ ...\ \text{Re}\{W_{\text{lsq},m}^T\}\ \text{Im}\{W_{\text{lsq},m}^T\}\right]^T. \tag{6.53}$$

First, inverse eigenvalue problem for new matrices Z_{real} and W_{real} should be solved, and corresponding $(n_y+n_u)n_u \times (n_y+n_u)n_u$-block Hessenberg matrix should be calculated. Next, using corresponding block Schur parameters, OBPs are found. Finally, LS problem can be solved using (6.39).

6.8 Extension to identification of coprime factors for MIMO systems

Model $\hat{P}(z)$ is parametrized using RMFD as

$$\hat{P}(z,\theta) = B(z,\theta)A(z,\theta)^{-1}, \tag{6.54}$$

where $B(z,\theta) \in \mathbb{R}^{n_y \times n_u}[z]$ and $A(z,\theta) \in \mathbb{R}^{n_u \times n_u}[z]$. In addition, $\{\hat{N}(z,\theta), \hat{D}(z,\theta)\}$ and $\{B(z,\theta), A(z,\theta)\}$ are related as

$$\begin{bmatrix} \hat{N}(\theta) \\ \hat{D}(\theta) \end{bmatrix} = \begin{bmatrix} B(\theta) \\ A(\theta) \end{bmatrix} (\tilde{D}_e A(\theta) + \tilde{N}_{e,2} V_2^{-1} B(\theta))^{-1} . \tag{6.55}$$

MFDs are parametrized linearly in the parameters as

$$\text{vec}\left(\begin{bmatrix} B(z,\theta) \\ A(z,\theta) \end{bmatrix} \right) = \sum_j \varphi_j \theta_j , \tag{6.56}$$

where $\varphi_j \in \mathbb{R}^{(n_y+n_u)n_u \times (n_y+n_u)n_u}[z]$ and $\theta_j \in \mathbb{R}^{(n_y+n_u)n_u \times 1}$. Then, the following $\mathcal{H}_\infty$-norm based weighted error criterion for $\{N_o, D_o\}$ estimate is used [55]

$$\min_{\hat{N},\hat{D}} \|W \left(\begin{bmatrix} N_o \\ D_o \end{bmatrix} - \begin{bmatrix} \hat{N} \\ \hat{D} \end{bmatrix} \right) \tilde{N}_e\|_\infty . \tag{6.57}$$

$$\text{subject to } \hat{N}, \hat{D} \in \mathcal{RH}_\infty$$

As discussed in Chapter 5, this problem can be approximately solved by using Lawson's algorithm and Sanathanan-Koerner iterations as

$$\sum_i \|W_{\text{lsq},i}^{\langle k \rangle}(\theta^{\langle f-1 \rangle}) \text{vec}\left(\begin{bmatrix} B(\theta^{\langle f \rangle}) \\ A(\theta^{\langle f \rangle}) \end{bmatrix} \right) \|_2^2 . \tag{6.58}$$

Consequently, the following iteratively solvable linear LS problem is achieved

$$\min_{\theta^{\langle f \rangle}} \|W_{\text{lsq}}^{\langle k \rangle}(\theta^{\langle f-1 \rangle}) \Phi \theta^{\langle f \rangle}\|_2^2 \tag{6.59}$$

where

$$\begin{aligned} W_{\text{lsq},i}^{\langle k \rangle}(\theta^{\langle f-1 \rangle}) = \text{diag}\left(\text{vec}(W_h^{\langle k \rangle})\right) \Bigg(& \left[(\tilde{D}_e A(\theta^{\langle f-1 \rangle}) + \tilde{N}_{e,2} V_2^{-1} B(\theta^{\langle f-1 \rangle}))^{-1} \right]^T \\ & \otimes \left[W \left(\begin{bmatrix} N_o \tilde{N}_{e,2} V_2^{-1} & N_o \tilde{D}_e \\ D_o \tilde{N}_{e,2} V_2^{-1} & D_o \tilde{D}_e \end{bmatrix} - I \right) \right] \Bigg), \end{aligned} \tag{6.60}$$

$$W_{\text{lsq}}^{\langle k \rangle} = \text{diag}\left(W_{\text{lsq},1}^{\langle k \rangle}, \ W_{\text{lsq},2}^{\langle k \rangle}, \ \ldots \right) , \tag{6.61}$$

$$\Phi = [\ \varphi(z_1)^T \ \varphi(z_2)^T \ \ldots]^T. \tag{6.62}$$

For this case, node matrix is modified as $Z \in \mathbb{C}^{2(n_y+n_u)n_u m \times 2(n_y+n_u)n_u m}$ and weight matrix $W \in \mathbb{C}^{2(n_y+n_u)n_u m \times (n_y+n_u)n_u}$ as

$$Z = \text{diag}(\underbrace{z_1,\ z_1, ...,\ z_1}_{(n_y+n_u)n_u}, \underbrace{z_1^*,\ z_1^*, ...,\ z_1^*}_{(n_y+n_u)n_u}, ..., \underbrace{z_m,\ z_m, ...,\ z_m}_{(n_y+n_u)n_u}, \underbrace{z_m^*,\ z_m^*, ...,\ z_m^*}_{(n_y+n_u)n_u}), \quad (6.63)$$

$$W = [W_{\text{lsq},1}^T\ W_{\text{lsq},1}^H\ ...\ W_{\text{lsq},m}^T\ W_{\text{lsq},m}^H]^T. \quad (6.64)$$

where $W_{\text{lsq},j} \in \mathbb{C}^{(n_y+n_u)n_u \times (n_y+n_u)n_u}$. Real node matrix $Z_{real} \in \mathbb{C}^{2(n_y+n_u)n_u m \times 2(n_y+n_u)n_u m}$ and weight matrix $W_{real} \in \mathbb{C}^{2(n_y+n_u)n_u m \times (n_y+n_u)n_u}$ can be obtained as below using suitable unitary similarity transform

$$Z_{real} = \text{diag}\left(\bar{Z}_1, ..., \bar{Z}_m\right), \quad (6.65)$$

where

$$\bar{Z}_k = \left(\begin{bmatrix} \cos\alpha_k & -\sin\alpha_k \\ \sin\alpha_k & \cos\alpha_k \end{bmatrix} \otimes I_{(n_y+n_u)n_u} \right) \quad (6.66)$$

$$= \left[\begin{array}{c|c} \cos\alpha_k\ I_{(n_y+n_u)n_u} & -\sin\alpha_k\ I_{(n_y+n_u)n_u} \\ \hline \sin\alpha_k\ I_{(n_y+n_u)n_u} & \cos\alpha_k\ I_{(n_y+n_u)n_u} \end{array} \right]_{2(n_y+n_u)n_u \times 2(n_y+n_u)n_u},$$

$$W_{real} = \sqrt{2}\ \left[\text{Re}\{W_{\text{lsq},1}^T\}\ \text{Im}\{W_{\text{lsq},1}^T\}\ ...\ \text{Re}\{W_{\text{lsq},m}^T\}\ \text{Im}\{W_{\text{lsq},m}^T\}\right]^T. \quad (6.67)$$

First, inverse eigenvalue problem for new matrices Z_{real} and W_{real} should be solved, and corresponding $(n_y+n_u)n_u \times (n_y+n_u)n_u$-block Hessenberg matrix should be calculated. Next, using corresponding block Schur parameters, OBPs are found. Finally, LS problem can be solved using (6.39).

6.9 Gaus-Newton algorithm

The error criterion given in (6.43) can be written as

$$\arg\min_{\theta} \sum_{k=1}^{m} \left[\epsilon(z_k,\theta)^* \epsilon(z_k,\theta)\right], \quad (6.68)$$

where

$$\epsilon(z_k,\theta) = W_{\text{GN},k}(\theta^{\langle i \rangle}) \text{vec}\left(\begin{bmatrix} \hat{D}(z_k,\theta^{\langle i \rangle}) \\ \hat{N}(z_k,\theta^{\langle i \rangle}) \end{bmatrix} \right), \quad (6.69)$$

$$W_{\mathrm{GN},k}(\theta^{\langle i\rangle}) = \mathrm{diag}\left(\mathrm{vec}(W_h)\right)\left(\hat{D}(z_k,\theta^{\langle i\rangle})^{-T} \otimes W(z_k)\begin{bmatrix} P_o(z_k) & -I \end{bmatrix}\right). \quad (6.70)$$

Similar formulation can also be used for coprime factors $\{B(z,\theta), A(z,\theta)\}$ identification problem in (5.30).

Given an initial estimate $\theta^{\langle 0\rangle}$, Gaus-Newton algorithm finds a new estimate for $i = 1, 2, \ldots$ by solving [70, 73]

$$\theta^{\langle i+1\rangle} = \theta^{\langle i\rangle} + \arg\min_{\Delta\theta} \sum_{k=1}^{m} \| J(z_k,\theta^{\langle i\rangle})\Delta\theta + \epsilon(z_k,\theta^{\langle i\rangle})\|_2^2 \,, \quad (6.71)$$

where

$$J(z_k,\theta^{\langle i\rangle}) = \left.\frac{\partial\epsilon(z_k,\theta)}{\partial\theta}\right|_{\theta^{\langle i\rangle}}. \quad (6.72)$$

If the parametrization of $[\hat{N}^T(\theta)\ \hat{D}^T(\theta)]^T$ uses data dependent orthonormal polynomials in SK iterations, subsequent Gaus-Newton iterations also remain close to optimal for the nonlinear least squares problem. Therefore, accurate parametric coprime factors can be obtained in this way.

CHAPTER 7

MODEL VALIDATION

Robust control design requires a nominal model together with $\mathcal{H}_\infty$-norm based perturbation to determine robustness of the feedback system. In this respect, model validation method in frequency domain is introduced in [74], and it aims to find whether an uncertain model is consistent with measured outputs from true system. In addition, representing disturbance as an additive signal to system output is common method, and both additive disturbance and perturbation are considered as deterministic sets. This problem is called deterministic model validation problem, and it aims to find the minimum norm perturbation and disturbance such that the measured data and the uncertain model are consistent [31, 75]. Allocating larger portions of residuals to disturbance may result in poor performance and instability; whereas, allocating larger portions to perturbation may result in overly conservative design. Therefore, the nominal model residuals should be partitioned correctly between perturbation and disturbance terms to address this ill-posedness of model validation problem. Moreover, the disturbance terms should be related with parts of the residuals which are uncorrelated with the input. Consequently, stochastic disturbance model is more suitable to enforce independence of disturbance. Therefore, the method introduced in [31, 76] suggests an estimator for a non-parametric stochastic disturbance model, and its deterministic approximation. Then, model validation problem is solved by using the generalization of structured singular value for implicit LFTs as defined in [77, 78]. The problem is briefly introduced by following similar strategy followed in [31, 76].

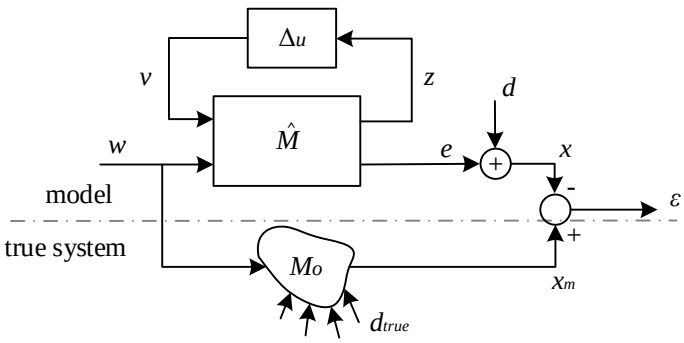

Figure 7.1: Model validation framework

7.1 Problem formulation

The model validation problem is considered in the framework depicted in Figure 7.1, where $M_o \in \mathcal{RH}_\infty^{n_x \times n_w}$, x_m, d_{true} and w denote the actual system, measured output, disturbance term and manipulated input respectively. Consequently, the true system is governed by

$$x_m = M_o w + d_{\text{true}} \ . \tag{7.1}$$

Let $\hat{M} \in \mathcal{RH}_\infty^{(n_z+n_x)\times(n_v+n_w)}$ be the interconnection structure including the controller, nominal model, uncertainty structure and weighting functions, and x and d denote the uncertain model output and disturbance model. Then, the uncertain model is defined as

$$x = \mathcal{F}_u(\hat{M}, \Delta_u) w + d \ , \tag{7.2}$$

where the $\mathcal{H}_\infty$-norm bounded perturbation block $\mathbf{\Delta_u}$ is specified as in [79].

$$\begin{aligned} \mathbf{\Delta_u^c} = \{&\text{diag}(\delta_1 I_{r_1}, ..., \delta_s I_{r_s}, \Delta_{S+1}, ..., \Delta_{S+F}) : \delta_i \in \mathbb{C}, \\ &\Delta_{S+j} \in \mathbb{C}^{n_{v_j} \times n_{z_j}}, 1 \leqslant i \leqslant S, 1 \leqslant j \leqslant F\} \end{aligned} \tag{7.3}$$

$$\mathbf{\Delta_u} = \{\Delta_u \in \mathbf{\Delta_u^c} : \bar{\sigma}(\Delta_u) \leqslant \gamma\} \tag{7.4}$$

Let the measured signals w and x_m have discrete Fourier transforms (DFT) $W(w_i)$ and $X_m(w_i)$ on a DFT grid $w_i \in \Omega$ as defined by (7.5), and Ω^{val} is the part of Ω where $W(w_i) \neq 0$.

$$W_N(w_i) = \frac{1}{\sqrt{N}} \sum_{t=1}^{N} w(t) e^{j w_i t} \tag{7.5}$$

Then, the uncertain model residual is equal to

$$E(w_i) = X_m(w_i) - X(w_i) \ , \tag{7.6}$$

where $X(w_i)$ is the DFT of $x(t)$. Moreover, let $D(w_i)$ denote the DFT of $d(t)$, and let it belong to certain set $\mathbf{D}(w_i)$ as discussed in the next section. Then, model validation problem requires two problem definition from [31, 76].

Frequency domain model validation decision problem (FDMVDP): It is assumed that the uncertain model (7.2), norm bound $\gamma(w_i) = \bar{\sigma}(\Delta_u(w_i))$, measurements $W(w_i)$ and $X_m(w_i)$ on $w_i \in \Omega^{\text{val}}$ and disturbance $D(w_i) \in \mathbf{D}(w_i)$ are known. Then, FDMVDP determines whether the uncertain model reproduces the measured signal at frequency w_i, namely $E(w_i) = 0$.

Frequency domain model validation optimization problem (FDMVOP): It is assumed that the uncertain model (7.2), measurements $W(w_i)$ and $X_m(w_i)$ on $w_i \in \Omega^{\text{val}}$ and disturbance $D(w_i) \in \mathbf{D}(w_i)$ are known. Then, FDMVOP aims to find minimum $\gamma(w_i)$ such that $E(w_i) = 0$. The model validation problem makes sense if the following three assumptions hold. While well-posedness of $\mathcal{F}_u(\hat{M}, \Delta_u)$ requires assumption 7.1, observability of the uncertainty from the output requires assumption 7.2. Finally, nontrivial model validation problem is assured by assumption 7.3 indicating nonzero nominal model error [31].

Assumption 7.1. $\det(I - \hat{M}_{11}\Delta_u) \neq 0 \ \ \forall \Delta_u \in \mathbf{\Delta_u}, \ \|\Delta_u\|_\infty < \gamma$

Assumption 7.2. $E^{\text{nom}} = (X_m - \hat{M}_{22}W) \in \text{Im}\left(\hat{M}_{21}\Delta_u(I - \hat{M}_{11}\Delta_u)^{-1}\hat{M}_{12}\right)$

Assumption 7.3. $E^{\text{nom}} = (X_m - \hat{M}_{22}W) \neq 0$

7.2 Disturbance model

In this section disturbance model $\mathbf{D}(w_i)$ is discussed in detail. The main idea is to use a stochastic model for accurate representation of a disturbance in physical system. Therefore, the estimator proposed in [31] to determine nonparametric stochastic disturbance model is reviewed. Then, this model is modified for approximate deterministic model which is essential for model validation purposes. Following properties of filtered white noise after a DFT are essential [31, 80].

Lemma 7.4. Let $d_s = H_o t$ where t is a sequence of independent, identically distributed (IID) random variables with zero mean, unit variance, and bounded moments of all orders, and $H_o \in \mathcal{RH}_\infty$.

Theorem 7.5. If the above lemma holds, then the $D_{S,N}(w_i)$, DFT of d_s , is asymptotically ($N \to \infty$) independent, circular complex normally distributed. It is shown as $\mathcal{N}_c(0, C_{d_s}(w_i))$ for $w_i \neq k\pi,\ k \in \mathbb{Z}$ and independence states that $D_{S,N}(w_i)$ and $D_{S,N}(w_j)$ are asymptotically independent for $i \neq j,\ w_i, w_j \in [0, \pi]$.

Constant probability lines correspond to circles in the complex plane for $\mathcal{N}_c$ distribution since real and imaginary part of circular complex normal distribution are independent. This essentially leads to the following proposition in [31].

Proposition 7.6. Let $D_{S,N}(w_i) \in \mathcal{N}_c(0, C_{d_s}(w_i))$, then

$$\mathcal{P}\Big(|D_{S,N}(w_i)| < \sqrt{\frac{1}{2}C_{d_s}(w_i)c_x}\Big) = \alpha \tag{7.7}$$

where c_x is the α-probability level of the $\chi^2(2)$ distribution.

Proposition 7.6 is essential for converting stochastic disturbance model to deterministic one. Now let

$$\bar{\tilde{D}}_{S,N}(w_i) = \sqrt{\frac{1}{2}C_{d_s}(w_i)c_x} \tag{7.8}$$

Then, with probability α, the following equation is satisfied,

$$D_{S,N}(w_i) \in \delta_d \bar{\tilde{D}}_{S,N}(w_i),\ \text{for } |\delta_d| < 1 \tag{7.9}$$

where $\delta_d \bar{\tilde{D}}_{S,N}(w_i)$ corresponds to approximate deterministic disturbance model. It is frequency dependent which gives nonparametric disturbance model for all $w_i \in \Omega^{\text{val}}$. Note that lemma 7.4 and theorem 7.5 are given for random variables, i.e., for scalar case. For multivariable case, circularity property for random vectors requires that elements of $D_{S,N}(w_i)$ must be uncorrelated. This is achieved by introducing coordinate transform $T_D^*(w_i)$ where $C_{d_s}(w_i) = T_D(w_i)\Sigma_{S,N}T_D^*(w_i)$ is the eigenvalue decomposition for each w_i [76]. After the transformation (7.10) is applied,

$$\tilde{D}_{S,N}(w_i) = T_D^*(w_i)D_{S,N}(w_i) \tag{7.10}$$

desired independent identical distribution is found as

$$\tilde{D}_{S,N}(w_i) \in \mathcal{N}_c(0, \Sigma_{S,N}(w_i))\ , \tag{7.11}$$

where $\Sigma_{S,N} = \text{diag}(\lambda_1, ..., \lambda_{n_d})$. Then, the diagonal matrix $\bar{\tilde{D}}(w_i)$ with the qth entry as (7.12), and block structure (7.13) are introduced.

$$\bar{\tilde{D}}_q(w_i) = \sqrt{\frac{1}{2}\lambda_q(w_i)c_x} \tag{7.12}$$

$$\mathbf{\Delta_d} = \{\text{diag}(\delta_1, ..., \delta_{n_d}) \mid \delta_q \in \mathbb{C}, 1 \leqslant q \leqslant n_d\} \tag{7.13}$$

Finally, $\mathbf{D}(w_i)\mathbf{1}$ corresponds to the $\mathcal{L}_\infty$ norm-bounded disturbance model where $\mathbf{1}$ denotes all-ones column vector and

$$\mathbf{D}(w_i) = \left\{T_D(w_i)\bar{\tilde{D}}(w_i)\Delta_d \mid \Delta_d \in \mathcal{B}\mathbf{\Delta_d}\right\}. \tag{7.14}$$

7.2.1 Estimating nonparametric disturbance models

The nonparametric disturbance model on a frequency grid $w_i \in \Omega^{\text{val}}$ requires $C_{d_s}(w_i)$. The properties of d_s can be estimated efficiently if a periodic input signal w with period time N is used, and this periodic signal is applied n_{exp} times.

$$x_m = M_o w + d_s \tag{7.15}$$

Under these conditions, the following estimator is suggested in [76].

$$\hat{C}_{d_s}(w_i) = \frac{1}{n_{\text{exp}} - 1} \sum_{r=1}^{n_{\text{exp}}} \left((X_{m,r}(w_i) - \hat{m}_{X_{m,r}}(w_i)) \, (X_{m,r}(w_i) - \hat{m}_{X_{m,r}}(w_i))^* \right). \tag{7.16}$$

$$\hat{m}_{X_{m,r}}(w_i) = \frac{1}{n_{\text{exp}}} \sum_{r=1}^{n_{\text{exp}}} X_{m,r}(w_i). \tag{7.17}$$

These estimates asymptotically ($n_{\text{exp}} \to \infty$) converge to true values C_{d_s} and $m_{X_{m,r}}$.

7.3 Averaging in a deterministic framework

As stated previously, disturbance is attributed to parts of model residuals that are uncorrelated with the input. The stochastic disturbance assumptions that gives (7.14) state that d can not include periodic components. In addition, this property is preserved when the stochastic model is converted into deterministic model. Therefore,

periodic input w can be used to discriminate the effects of w from d [31].
In the frequency domain, uncertain model residuals can be given by

$$E(w_i) = X_m(w_i) - \Big(\mathcal{F}_u(\hat{M}, \Delta_u)W(w_i) + D(w_i)\mathbf{1}\Big), \quad D(w_i) \in \mathbf{D}(w_i). \tag{7.18}$$

Main problem is to determine the minimum uncertainty bound γ which makes $E(w_i) = 0 \ \forall w_i \in \Omega^{\text{val}}$. Nominal model error can be obtained as below for each $\forall w_i$.

$$E^{\text{nom}} = \hat{M}_{21}\Delta_u(I - \hat{M}_{11}\Delta_u)^{-1}\hat{M}_{12}W - T_D\bar{\tilde{D}}\Delta_d\mathbf{1}. \tag{7.19}$$

This equation clearly shows that nominal model residuals should be partitioned between perturbation and disturbance correctly. If too large disturbance model is selected, resulting model perturbation becomes too optimistic. Therefore, reducing this optimism in uncertainty estimation is essential. E^{nom} depends on both size and direction of W. In the constant direction of W, normalization (7.20) is helpful to analyze the error for different inputs [31, 68].

$$\bar{E}^{\text{nom}} = \frac{E^{\text{nom}}}{\|W\|_2} = \frac{\hat{M}_{21}\Delta_u(I - \hat{M}_{11}\Delta_u)^{-1}\hat{M}_{12}W}{\|W\|_2} - \frac{T_D\bar{\tilde{D}}\Delta_d\mathbf{1}}{\|W\|_2}. \tag{7.20}$$

Then, by increasing the input amplitude by a factor of a, the following result is obtained.

$$\bar{E}^{\text{nom}} = \frac{\hat{M}_{21}\Delta_u(I - \hat{M}_{11}\Delta_u)^{-1}\hat{M}_{12}\, aW}{\|aW\|_2} - \frac{T_D\bar{\tilde{D}}\Delta_d\mathbf{1}}{\|aW\|_2} \tag{7.21}$$

$$= \frac{\hat{M}_{21}\Delta_u(I - \hat{M}_{11}\Delta_u)^{-1}\hat{M}_{12}W}{\|W\|_2} - \frac{T_D\bar{\tilde{D}}\Delta_d\mathbf{1}}{a\|W\|_2}. \tag{7.22}$$

(7.22) implies that when W is increased by $a > 1$, normalized nominal model residual that is attributed to disturbance decays; however, the part related to uncertainty remains constant. Consequently, less optimistic perturbation model can be obtained.
Multiplying input signal in the time domain and averaging over multiple periods have similar results in the frequency domain. If n_{per} period signal with period N is applied, DFTs of these signals satisfy

$$W_{n_{\text{per}}N}(w_i) = \frac{1}{\sqrt{n_{\text{per}}N}}\sum_{t=1}^{n_{\text{per}}N} w(t)e^{jw_it} = \sqrt{n_{\text{per}}}\, W_N(w_i) \tag{7.23}$$

for $w_i \in \{2\pi p/N, p = 0, 1, ..., N-1\}$ [68, 81]. Therefore, using periodic signal w and increasing number of period n_{per}, the disturbance term effectively averages out with a factor $a = \sqrt{n_{\text{per}}}$, and optimism in the estimation is reduced.

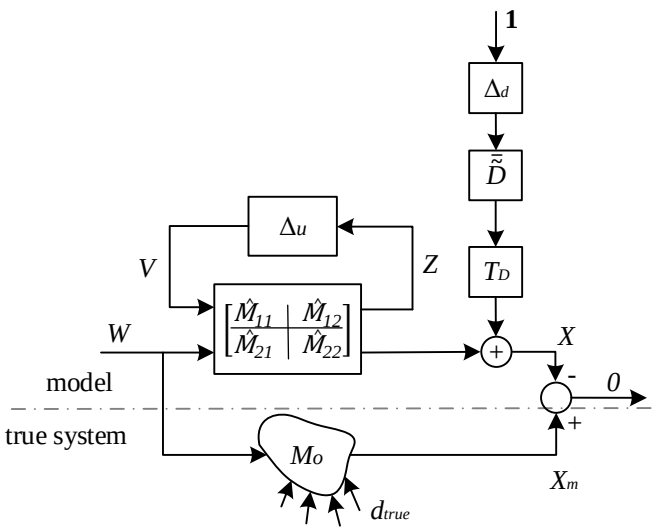

Figure 7.2: Consistency in the FDMVDP

7.4 Solution of model validation problem

FDMVDP is related to whether model is consistent with the measured data, that is $E = 0\ \forall w_i \in \Omega^{\text{val}}$ as given by (7.24), and as illustrated in Figure 7.2.

$$0 = X_m - \mathcal{F}_u(\hat{M}, \Delta_u)W - T_D\bar{\tilde{D}}\Delta_d\mathbf{1} \tag{7.24}$$

By introducing fictitious scalar input 1, implicit LFT given by (7.25) and shown in Figure 7.3 is obtained

$$0 = \mathcal{F}_u(\bar{M}, \bar{\Delta})\beta\ , \tag{7.25}$$

where $\beta \in \mathbb{C} \setminus 0$ is the nontrivial signal, and $\bar{M}$ and $\bar{\Delta}$ are rearranged as [68, 81]

$$\bar{M} = \left[\begin{array}{cc|c} 0 & 0 & \mathbf{1} \\ 0 & \gamma\hat{M}_{11} & -\hat{M}_{12}W \\ \hline -T_D\bar{\tilde{D}} & \gamma\hat{M}_{21} & X_m - \hat{M}_{22}W \end{array}\right]\ , \tag{7.26}$$

$$\bar{\Delta} \in \mathcal{B}\bar{\mathbf{\Delta}}, \bar{\mathbf{\Delta}} = \left\{ \begin{bmatrix} \Delta_d & 0 \\ 0 & \Delta_u \end{bmatrix} \mid \Delta_d \in \mathbf{\Delta_d},\ \Delta_u \in \mathbf{\Delta_u} \right\}. \tag{7.27}$$

After inserting γ in $\bar{M}$ as given in (7.26), the consistency equation (7.25), which is the requirement for FDMVDP, becomes directly related to structured singular value.

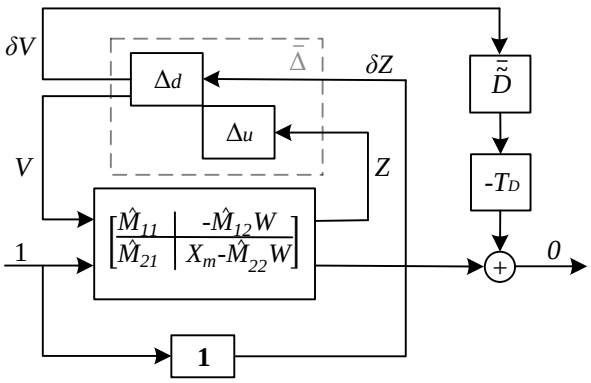

Figure 7.3: Implicit LFT

Definition 7.7. The structured singular value of implicit system is defined as

$$\bar{\mu}_{\bar{\Delta}}(M,N) = 0 \text{ If Ker} \left(\begin{bmatrix} I - \bar{\Delta}M \\ N \end{bmatrix} \right) = 0 \ \forall \bar{\Delta} \in \bar{\mathbf{\Delta}}, \text{ otherwise} \tag{7.28}$$

$$\bar{\mu}_{\bar{\Delta}}(M,N) = \left(\min_{\bar{\Delta}} \{ \bar{\sigma}(\bar{\Delta}) \mid \bar{\Delta} \in \bar{\mathbf{\Delta}}, \text{Ker} \left(\begin{bmatrix} I - \bar{\Delta}M \\ N \end{bmatrix} \right) \neq 0 \} \right)^{-1}.$$

Proposition 7.8. In the FDMVDP, the model is not invalidated if and only if $\bar{\mu}_{\bar{\Delta}}(\bar{M}_{11} - \bar{M}_{12}\bar{X}_{22}\bar{M}_{21}, \bar{M}_{21} - \bar{M}_{22}\bar{X}_{22}\bar{M}_{21}) > 1$ where $\bar{X}_{22}\bar{M}_{22} = I$ [77, 76]. If $N = 0$ is satisfied, the condition reduces to standard structured singular value problem $\mu_{\bar{\Delta}}$, and corresponding test reduces to $\mu_{\bar{\Delta}}(\bar{M}_{11} - \bar{M}_{12}\bar{X}_{22}\bar{M}_{21}) > 1$ [78, 82]. Therefore, FDMVOP is solved by bisection algorithm and testing this proposition each time for a new $\gamma(w_i)$.

Algorithm 7.9. Similar to μ case, bounds of $\bar{\mu}_{\bar{\Delta}}(M,N)$ are used instead of exact value calculation. Herein, testing upper bound $\bar{\mu}^u_{\bar{\Delta}}(M,N) \leq 1$ is a sufficient but not necessary condition for model invalidation. In addition, $\bar{\mu}^u_{\bar{\Delta}}(M,N) > 1$ leads to optimistic results for model validation [31].

CHAPTER 8

VISUALIZATION OF UNCERTAIN MODELS

In this section, construction of Bode magnitude diagrams for multivariable uncertain systems is explained by following the method suggested in [83]. First, for a single frequency, the complex valued matrix problem is defined. Next, Bode magnitude diagrams are constructed by solving these problems for required frequency grid.

8.1 A review of μ

For this and the following chapters, structural singular value definition [79], and its extensions [75, 84] are required. The feedback connection in Figure 8.1 is defined by equations $z = Mv$ and $v = \Delta_u z$ with M and $\Delta_u \in \mathbf{\Delta_u}$ are complex valued matrices with suitable sizes. In addition, $\mathbf{\Delta_u}$ has block diagonal structure on Δ_u as (8.1)

$$\mathbf{\Delta_u} = \{\text{diag}\ (...\Delta_i...) \mid i \in I\} \tag{8.1}$$

where I corresponds to index set $(1, ..., n)$ for n perturbation blocks [75].

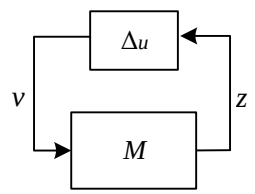

Figure 8.1: Uncertain system

8.1.1 Structured singular value

Definition 8.1. Let M and $\Delta_u \in \mathbf{\Delta_u}$ be given with suitable sizes. Then,

$$\mu_{\mathbf{\Delta_u}}(M) = \left(\min\{\bar{\sigma}(\Delta_u) \mid \Delta_u \in \mathbf{\Delta_u},\ \det(I - M\Delta_u) = 0\}\right)^{-1}, \tag{8.2}$$

If $\det(I - M\Delta_u) \neq 0,\ \forall \Delta_u \in \mathbf{\Delta_u},$ define $\mu_{\mathbf{\Delta_u}}(M) = 0.$

Definition given below can also be used equivalently for $\mu_{\mathbf{\Delta_u}}(M)$,

$$\mu_{\mathbf{\Delta_u}}(M) = \max_{\|v\|_2=1} \{\gamma \ \mid \ \|v_i\|_2\, \gamma \leq \|z_i\|_2, \forall i \in I\} \tag{8.3}$$

where $v_i = \Delta_i\, z_i,\ \forall i \in I$ [75].

8.1.2 Generalized structured singular value

The μ framework considers perturbation block Δ_u, satisfying a maximum norm constraint. Second class of perturbations is defined to satisfy minimum gain constraint [75]. Let block structure $\mathbf{\Delta_u}$ be partitioned as

$$\mathbf{\Delta_u} = \begin{bmatrix} \mathbf{\Delta_J} & 0 \\ 0 & \mathbf{\Delta_K} \end{bmatrix}, \tag{8.4}$$

where

$$\mathbf{\Delta_J} = \{\text{diag}\ (...\Delta_j...) \mid j \in J\} \tag{8.5}$$

$$\mathbf{\Delta_K} = \{\text{diag}\ (...\Delta_k...) \mid k \in K\} \tag{8.6}$$

and index set I is partitioned as $I = (J, K)$. Similarly, matrix M is also partitioned according to $\mathbf{\Delta_u}$ as

$$M = \begin{bmatrix} M_{JJ} & M_{JK} \\ M_{KJ} & M_{KK} \end{bmatrix}. \tag{8.7}$$

Definition 8.2. Let M and $\Delta_u \in \mathbf{\Delta_u}$ be partitioned suitably as (8.7) and (8.4), respectively. Then, $\mu_{g,\mathbf{\Delta_u}}$ is defined as [75]

$$\mu_{g,\mathbf{\Delta_u}} = \max_{\|v\|_2=1} \left\{ \gamma \ \middle| \ \begin{array}{c} \|v_j\|_2\, \gamma \leq \|z_j\|_2,\ \forall j \in J \\ \|z_k\|_2\, \gamma \leq \|v_k\|_2,\ \forall k \in K \end{array} \right\}. \tag{8.8}$$

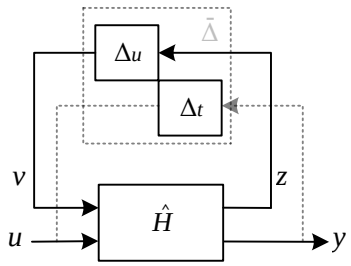

Figure 8.2: Uncertain open loop system

Generalized structured singular value becomes more valuable if it is used with a new extended already partitioned uncertainty set $\bar{\mathbf{\Delta}}$ which is defined as

$$\bar{\mathbf{\Delta}} = \left\{ \begin{bmatrix} \Delta_u & 0 \\ 0 & \Delta_t \end{bmatrix} \mid \Delta_u \in \mathbf{\Delta_u},\ \Delta_t \in \mathbf{\Delta_t} \right\} , \tag{8.9}$$

where $\mathbf{\Delta_t} = \{\Delta_t \mid \Delta_t \in \mathbb{C}^{n_u \times n_y}\}$ [83].

Consequently, using μ_g definition (8.8) for the interconnection structure shown in Figure 8.2, where the uncertainty block $\bar{\mathbf{\Delta}}$ is defined in (8.9) and $\hat{H}$ is full column rank, gives

$$\mu_{g,\bar{\mathbf{\Delta}}} = \max_{\left\| \begin{bmatrix} v \\ u \end{bmatrix} \right\|_2 = 1} \left\{ \gamma \;\middle|\; \begin{array}{c} \|v_i\|_2\, \gamma \leq \|z_i\|_2,\ \forall i \in I \\ \|y\|_2\, \gamma \leq \|u\|_2 \end{array} \right\} . \tag{8.10}$$

This definition is later modified to generate Bode magnitude diagrams in the next section.

8.1.3 Skewed structured singular value

Definition 8.3. For a complex matrix H and $\bar{\Delta} \in \bar{\mathbf{\Delta}}$, $\mu_{s,\bar{\mathbf{\Delta}}}$ is defined as [83, 84]

$$\mu_{s,\bar{\mathbf{\Delta}}} = \left(\min\{\bar{\sigma}(\Delta_t) \mid \Delta_t \in \mathbf{\Delta_t},\ \Delta_u \in \mathbf{\Delta_u},\ \bar{\sigma}(\Delta_u) \leq 1, \det(I - M\bar{\Delta}) = 0\}\right)^{-1} . \tag{8.11}$$

Skewed structured singular value is more suitable when some partitions of the uncertainty block are already known. In other words, the minimization is performed over the unknown portions instead of over whole block as in the standard structured singular value case (8.2).

8.2 Upper and lower bounds for MIMO systems

In this section, Bode magnitude bounds are obtained for both multivariable singular values and elementwise maximum and minimum gain. Second approach requires ij^{th} element of $\mathcal{P}$ which is obtained as,

$$\mathcal{P}_{ij} = \{P_{ij} \mid P_{ij} \in u_i \mathcal{P}_{ij} u_j^T \tag{8.12}$$

where u_k^T denotes a zero vector except its kth element which equals to 1.

8.2.1 Lower bound

Lower bound on the singular values of an uncertain model can be obtained from following theorem [83].

Theorem 8.4. Let the uncertain model set is represented with Figure 8.2 with $\Delta_u \in \mathcal{B}\mathbf{\Delta_u}$ and full column rank $\hat{H}_{22}$. Then, the minimum gain of the uncertain model set $\mathcal{P}$ is larger than α, $\min_{P\in\mathcal{P}} \underline{\sigma}(P) \geq \alpha$, iff

$$\mu_{g,\bar{\mathbf{\Delta}}} \left(\begin{bmatrix} \hat{H}_{11} & \hat{H}_{12} \\ \frac{1}{\alpha}\hat{H}_{21} & \frac{1}{\alpha}\hat{H}_{22} \end{bmatrix} \right) \geq 1. \tag{8.13}$$

If $\hat{H}_{22}$ is not full column rank, define $\min_{P\in\mathcal{P}} \underline{\sigma}(P) = 0$.

Similarly, following corollary gives a lower bound on elementwise singular values of the uncertain model set [83].

Corollary 8.5. Let the uncertain model set is represented with Figure 8.2 with $\Delta_u \in \mathcal{B}\mathbf{\Delta_u}$ and full column rank $u_i\hat{H}_{22}u_j^T$. Then, the minimum gain of the SISO uncertain model set P_{ij} is larger than α, $\min_{P_{ij}\in\mathcal{P}_{ij}} \underline{\sigma}(P_{ij}) \geq \alpha$, iff

$$\mu_{g,\bar{\mathbf{\Delta}}} \left(\begin{bmatrix} \hat{H}_{11} & \hat{H}_{12}u_j^T \\ \frac{1}{\alpha}u_i\hat{H}_{21} & \frac{1}{\alpha}u_i\hat{H}_{22}u_j^T \end{bmatrix} \right) \geq 1. \tag{8.14}$$

If $u_i\hat{H}_{22}u_j^T = 0$, define $\min_{P_{ij}\in\mathcal{P}_{ij}} \underline{\sigma}(P_{ij}) = 0$.

Using the theorem 8.4 and corollary 8.5 and applying bisection over α, the minimum gain of the uncertain model can be obtained. The results use skewed and generalized

structured singular value simultaneously. As stated in [75], the $\mu_{g,\bar{\mathbf{\Delta}}}$ problem can be recast as a μ problem for square multivariable case where $n_u = n_y$. This formulation is applicable to both multivariable and elementwise SISO uncertain model case in this thesis. Therefore, the following theorem gives the equivalent μ problem [75].

Theorem 8.6. Consider the structure in Figure 8.1, $\mathbf{\Delta_u}$ satisfies (8.4) and M satisfies (8.7). If M_{KK} is square and μ_g maximization problem is well-defined; then

$$\mu_{g,\mathbf{\Delta_u}}(M) = \mu_{\tilde{\mathbf{\Delta}}}(\tilde{M}) \tag{8.15}$$

where

$$\tilde{M} = \begin{bmatrix} M_{JJ} - M_{JK}M_{KK}^{-1}M_{KJ} & M_{JK}M_{KK}^{-1} \\ -M_{KK}^{-1}M_{KJ} & M_{KK}^{-1} \end{bmatrix} \tag{8.16}$$

and corresponding uncertainty structure for the μ problem is

$$\tilde{\mathbf{\Delta}} = \begin{bmatrix} \mathbf{\Delta_J} & 0 \\ 0 & \mathbf{\Delta_K^T} \end{bmatrix}. \tag{8.17}$$

8.2.2 Upper bound

Upper bound on the singular values of an uncertain model set can be obtained by using the standard structured singular value μ [83].

Theorem 8.7. Let the uncertain model set is represented with Figure 8.2 with $\Delta_u \in \mathcal{B}\mathbf{\Delta_u}$. Then, the maximum gain of the uncertain model set $\mathcal{P}$ is smaller than β, $\max_{P\in\mathcal{P}} \bar{\sigma}(P) < \beta$, iff

$$\mu_{\bar{\mathbf{\Delta}}}\left(\begin{bmatrix} \hat{H}_{11} & \hat{H}_{12} \\ \frac{1}{\beta}\hat{H}_{21} & \frac{1}{\beta}\hat{H}_{22} \end{bmatrix}\right) < 1. \tag{8.18}$$

If $\mu(\hat{H}_{11}) \geq 1$, define $\max_{P\in\mathcal{P}} \bar{\sigma}(P) = \infty$.

Similarly, following corollary gives an upper bound on elementwise singular values of uncertain model set [83].

Corollary 8.8. Let the uncertain model set is represented with Figure 8.2 with $\Delta_u \in \mathcal{B}\mathbf{\Delta_u}$. Then, the maximum gain of the SISO uncertain model set P_{ij} is smaller than

β, $\max_{P_{ij}\in\mathcal{P}_{ij}} \bar{\sigma}(P_{ij}) < \beta$, iff

$$\mu_{\bar{\mathbf{\Delta}}}\left(\begin{bmatrix} \hat{H}_{11} & \hat{H}_{12}u_j^T \\ \frac{1}{\beta}u_i\hat{H}_{21} & \frac{1}{\beta}u_i\hat{H}_{22}u_j^T \end{bmatrix}\right) < 1. \tag{8.19}$$

If $\mu(\hat{H}_{11}) \geq 1$, define $\max_{P\in\mathcal{P}} \bar{\sigma}(P) = \infty$.

Using the theorem 8.7 and corollary 8.8 and applying bisection over β, the maximum gain of the uncertain model can be obtained. These upper bounds are equal to skewed-μ test, $\mu_{s,\bar{\mathbf{\Delta}}}(\hat{H})$, and its solution can be obtained by computing standard μ iteratively for the modified matrix given previously. Finally, instead of μ, its upper and lower bounds are calculated and used in these tests.

CHAPTER 9

ROBUST CONTROLLER SYNTHESIS

In this section, robust controller design method is reviewed for the determined uncertain model set $\mathcal{P}^{\text{dyn}}$. For the identified parametric uncertainty bound W_γ, the generalized plant (9.1) is obtained. Structured singular value synthesis (9.2) is used for this generalized structure depicted in Figure 9.1, where $\hat{M} = \mathcal{F}_l(G, C)$ is the lower LFT that is used during worst-case performance evaluation [27].

$$G = \left[\begin{array}{c|cc|c} W_\gamma \hat{D}^{-1} N_c & 0 & W_\gamma \hat{D}^{-1} V_1 & W_\gamma \hat{D}^{-1} \\ \hline W_y(D_c + \hat{P} N_c) & 0 & W_y \hat{P} V_1 & W_y \hat{P} \\ 0 & 0 & W_u V_1 & W_u \\ \hline -(D_c + \hat{P} N_c) & V_2 & -\hat{P} V_1 & -\hat{P} \end{array}\right] \tag{9.1}$$

$$C^{\text{RP}} = \arg\min_C J_{WC}(\mathcal{P}, C) = \arg\min_C \sup_{w \in [0, 2\pi)} \mu_s \left(\mathcal{F}_l \left(G(e^{jw}), C(e^{jw}) \right) \right) \tag{9.2}$$

Standard μ synthesis aims to optimize robustness and performance at the same time. In other words, it tries to maximize the uncertainty bound while preserving stability. Therefore, this method is not suitable for problems where the uncertainty is already determined by model validation procedure and required robustness is known. This arises the definition of skewed-μ.

The skewed-μ definition in (9.3) results when one of the uncertainty block is fixed and the other one is varying. The norm bound in uncertainty channel $v \to z$ is fixed at γ, while the norm bound in the performance channel $w \to e$ is to be minimized [27]. (Since identified uncertainty bound W_γ is already included in G, $\gamma = 1$ is satisfied in this analysis.)

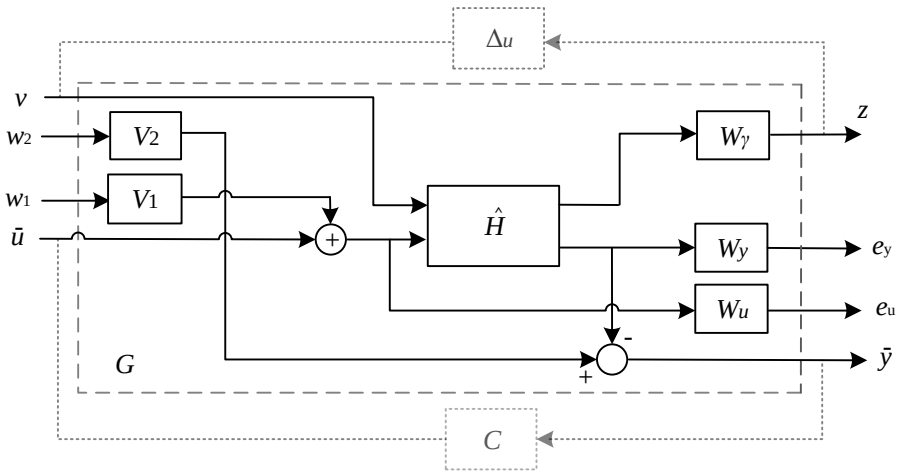

Figure 9.1: Generalized plant

$$\mu_s = \max_{\left\| \begin{bmatrix} v \\ w \end{bmatrix} \right\|_2 = 1} \left\{ a \;\middle|\; \begin{array}{c} \frac{1}{\gamma}\|v\|_2 \leqslant \|z\|_2 \\ a\|w\|_2 \leqslant \|e\|_2 \end{array} \right\} \tag{9.3}$$

Solution method of skewed-μ synthesis is $D-K$ iterations as in the standard case. However, the aim of the $D-K$ iterations is slightly modified as (9.4) by introducing another matrix (9.5) with appropriate dimensions that is updated at each iteration.

$$\min_{K,D} \|DU\hat{M}D^{-1}\|_\infty \tag{9.4}$$

$$U = \begin{bmatrix} I_n & 0 \\ 0 & \frac{1}{\mu_s} I_{n_p} \end{bmatrix} \tag{9.5}$$

By iterating on μ_s until $\mu_s = \mu(U\hat{M}) = 1$, robust controller (9.2) can be synthesized with available software developed for the standart μ synthesis [51, 85].

CHAPTER 10

PROTOTYPE AND SYSTEM ARCHITECTURE OF THE UNCOMMON QUADROTOR CONFIGURATION

In this chapter, a prototype of the proposed quadrotor is discussed. This device is constructed as a first proof of concept prototype, and it is used to test and verify the required flight functionalities. More advanced and optimized solution in terms of hardware design will be left for future research.

10.1 Prototype

Most of the electrical and mechanical parts of the first prototype of the vehicle is constructed using low-cost off-the-shelf devices available in UAV laboratory of the METU EEE department. Only 3D printed tilt mechanisms and aluminum main frame are specifically designed for this case. T-Motor KV400 with 16 inches propeller is used corresponding to large rotor in this configuration. Similarly, T-Motor KV830 with 9 inches propeller corresponds to small rotor. 3D printed tilt mechanism together with Savöx SA-1256 servo motor which can rotate 60° in 0.18 seconds are used to tilt the small rotors as depicted in Figure 10.1. Hobbywing Quattro four-channel electronic speed controller (ESC) is used to power the brushless motors. This ESC can supply 20A continuous current to each channel, and it can be powered with 2-4S Lipo battery. As a power source Gens ace 4S (14.8V) Lipo battery having 5100mAh capacity and 35C discharge rate is used, and it is placed at the bottom of the quadrotor. Standard landing gears compatible to various frames are used, and they are attached to the corners of the bottom frame. Ublox Neo 7 GPS-Compass module, 3DR 433Mhz radio telemetry kit and Futaba 2.4Ghz R2008SB receiver are also attached to the top

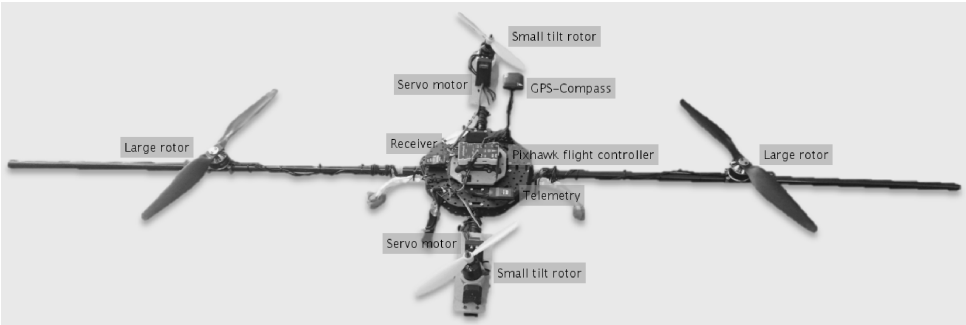

Figure 10.1: Prototype of the uncommon quadrotor configuration

frame. Moreover, clone mRo Pixhawk flight controller board are mounted with a vibration damper in the middle of top frame. This board is fully compatible with Pixhawk/PX4 open source flight control software that is intended to be used in this thesis.

This prototype has a nominal mass of 2.7 kg, and it is represented in Figure 10.1.

10.2 System architecture

Pixhawk control board includes 32-bit ARM Cortex M4 processor running NuttX real-time operating system. Flight controller runs at 400 Hz and evaluates different modules. 3-axis L3GD20 gyroscope and LSM303D accelerometer/magnetometer, Ublox Neo 7 GPS-Compass module, MS5611-01BA03 barometer measurements are taken. Using these sensor measurements Extended Kalman filter (EKF) algorithm provides estimates of local position ξ, velocity $\dot{\xi} = V^B$, Euler angles η and sensors' biases to correct the measurements. Corrected gyro measurements Ω and these EKF state estimates are used in the cascaded local position/attitude control loops as discussed previously in Chapter 3.

GPS and telemetry are connected to the control board through serial ports. Various flight data are sent to a ground control station with telemetry using MAVLink communication protocol. Similarly, different commands are taken from a ground control station. Moreover, joystick inputs are also taken through R2008SB S.BUS receiver. According to attitude controller desired thrust and torques are calculated. Later, these demands are mapped to rotors and tilt angles with multiplication by rotor mixing

matrix. Then, desired rotor speeds and tilt angles are calculated. However, to regulate motor speed and tilt angle, these parameters should be mapped to corresponding PWM signals. These is achieved by using PWM output channels of the control board. Then, electronic speed controller regulates the required speed according to these signals. Similarly, servo motors regulate the required tilt angle according to commanded PWM signals. More detailed information about the PX4 open source flight control software can be found in [86, 87]. The main objective of this thesis is to customize this available software for this uncommon quadrotor configuration to reach a convenient solution. Firstly, PID type angular rate and local velocity and P type Euler angle and local position controllers are tuned manually to give sufficient performance. Later, by injecting multisine signal into the inner attitude rate control reference when the quadrotor is stabilized in hover conditions, system identification experiments are conducted. Then, using combined identification and robust control method, attitude controller is synthesized. Finally, available attitude controller module is customized for the designed robust controller, and it is tested in flight experiments.

CHAPTER 11

QUADROTOR ATTITUDE CONTROL: SYSTEM IDENTIFICATION AND ROBUST CONTROL

Control relevant identification and controller design method discussed in the previous chapters are applied to the prototype of the proposed quadrotor configuration. The accuracy of the attitude control is directly related to inner rate control loop performance if cascade structure in Figure 11.1 is used. The main motivation of this chapter is to obtain high performance rate loop. Therefore, control design is performed for three-input three-output subsystem corresponding to attitude rate control as depicted in Figure 11.1. Euler angle controller and other translational dynamics are controlled by PID and P controllers which give sufficient performance. Since estimate of equivalent model P_o is not found yet, PI rate and P angle controllers are tuned manually in flight by investigating the command tracking performances of resulting attitude control loops. Firstly, estimate of equivalent model P_o is obtained from flight tests when the quadrotor is stabilized by these controllers. Next, loop shaping weighting filters and estimates of $\{N_o, D_o\}$ are found. Coprime factors $\{\hat{N}, \hat{D}\}$ of $\hat{P}$ and

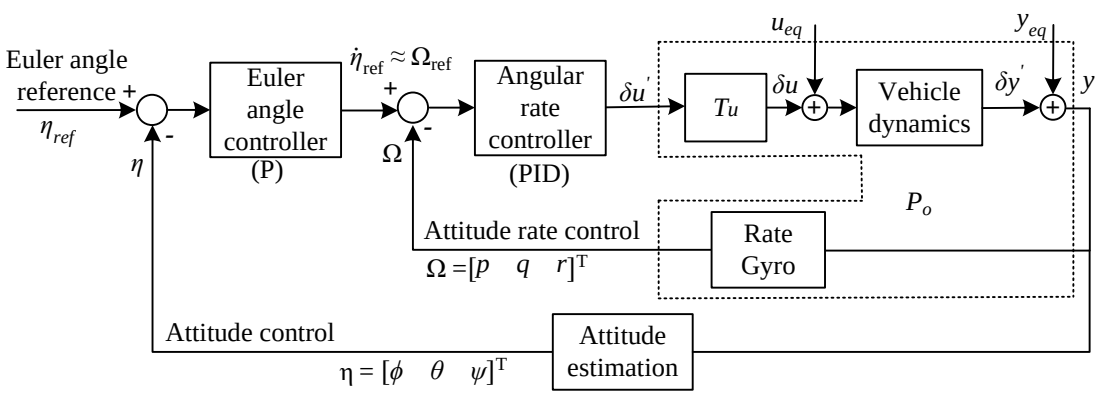

Figure 11.1: Cascade control structure for attitude control

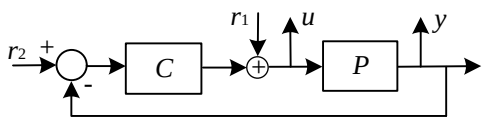

Figure 11.2: Feedback configuration

uncertainty bound W_γ are found, and they are used during controller synthesis. By evaluating the attitude rate loop constructed with manually tuned PI rate controller and estimate of P_o, sufficient gain and phase margins are obtained. Further increasing the gains of PI controller is not preferred since it will diminish the stability margins and give poor performance as discussed in Section 11.1.1. Therefore, the PI rate controller that is present during identification test is also used in different flight tests. Later, performance improvement with the designed robust controller is analyzed. Both theoretical and experimental results indicate the performance improvement. Finally, flight experiments show performance improvement compared to the standard PI based design that satisfies required stability margins.

11.1 Frequency response function identification

Frequency response functions are derived by manipulating mapping (11.1) for the feedback configuration in Figure 11.2.

$$T(P,C): \begin{bmatrix} r_2 \\ r_1 \end{bmatrix} \rightarrow \begin{bmatrix} y \\ u \end{bmatrix} = \begin{bmatrix} P \\ I \end{bmatrix} (I + CP)^{-1} \begin{bmatrix} C & I \end{bmatrix} \tag{11.1}$$

During identification tests, signals r_2, u and y are measured, and r_2 excitation signal is applied and r_1 is kept at zero. Therefore, the following equation is obtained where the DFTs of measured signals $\mathcal{R}_2^{\langle j \rangle} \in \mathbb{C}^{3\times 1}$, $\mathcal{U}^{\langle j \rangle} \in \mathbb{C}^{3\times 1}$ and $\mathcal{Y}^{\langle j \rangle} \in \mathbb{C}^{3\times 1}$ on the DFT grid Ω are obtained where $\langle j \rangle$ represents the jth test. Performing three tests to span the required space for P_o leads to

$$\begin{bmatrix} \mathcal{Y}^{\langle 1 \rangle} & \mathcal{Y}^{\langle 2 \rangle} & \mathcal{Y}^{\langle 3 \rangle} \\ \mathcal{U}^{\langle 1 \rangle} & \mathcal{U}^{\langle 2 \rangle} & \mathcal{U}^{\langle 3 \rangle} \end{bmatrix} = \begin{bmatrix} P_o \\ I \end{bmatrix} (I + C^{\text{exp}} P_o)^{-1} C^{\text{exp}} \begin{bmatrix} \mathcal{R}_2^{\langle 1 \rangle} & \mathcal{R}_2^{\langle 2 \rangle} & \mathcal{R}_2^{\langle 3 \rangle} \end{bmatrix} . \tag{11.2}$$

Figure 11.3: Overlay of several snapshots during sequential excitation: roll excitation (left), pitch excitation (center), yaw excitation (right). See video [online].

Then, the estimation of $T(P_o, C^{\text{exp}})$ is obtained as

$$\tilde{T}(P_o, C^{\text{exp}}) = \begin{bmatrix} \mathcal{Y}^{\langle 1\rangle} & \mathcal{Y}^{\langle 2\rangle} & \mathcal{Y}^{\langle 3\rangle} \\ \mathcal{U}^{\langle 1\rangle} & \mathcal{U}^{\langle 2\rangle} & \mathcal{U}^{\langle 3\rangle} \end{bmatrix} \begin{bmatrix} \mathcal{R}_2^{\langle 1\rangle} & \mathcal{R}_2^{\langle 2\rangle} & \mathcal{R}_2^{\langle 3\rangle} \end{bmatrix}^{-1} \begin{bmatrix} I & (C^{\text{exp}})^{-1} \end{bmatrix}, \quad (11.3)$$

on the Ω^{id} grid given as [88]

$$\Omega^{\text{id}} = \left\{ w \mid w \in \Omega,\ \det\left(\begin{bmatrix} \mathcal{R}_2^{\langle 1\rangle} & \mathcal{R}_2^{\langle 2\rangle} & \mathcal{R}_2^{\langle 3\rangle} \end{bmatrix} \right) \neq 0 \right\}. \quad (11.4)$$

Multisine input signals are used to reduce the variances of estimates by using averaging properties of periodic signals as discussed in Chapter 7 as

$$\begin{bmatrix} r_2^{\langle 1\rangle}(t) & r_2^{\langle 2\rangle}(t) & r_2^{\langle 3\rangle}(t) \end{bmatrix} = \bar{\Omega}_{ref} + Q \sum_k a_k \sin(w_k t + \phi_k), \quad (11.5)$$

where w_k, a_k and ϕ_k denote corresponding frequency, amplitude and phase, respectively. In addition, index k denotes the kth frequency. When $\bar{\Omega}_{ref}$ is constant, the condition, $\det\left(\begin{bmatrix} \mathcal{R}_2^{\langle 1\rangle} & \mathcal{R}_2^{\langle 2\rangle} & \mathcal{R}_2^{\langle 3\rangle} \end{bmatrix} \right) \neq 0$ requires full rank Q to span all input space, and $w_k \in \Omega^{\text{id}}$ is satisfied. However, $\bar{\Omega}_{ref}$ given by (11.6) is not constant due to cascaded loops in this case, and it denotes reference signals created by outer Euler angle controller to minimize the attitude error.

$$\bar{\Omega}_{ref} = \begin{bmatrix} p_{ref}^{\langle 1\rangle}(t) & p_{ref}^{\langle 2\rangle}(t) & p_{ref}^{\langle 3\rangle}(t) \\ q_{ref}^{\langle 1\rangle}(t) & q_{ref}^{\langle 2\rangle}(t) & q_{ref}^{\langle 3\rangle}(t) \\ r_{ref}^{\langle 1\rangle}(t) & r_{ref}^{\langle 2\rangle}(t) & r_{ref}^{\langle 3\rangle}(t) \end{bmatrix} \quad (11.6)$$

When $\bar{\Omega}_{ref}$ is not constant, $Q = I$ may be used. In this case, approximately diagonal $\begin{bmatrix} \mathcal{R}_2^{\langle 1\rangle} & \mathcal{R}_2^{\langle 2\rangle} & \mathcal{R}_2^{\langle 3\rangle} \end{bmatrix}$ with large diagonal entries can be obtained. Even if diagonal entries may become smaller in the low frequencies due to outer loop, approximate diagonality is expected to hold. In short, the invertibility condition is not violated due

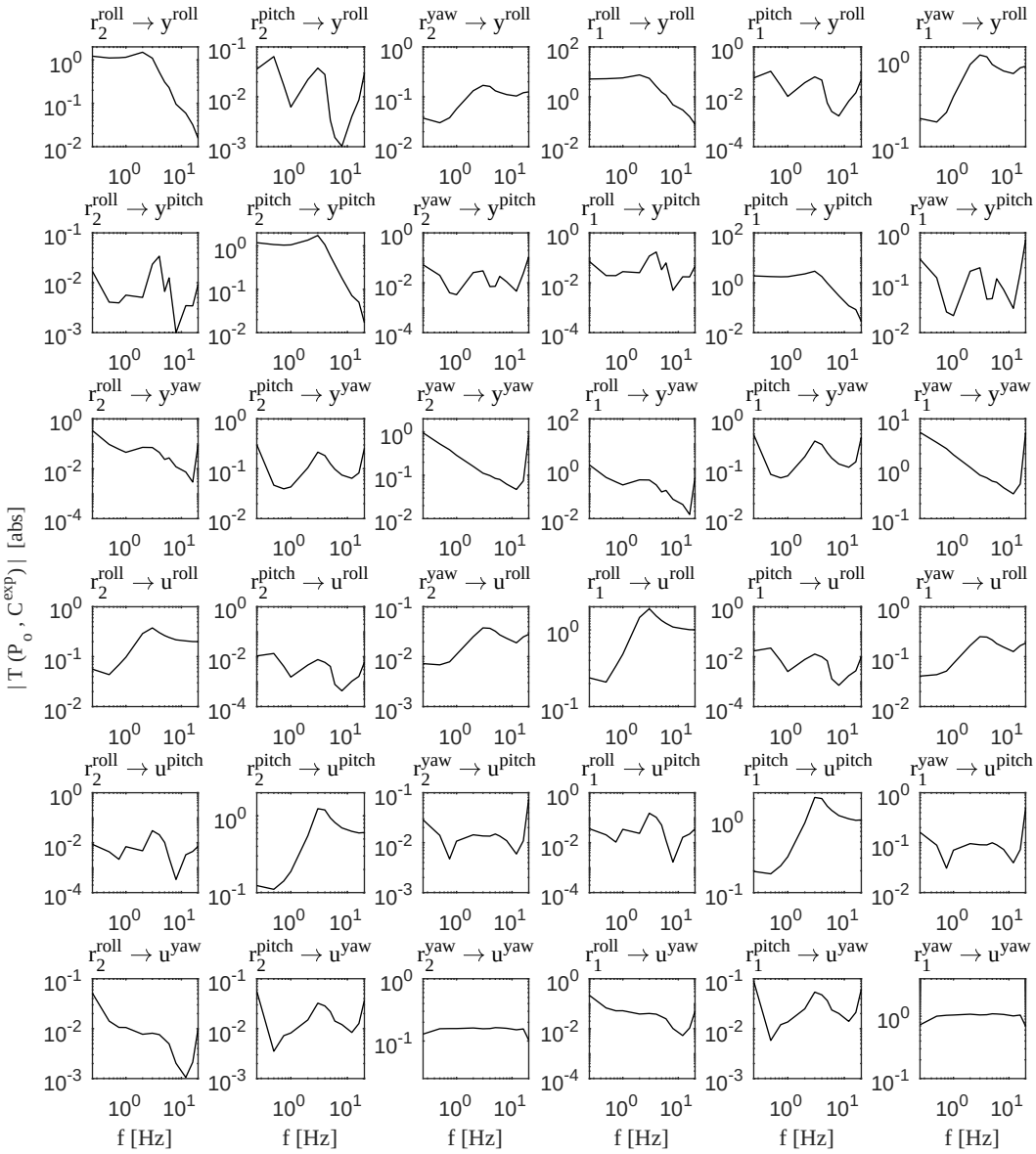

Figure 11.4: Identified frequency response function of $\tilde{T}(P_o, C^{\text{exp}})$ on Ω^{id}

to outer loop in the experiments, and the same $w_k \in \Omega^{\text{id}}$ grid is used as in the case of constant $\bar{\Omega}_{ref}$. For identification experiments, $Q = I$ corresponds to sequential excitation in the roll, pitch and yaw axes of the quadrotor platform as depicted in Figure 11.3. In addition, the estimation of $T(P_o, C^{\text{exp}})$ is shown in Figure 11.4. Finally, the estimate of P_o is obtained by $\tilde{P}_o = \tilde{T}_{11}\tilde{T}_{21}^{-1}$ on the Ω^{id} and depicted in Figure 11.5.

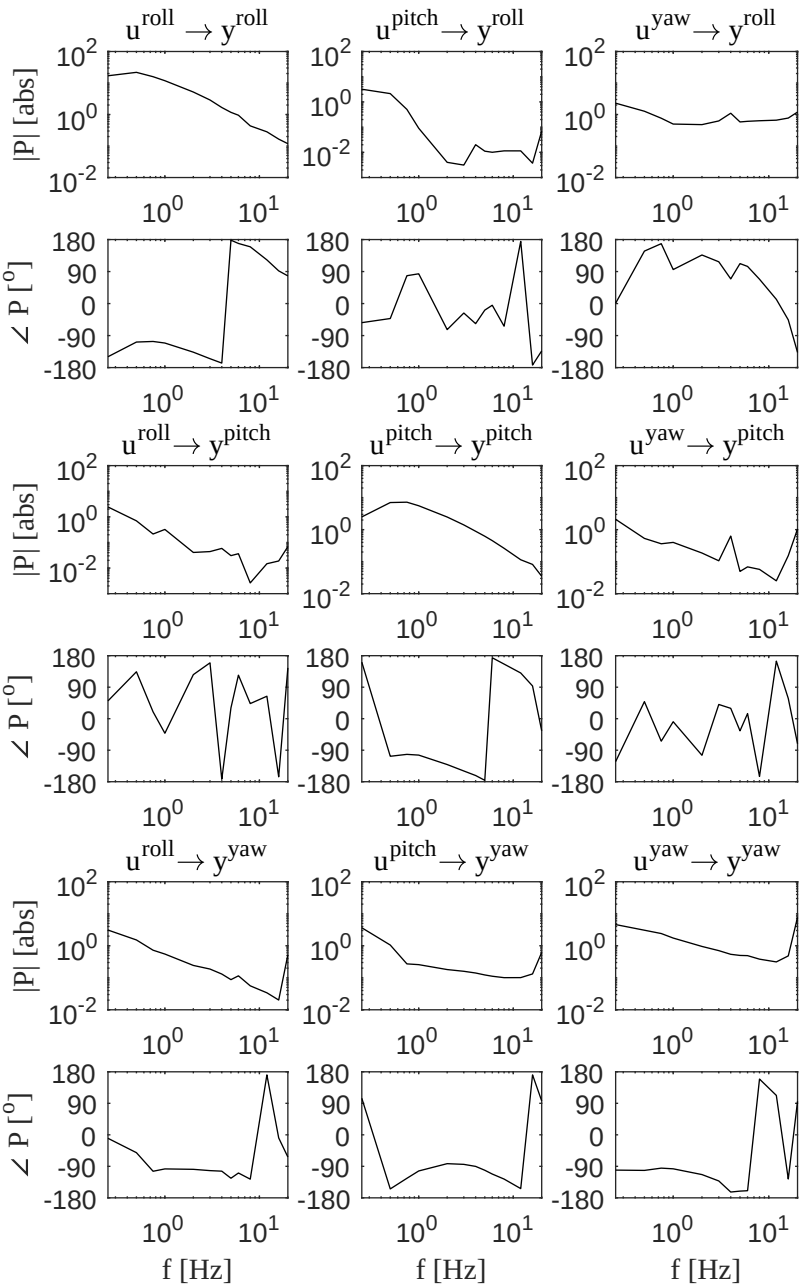

Figure 11.5: Identified frequency response function of $\tilde{P}_o$ on Ω^{id}

Diagonal elements of $\tilde{P}_o$ illustrate that these dynamics include first order inertia line and time delay due to sensor and motor speed control. Moreover, due to inexact static input decoupling matrix T_u, small coupling between different axes can be observed in the off-diagonal elements. Especially in roll and pitch axes, these couplings are very small in low frequencies and around the crossover region when compared to diagonal elements. Therefore, their effects on the control design may be insignificant. Therefore, diagonal controller can give high performance in these axes. Around crossover region, roll and yaw axes coupling and diagonal element can be in comparable magnitudes. This may reduce the performance for a SISO controller. Hence, MIMO controller may give better performance in yaw axis. In other words, with diagonal controller, sufficient performance can be obtained since the off-diagonal elements are small compared to diagonals around the crossover region. Therefore, PI rate controllers can give sufficient performance. If coupling terms are large, performances of diagonal controllers reduce, and more advanced controllers are required similar to the designed robust controller in this thesis [27, 51]. Similarly, nonparametric estimate of $\{N_o, D_o\}$ on Ω^{id} is obtained by (11.7) as discussed in Chapter 5.

$$\begin{bmatrix} \tilde{N}_o \\ \tilde{D}_o \end{bmatrix} = \tilde{T}(P_o, C^{\text{exp}}) V \tilde{N}_e^* \tag{11.7}$$

In this thesis, following frequency grid Ω^{id} is used during identification tests, and the data sets are obtained based on this frequency grid.

$$\Omega^{\text{id}} = 2\pi\{0.25, 0.5, 0.75, 1, 2, 3, 4, 5, 6, 8, 12, 16, 20\} \tag{11.8}$$

It is known that multisine signal is periodic. Here, it is assumed that the input signal in (11.5) is also periodic with a period of 4 seconds. For 400 Hz sampling frequency, this signal is periodic in every $N = 1600$ samples. Moreover, the phases of multisine signal are selected according to Schröder rule [80]. The identification tests take nearly 120 seconds which correspond to 30-period input excitation tests, which gives sufficiently accurate FRFs and covariance estimate of the disturbances for the model validation procedure as reported in Chapter 7.

11.1.1 Weight determination

Precise attitude control requires high bandwidth for sufficient disturbance rejection and accurate command tracking. Time delay of the gyroscopes, bandwidth of motor control and flexible modes of the structure may limit the achievable bandwidth. Moreover, model uncertainties due to possible nonlinearities and coupling effects due to wrong decoupling matrix should be addressed suitably. Therefore, a certain value for the robustness margin is required which directs robust control methods.

Previously, PI rate controller was tuned manually in flight by investigating the command tracking performances of resulting attitude control loops since estimate of P_o was not found yet. Estimate of P_o is now obtained from identification tests as discussed above using this controller. By evaluating the attitude rate loop constructed with manually tuned PI rate controller and estimate $\tilde{P}_o$, sufficient gain and phase margins are obtained. In classical control theory, robustness is often specified considering limits on gain margin (GM) and phase margin (PM). According to common rules of thumb, $2 <$ GM < 5 and $30^\circ <$ PM $< 60^\circ$ are needed. These stability margins are often aimed in practice in classical feedback system design [51, 89, 90].

By using the diagonal entries of $\tilde{P}_o$ and manually tuned PI controller, gain and phase margins are investigated. In roll axis, 2 Hz bandwidth, 37° phase margin and 3.9 gain margin are obtained. In pitch axis, 2.65 Hz bandwidth, 34° phase margin and 2.6 gain margin are achieved. For yaw axis, 0.28 Hz bandwidth is reached. As shown in Figure 11.5, yaw axis has a resonance around 20 Hz, and margins need to be determined in this region for a standard PI controller. Since Ω^{id} does not have much frequency component in this region, gain and phase margins could not be determined accurately. During manual tuning in flight, when gain of yaw PI controller was increased, poor performance was obtained. Also, doubling the gain of this controller led to instability in yaw axis. Therefore, approximate gain margin 2 can be assumed in yaw axis.

Phase loss due to finite bandwidth of motor speed control and gyro sensor delay does not allow any gain increase in this PI controller for roll and pitch axes to maintain sufficient margins. For yaw axis, resonance around 20 Hz limits the achievable gain and bandwidth for a standard PI controller. Adding extra lead and lag filters are necessary to improve the performance, but it is not in the scope of this thesis. Therefore, this PI rate controller that is present during identification test is also used in perfor-

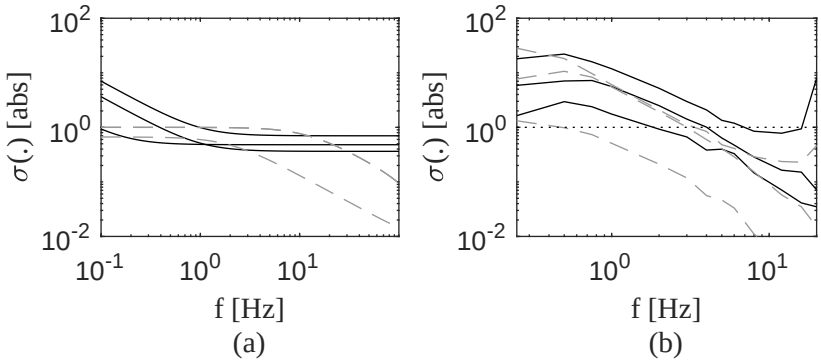

Figure 11.6: (a) Singular values of weighting filters: W_1 (solid black), W_2 (dashed gray). (b) Singular values of FRF estimate $\tilde{P}_o$ (solid black), shaped system $W_2\tilde{P}_oW_1$ (dashed gray).

mance evaluation part. This diagonal controller which gives above stability margins is denoted by C^{exp} in this chapter.

The main motivation is to reach approximately 3 Hz bandwidth in the roll and pitch axes and 0.5 Hz bandwidth in the yaw axis to increase disturbance rejection performance. It is assumed that coupling effects between different axes are small in low frequency range. Therefore, both P and C are approximately diagonal which leads to three different bandwidth definition corresponding to each axis. In this thesis, three different bandwidths f_{roll}, f_{pitch} and f_{yaw} refer to crossover frequencies in the corresponding axes satisfying

$$|P^{rr}C^{rr}(2\pi f_{\text{roll}})| = 1, \quad |P^{pp}C^{pp}(2\pi f_{\text{pitch}})| = 1, \quad |P^{yy}C^{yy}(2\pi f_{\text{yaw}})| = 1\ . \quad (11.9)$$

Here, P^{rr}, P^{pp}, P^{yy} and C^{rr}, C^{pp}, C^{yy} terms indicate the diagonal elements of P and C for the roll, pitch and yaw axes, respectively. These frequencies approximately correspond to the region where $\sigma(PC) = 1$ and $\sigma(CP) = 1$ are satisfied due to diagonality of P and C. In addition, to use similar formulation, the notation f_{bw} is used which may represent f_{roll}, f_{pitch} or f_{yaw} according to axis to be in use.

In this thesis, weighting functions are selected to shape the loop similar to method in [91]. These weighting filters are designed such that W_2PW_1 has desired open loop shape of PC. Since $\hat{P}$ is not found yet, the estimate $\tilde{P}_o$ can be used directly. The weight selection method suggested in [48] for position loops is extended for rate loops. In this respect, W_1 is selected to have an integrator for good disturbance rejection, and its cut-off is at $f_{bw}/3$ as shown in Figure 11.6 where $f_{bw} = 3$ Hz for the

roll and pitch axes and $f_{bw} = 0.5$ for the yaw axis. W_2 is selected to satisfy 0 slope around f_{bw} such that desired open loop shape has -1 slope in this region for sufficient robustness. Moreover, high frequency roll-off beyond $4f_{bw}$ is also enforced with W_2. Finally, W_2 and shaped open loop W_2PW_1 are depicted in Figure 11.6.

The two-block problem considered in [91] is equivalent to four-block problem considered in this thesis in terms of control criterion if the following weighting filters are used in (11.12) [91, 92]. In this thesis, this method is followed.

$$W = \begin{bmatrix} W_y & 0 \\ 0 & W_u \end{bmatrix} = \begin{bmatrix} W_2 & 0 \\ 0 & W_1^{-1} \end{bmatrix} \tag{11.10}$$

$$V = \begin{bmatrix} V_2 & 0 \\ 0 & V_1 \end{bmatrix} = \begin{bmatrix} W_2^{-1} & 0 \\ 0 & W_1 \end{bmatrix} \tag{11.11}$$

$$J(P, C) = \|WT(P, C)V\|_\infty \tag{11.12}$$

11.1.2 Coprime factorization

Nonparametric frequency response functions of $\tilde{N}_o$ and $\tilde{D}_o$ are obtained by using (11.7). The following parametrization is introduced for $\{\hat{N}, \hat{D}\}$

$$\begin{bmatrix} \hat{N}(\theta) \\ \hat{D}(\theta) \end{bmatrix} = \begin{bmatrix} B(\theta) \\ A(\theta) \end{bmatrix} (\tilde{D}_e A(\theta) + \tilde{N}_{e,2} V_2^{-1} B(\theta))^{-1} , \tag{11.13}$$

where $B \in \mathbb{R}^{3\times3}[z]$ and $A \in \mathbb{R}^{3\times3}[z]$ are polynomial matrices defined as

$$B(\theta) = [B_3]\, z^3 + [B_2]\, z^2 + [B_1]\, z + [B_0] \tag{11.14}$$

$$A(\theta) = \begin{bmatrix} 1 & 0 & 0 \\ 0 & 1 & 0 \\ 0 & 0 & 1 \end{bmatrix} z^4 + [A_3]\, z^3 + [A_2]\, z^2 + [A_1]\, z + [A_0] \tag{11.15}$$

with $B_0, B_1, B_2, B_3, A_0, A_1, A_2, A_3 \in \mathbb{R}^{3\times3}$. Therefore, $\hat{P}$ is defined as a right MFD as [55]

$$\hat{P}(\theta) = \hat{N}(\theta)\hat{D}(\theta)^{-1} = B(\theta)A(\theta)^{-1}. \tag{11.16}$$

Consequently using this model parametrization, there are 72 unknown parameters to be estimated. Polynomial vector is constructed as

$$\text{vec}\left(\begin{bmatrix} B(\theta) \\ A(\theta) \end{bmatrix}\right) = \varphi_4\theta_4 + \varphi_3\theta_3 + \varphi_2\theta_2 + \varphi_1\theta_1 + \varphi_0\theta_0 \in \mathbb{R}^{18\times 1}[z], \tag{11.17}$$

where

- $\varphi_4,\ \varphi_3,\ \varphi_2,\ \varphi_1,\ \varphi_0 \in \mathbb{R}^{18\times 18}[z]$,
- $\theta = [\theta_0^T\ \theta_1^T\ \theta_2^T\ \theta_3^T]^T \in \mathbb{R}^{72\times 1}$ is the parameter vector to be determined,
- $\theta_4 \in \mathbb{R}^{18\times 1}$ is pre-determined to satisfy degree constratint of $B(\theta)$ and monic constraint of $A(\theta)$.

As mentioned in Chapter 5, linear least squares estimation of these coprime factors is obtained by using data-dependent orthonormal polynomials. In each SK iteration new $\varphi_4,\ \varphi_3,\ \varphi_2,\ \varphi_1,\ \varphi_0$ polynomial matrices are found to satisfy $\kappa(W_{\text{lsq}}^{\langle k\rangle}\Phi) = 1$, and parameters are estimated by solving optimally conditioned linear least squares problem. Estimates obtained from linear least squares problem are used in the subsequent Gauss-Newton optimization step. The original nonlinear least squares problem is solved by Gauss-Newton algorithm and more accurate model is obtained. These models are shown in Figure 11.7 and 11.8. Herein, parametrization (11.13) leads to 25th order coprime factors $\{\hat{N}, \hat{D}\}$. As observed in Figure 11.7 and 11.8, estimation errors between the diagonal elements of $\{\hat{N}, \hat{D}\}$ and $\{N_o, D_o\}$ are relatively small since they mostly dominate the robust control criterion. Errors in the remaining elements may seem larger; however, their effects to robust control are not significant. Resulting nominal model gives sufficiently small nominal model identification criterion in (5.22). Therefore, this nominal model and coprime factors are appropriate for subsequent robust control synthesis.

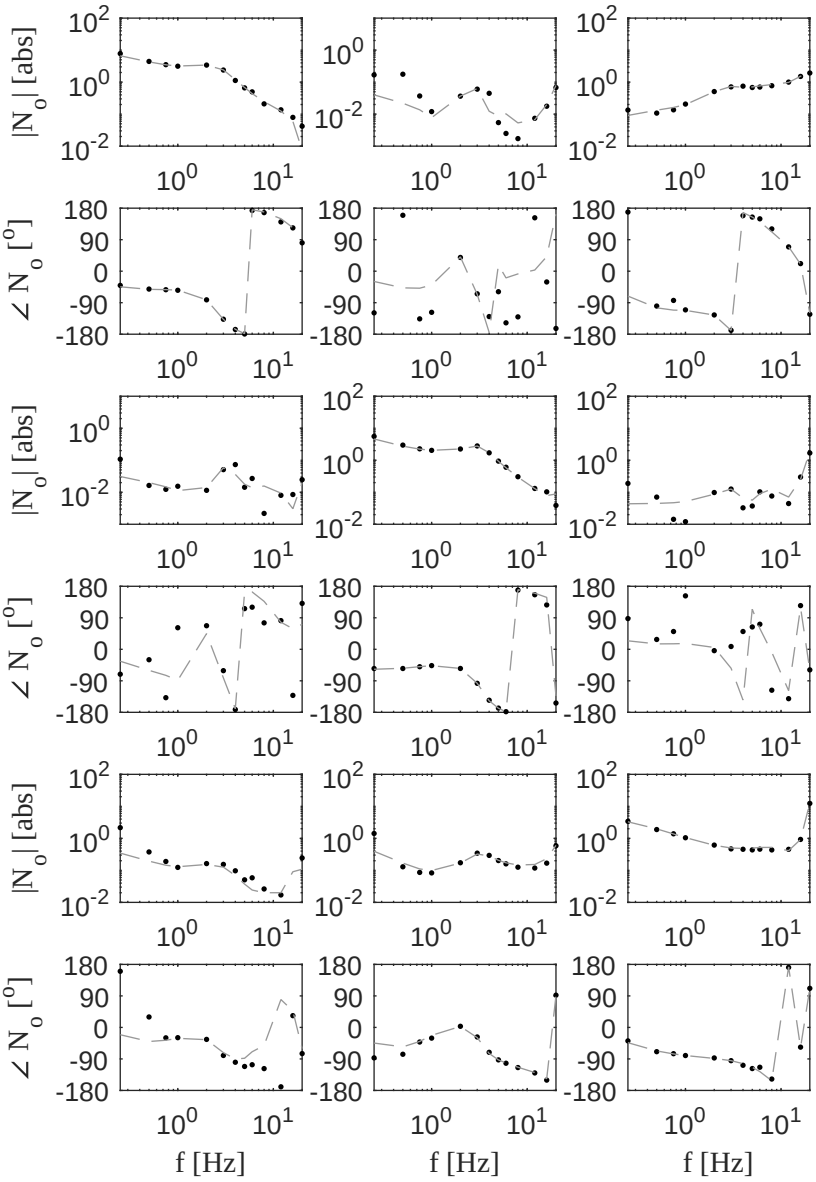

Figure 11.7: Coprime factor: nonparametric N_o (black dots), 25th order parametric coprime factor $\hat{N}$ (dashed gray).

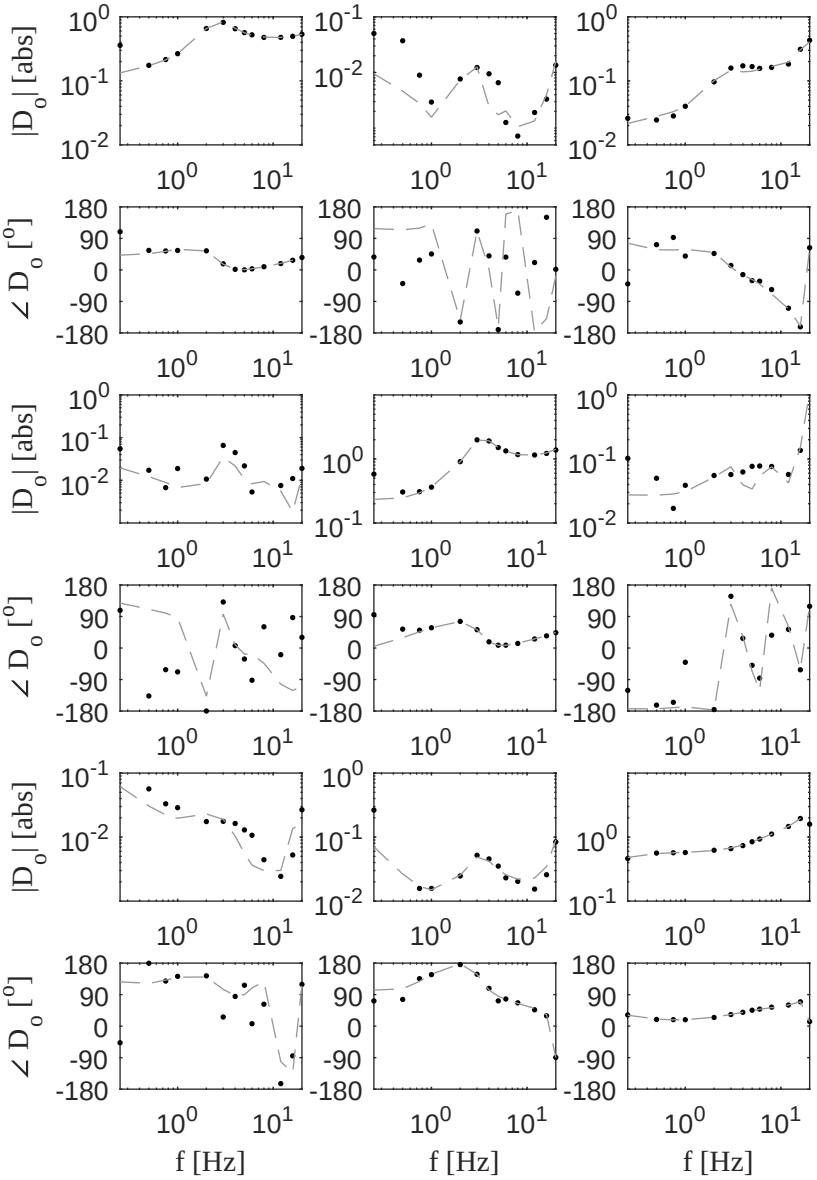

Figure 11.8: Coprime factor: nonparametric D_o (black dots), 25th order parametric coprime factor $\hat{D}$ (dashed gray).

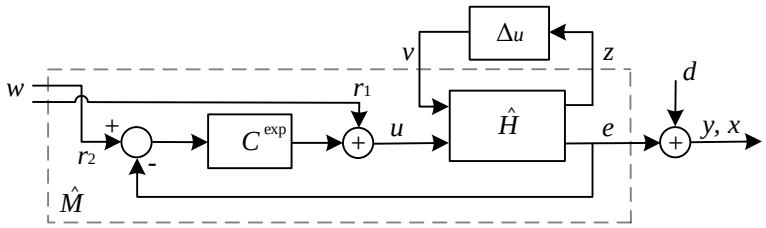

Figure 11.9: Model validation framework

11.2 Construction of model set

The identified coprime factorization is used to construct the robust-control-relevant model set $\mathcal{P}^{\text{RCR}}$. As discussed previously in Chapter 5, this set is constructed as

$$\mathcal{P}^{\text{RCR}} = \left\{ P \mid P \in \mathcal{P}^{\text{DY}},\ \{\hat{N}, \hat{D}\} \text{ satisfies (11.19)},\ \{N_c, D_c\} \text{ satisfies (11.20)} \right\}, \tag{11.18}$$

where $\{\hat{N}, \hat{D}\}$ and $\{N_c, D_c\}$ are determined by

$$\begin{bmatrix} \hat{N} \\ \hat{D} \end{bmatrix} = \begin{bmatrix} \hat{P} \\ I \end{bmatrix} (\tilde{D}_e + \tilde{N}_{e,2} V_2^{-1} \hat{P})^{-1}, \tag{11.19}$$

$$\begin{bmatrix} W_u N_c \\ W_y D_c \end{bmatrix}^* \begin{bmatrix} W_u N_c \\ W_y D_c \end{bmatrix} = I. \tag{11.20}$$

The required uncertainty bound γ is estimated by applying validation-based uncertainty modeling as discussed in Chapter 7.

During this procedure, structure originated from Figure 5.3 is used, and it is assumed that u is known exactly, and it is omitted from (5.16). Since the validation procedure is applied by using measured variables, weighting filters are also omitted, i.e., $x = y$ and $w = [r_2^T\ r_1^T]^T$, and structure depicted in Figure 11.9 is used. Therefore, the following matrix is used during model validation procedure.

$$\hat{M}^{\text{DY}}(\hat{P}, C^{\text{exp}}) = \left[\begin{array}{c|c} 0 & (\hat{D} + C^{\text{exp}} \hat{N})^{-1} \begin{bmatrix} C^{\text{exp}} & I \end{bmatrix} \\ \hline D_c & \hat{P}(I + C^{\text{exp}} \hat{P})^{-1} \begin{bmatrix} C^{\text{exp}} & I \end{bmatrix} \end{array} \right] \tag{11.21}$$

After that, data sets are collected by using excitation signal (11.5) with the same frequency components $w_i \in \Omega^{\text{id}}$ and same phases ϕ_k as the signals used during identification experiments. Sequential excitation in the roll, pitch and yaw axes of the

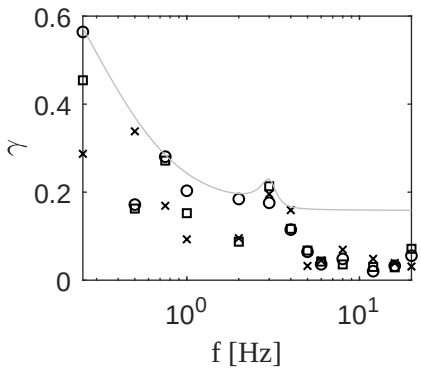

Figure 11.10: Resulting model uncertainty norm bound $\tilde{\gamma}(w_i)$ on the identification grid: data set obtained with: 1) 100% battery level ($\times$), 2) 80% battery level ($\circ$), 3) 60% battery level ($\square$), and parametric overbound W_γ (solid gray).

quadrotor platform are repeated for model validation. Summation of the signals obtained in these three tests is used to quantify the uncertainty for different battery levels. By solving FDMVOP defined in Chapter 7 for each battery level and frequency grid Ω^{id}, uncertainty bounds are obtained. Different norm-bounds $\tilde{\gamma}(w_i)$ as defined by (11.22) are shown in Figure 11.10 for different battery levels.

$$\tilde{\gamma}(w_i) = \bar{\sigma}(\Delta_u(w_i)),\ w_i \in \Omega^{\text{id}} \tag{11.22}$$

Then, model uncertainty bound is obtained as

$$\gamma = \sup_{w_i \in \Omega^{\text{id}}} \tilde{\gamma}(w_i) = 0.564\ , \tag{11.23}$$

and bistable dynamic overbound W_γ is illustrated in Figure 11.10. After that, two model sets are constructed using static overbound γ and dynamic overbound W_γ as

$$\mathcal{P}^{\text{sta}} = \{P \in \mathcal{P}^{\text{RCR}} \mid \|\Delta_u\|_\infty \leqslant \gamma\}, \tag{11.24}$$

$$\mathcal{P}^{\text{dyn}} = \{P \in \mathcal{P}^{\text{RCR}} \mid \|\Delta_u W_\gamma^{-1}\|_\infty \leqslant 1\}. \tag{11.25}$$

Using tight dynamic overbound W_γ does not affect the performance bound in (11.26); however, it has certain advantages. Mainly, it reduces possible conservatism compared to static overbound during controller synthesis since $\mathcal{P}^{\text{dyn}} \in \mathcal{P}^{\text{sta}}$. Moreover, it also reduces possible conservatism due to use of C^{exp} instead of C^{RP} in identification step, and due to use of upper bound in triangle inequality for (5.40) [27].

$$J_{WC}(\mathcal{P}^{\text{RCR}}, C^{\text{exp}}) \leqslant J(\hat{P}, C^{\text{exp}}) + \gamma \tag{11.26}$$

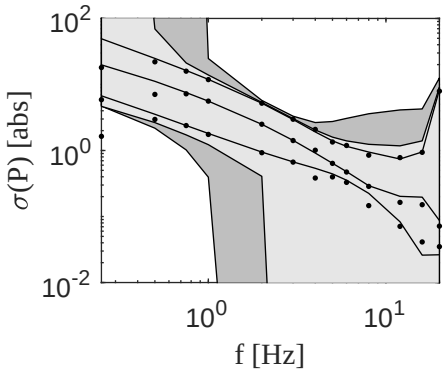

Figure 11.11: Singular values of nonparametric estimate $\tilde{P}_o$ (black dots), nominal model $\hat{P}$ (solid black), model set $\mathcal{P}^{\text{dyn}}$ (shaded), and $\mathcal{P}^{\text{sta}}$ (dark shaded).

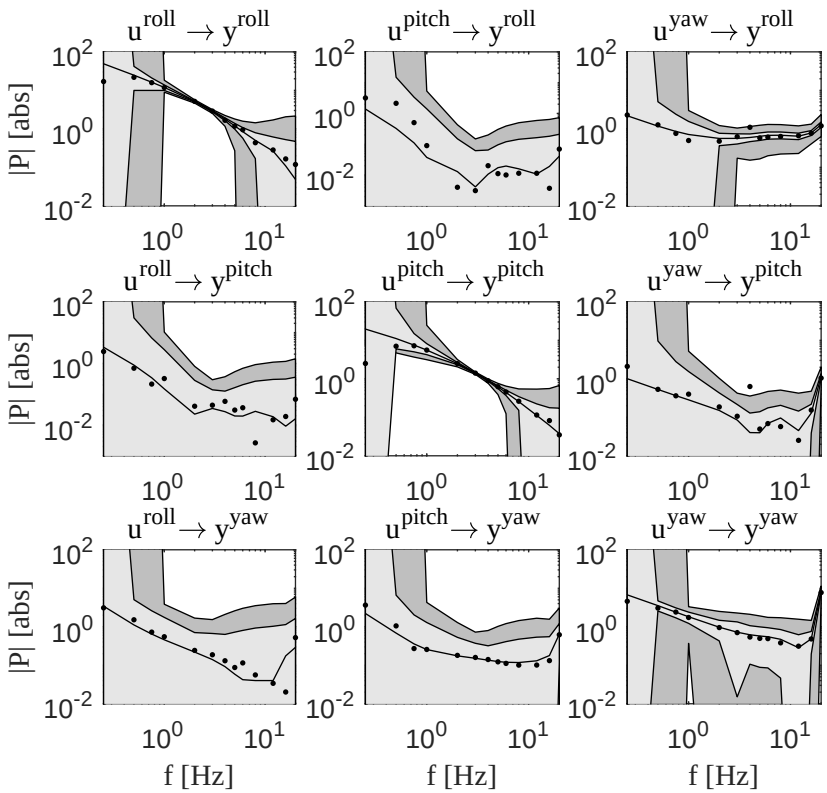

Figure 11.12: Magnitudes of nonparametric estimate $\tilde{P}_o$ (black dots), nominal model $\hat{P}$ (solid black), model set $\mathcal{P}^{\text{dyn}}$ (shaded), and $\mathcal{P}^{\text{sta}}$ (dark shaded).

The resulting model sets are visualized using the method introduced in Chapter 8. Singular values of MIMO uncertain model set is illustrated in Figure 11.11. After that, elementwise singular values are shown in Figure 11.12. In these figures, it is showed that $\mathcal{P}^{\text{dyn}}$ is narrower in the frequency domain compared to $\mathcal{P}^{\text{sta}}$. This fact results from the dynamic bound W_γ use instead of the static bound γ for uncertainty in model set construction. Therefore, possible conservatism is reduced with dynamic bound W_γ use since $\mathcal{P}^{\text{dyn}} \in \mathcal{P}^{\text{sta}}$. In addition, both uncertain model set get narrower around the crossover region which is very essential for high robust performance. Conversely, uncertain sets are relatively large in both low and high frequency regions. Therefore, model sets are uncertain in these frequencies. Next, especially in roll and pitch axes, off-diagonal elements are small compared to diagonal elements. Therefore, in these axes, diagonal controller can give high performance. In yaw axis, a similar observation holds, but around crossover, roll and yaw axes coupling and diagonal element can be in comparable magnitudes. This may affect the performance for a single variate controller. Hence, multivariable controller may give better performance in yaw axis.

11.3 Controller design and implementation

The uncertain model set $\mathcal{P}^{\text{dyn}}$ is used to synthesize a robust controller since it is narrower in the frequency domain $\mathcal{P}^{\text{dyn}} \in \mathcal{P}^{\text{sta}}$. Therefore, resulting robust controller can give higher performance for this uncertain model set. In addition, using standard $\mathcal{H}_\infty$ optimization, C^{NP} is synthesized for the nominal model $\hat{P}$. Gains of these three controllers are illustrated in Figure 11.13 where the input of the controller is error $\epsilon = r_2 - y$, and the output of the controller is control signal u when r_1 is zero.

In Figure 11.13, the designed controllers and C^{exp} are mostly single variate in roll and pitch axes since off-diagonal elements are relatively small compared to diagonal entries in large frequency interval. However, in yaw axis, C^{RP} and C^{NP} show multivariable characteristics. This may improve the performance in this axis.

Next, nominal and worst-case performances of these controllers are given in Table 11.1. It indicates that although C^{NP} gives optimal performance for the nominal model $\hat{P}$, it gives higher worst-case performance for $\mathcal{P}^{\text{dyn}}$ compared to C^{RP}. Moreover, C^{RP} gives improved performance compared to C^{exp} which satisfy certain robustness

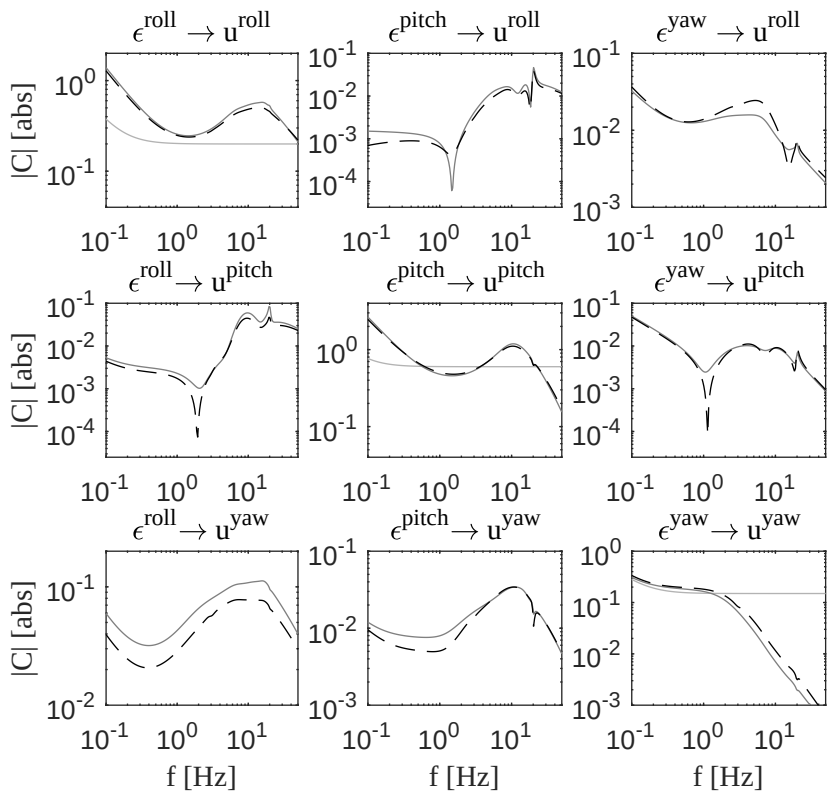

Figure 11.13: Bode magnitude diagrams of C^{exp} (solid gray), C^{NP} (solid dark gray), C^{RP} (dashed black).

margins used in classical feedback design. Herein, smaller performance criterion indicates that achieved bandwidth is closer to the desired one. As reported in [91], $J(P, C) < 4$ is an indicator of successful loop shape. Therefore, C^{RP} has closer properties to desired loop shape. Table 11.1 also indicates that all candidate models in the uncertain model set give similar high performance for C^{RP} since J and J_{WC} are almost equal in this case. Therefore, uncertain model set $\mathcal{P}^{\text{dyn}}$ is indeed robust control relevant. In other words, this tight robust control relevant model set shown in

Table 11.1: Robust control relevant identification and robust control synthesis results:

Controller	Minimized criterion	$J(\hat{P}, C)$	f_{roll}	f_{pitch}	f_{yaw}	$J_{WC}(\mathcal{P}^{\text{dyn}}, C)$
C^{exp}	None (PI)	18.87	2.0	2.65	0.28	18.88
C^{NP}	$J(\hat{P}, C)$	2.86	2.53	2.26	0.33	3.09
C^{RP}	$J_{WC}(\mathcal{P}^{\text{dyn}}, C)$	3.04	2.42	2.31	0.35	3.06

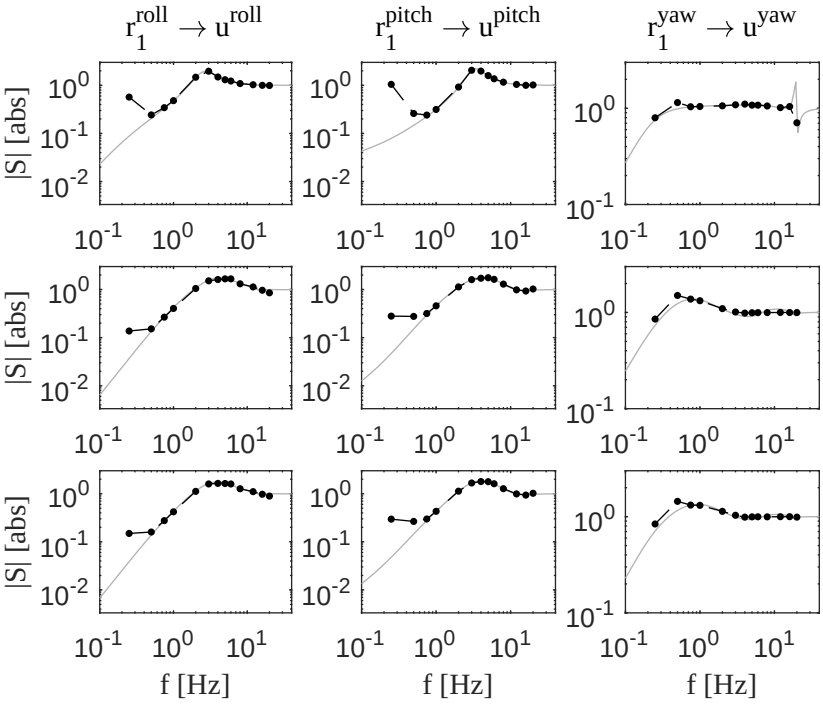

Figure 11.14: Bode magnitude diagrams of diagonal elements of sensitivity function $S = (I + CP)^{-1}$ for nominal model $\hat{P}$ (solid gray), and for identified FRF $\tilde{P}_o(w_i), w_i \in \Omega^{\text{id}}$ (black dots and dashed lines). C^{exp} (top), C^{NP} (middle), C^{RP} (bottom).

Figure 11.12 enables nonconservative controller synthesis as expected.

Theoretical sensitivity functions are obtained by evaluating $S = (I+CP)^{-1}$ for nominal model and for the estimate $\tilde{P}_o$ obtained on Ω^{id}. Sensitivity functions depicted in Figure 11.14 are obtained. These sensitivity responses show the performance improvement in terms of disturbance rejection with C^{RP} and C^{NP} compared to C^{exp}. In other words, disturbance rejection performances are improved in the low frequencies with these controllers since they have relatively large gains as shown in Figure 11.13. As depicted both in Figure 11.5 and 11.12, diagonal entries of nominal model deviate from ideal first order inertia line $1/(Js)$ behavior, and their slopes reduce in the low frequency region for roll and pitch axes. Therefore, optimization based control designs give higher controller gains in this region to satisfy closed loop performance demands. Therefore, resulting controllers have double integral behavior in this region which improves the disturbance rejection performance significantly for these axes. However, in yaw axis model behaves as $1/(Js)$. Therefore, resulting controller

Figure 11.15: Snapshots during hovering: C^{exp} (left), C^{RP} (right). See video [online].

behaves as a single integrator in the low frequencies. In this axis, performance improvement is achieved with increased bandwidth.

As given in Table 11.1, worst-case performance of C^{RP} is smaller than worst-case performance of C^{NP}. Therefore, C^{RP} will give slightly better robust performance when implemented theoretically. Therefore, in addition to C^{exp}, only C^{RP} is implemented on the proposed quadrotor prototype. Performances of these two controllers are compared. Firstly, attitude control performances of these controllers are investigated while the vehicle is stabilized around hover with these controllers as depicted in Figure 11.15.

Main duties of the designed attitude rate controllers are to follow angular rate references from the angle controller and to attenuate exogenous disturbances such as wind. Since attitude error is an important performance indicator, effects of these controllers to attitude error is investigated instead of angular rate. During hovering, small attitude reference signals are generated from the outer local velocity controller. Therefore, reference tracking problem is considered where the performance variable $\epsilon = r_2 - y$ denotes the attitude error. When the vehicle is stabilized around hover, attitude errors are obtained for the two controllers. In Figure 11.16, attitude errors in roll, pitch and yaw axes are depicted. Figure 11.16 shows that peak attitude errors are attenuated in all three channels with C^{RP}. Next, to investigate the error signals further and to compare different controllers, spectral analysis is used. To analyze the performance improvement, cumulative power spectrum (CPS) of the error signals are used. CPS of attitude errors are computed and depicted in Figure 11.17.

In can be seen in Figure 11.17 that error components are mostly in the low frequency region. Errors around 7 Hz contribute only small portion of overall attitude errors. Therefore, controller satisfying sufficient robustness and having higher bandwidth can perform better. Similarly, controller satisfying sufficient robustness and having

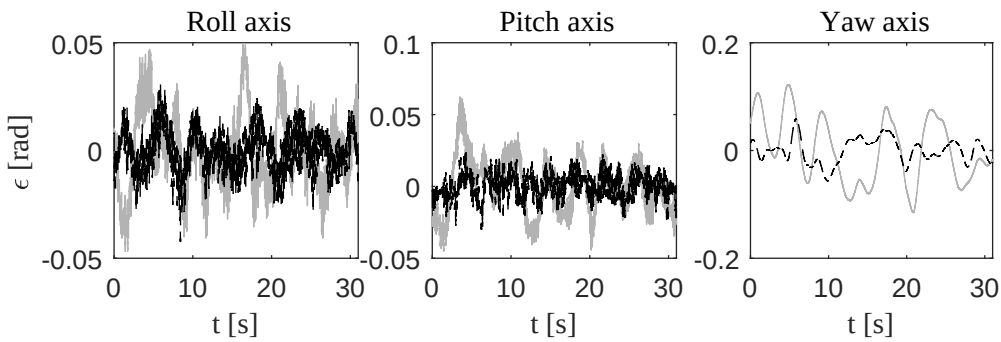

Figure 11.16: Hover test: Attitude errors in roll (left), pitch (center) and yaw (right): C^{exp} (solid gray), C^{RP} (dashed black).

higher gain in the low frequency region gives smaller error. These observations hold since error sources are mostly in the low frequencies. In addition, a controller which decouples the roll, pitch and yaw dynamics more accurately gives better performance. In this study, C^{RP} and C^{exp} have sufficient robustness. However, C^{RP} has higher gains in the low frequencies in roll and pitch axes as shown in Figure 11.13. In yaw axis, C^{RP} gives slightly higher bandwidth. More importantly, C^{RP} handles the roll and yaw axis coupling more accurately thanks to its multivariable structure. Therefore, as depicted in Figure 11.17, C^{RP} gives smaller attitude errors in all channels compared to C^{exp}.

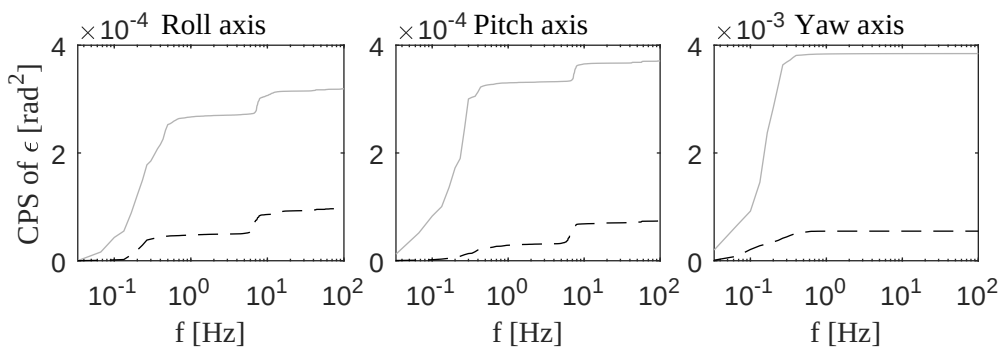

Figure 11.17: Hover test: Cumulative power spectrum of attitude errors in roll (left), pitch (center) and yaw (right): C^{exp} (solid gray), C^{RP} (dashed black).

Table 11.2: Hover test: Standard deviation of attitude errors ϵ in radian (degree):

Controller	σ_{roll}	σ_{pitch}	σ_{yaw}
C^{exp}	17.9×10^{-3} (1.02)	19.3×10^{-3} (1.1)	62.0×10^{-3} (3.55)
C^{RP}	9.9×10^{-3} (0.56)	8.6×10^{-3} (0.49)	23.4×10^{-3} (1.34)

Standard deviations of the attitude errors in hover are given in Table 11.2 for the two designed controllers. Percentage of the improvement changes based on wind condition that is present during hovering test. Three different tests are performed for each controller under similar environmental conditions. By investigating the average of three experiments given in Table 11.2, it can be said that standard deviation of attitude errors are reduced by a factor of 1.81 in roll, 2.24 in pitch and 2.65 in yaw axes. In view of these findings, attitude control performance is significantly improved with robust rate controller C^{RP} compared to PI rate controller C^{exp} when the vehicle is in hover.

In addition to reference tracking around hover, good disturbance rejection capability is also essential. Therefore, to analyze the disturbance rejection performance, a signal is injected at the plant input for each axis. This torque disturbance corresponds to 1/3 of the maximum available torque, i.e., $\Gamma_d = \Gamma_{\text{max}}/3$, for each axis. Similar to the previous case, attitude error $\epsilon = r_2 - y$ is selected for performance variable. In Figure 11.18, attitude errors in roll, pitch, yaw axes and torque disturbance injection points are illustrated. To analyze the disturbance rejection performance, standard deviations

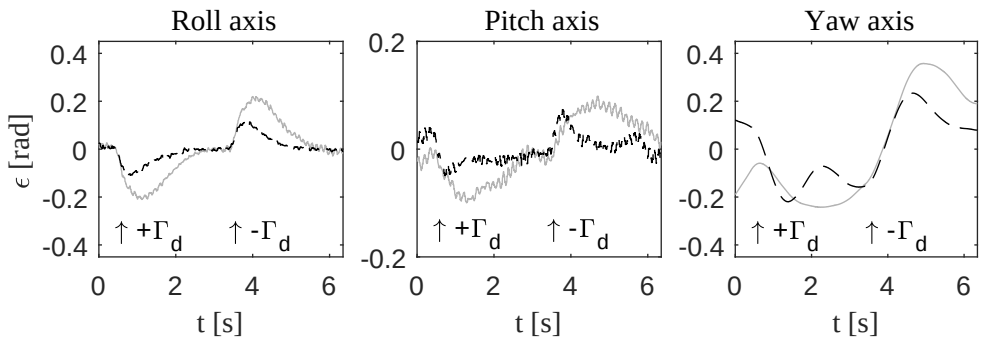

Figure 11.18: Disturbance rejection test: Attitude errors in roll (left), pitch (center) and yaw (right): C^{exp} (solid gray), C^{RP} (dashed black). See video [online].

Table 11.3: Disturbance rejection test: Standard deviation of attitude errors ϵ in radian (degree):

Controller	σ_{roll}	σ_{pitch}	σ_{yaw}
C^{exp}	0.1136 (6.51)	0.0571 (3.27)	0.2192 (12.56)
C^{RP}	0.048 (2.76)	0.025 (1.42)	0.14 (8.07)

of the attitude errors are used, and they are given in Table 11.3 for the two designed controllers. These results show that attitude errors are reduced by a factor of 2.36 in roll, 2.29 in pitch and 1.55 in yaw axes during disturbance rejection test. This test also illustrates that disturbance rejection performance is significantly improved with robust rate controller C^{RP} compared to PI rate controller C^{exp} around hover position.

11.4 Comments

In this chapter, attitude stabilization and torque disturbance rejection tests show that C^{RP} gives improved attitude control performance compared to C^{exp}. Herein, PI rate controller C^{exp} was tuned manually in flight to give sufficient command tracking performance. In addition, this controller also give sufficient robustness according to classical feedback control criteria. Phase loss due to finite bandwidth of motor speed control and gyro sensor delay does not allow any gain increase in this PI controller. In addition, PID controller is not used in this study to satisfy required roll-off to attenuate high frequency measurement noise. Therefore, extra lead and lag filters must be added to PI controller to enlarge the achieved bandwidths if classical control design method is used. Double PI can also be used to improve the performance if sufficient robustness is obtained. Similarly, notch filter may be required in the yaw channel. But they are not in the scope of this thesis. Herein, performances of commonly used standard PI controller and robust controller based on a robust-control-relevant model set are compared. This controller also shows multivariable characteristics in yaw axis. Therefore, roll and yaw axes coupling can be treated more accurately with C^{RP} compared to PI controller which is single variate.

CHAPTER 12

CONCLUSION

Unmanned aerial vehicles have gained popularity in the last two decades. Among all, quadrotors have been used in various military and civil applications. However, typical quadrotor has limited flight endurance due to high energy consumption. Therefore, alternative configurations have been investigated to increase the efficiency and hence flight endurance compared to a standard quadrotor. In this thesis, an uncommon quadrotor configuration is proposed for that purpose. This aerial vehicle has two big rotors on longitudinal axis to increase the efficiency and flight endurance. These large rotors carry most of the vehicle weight. Hence, small rotors are used on lateral axis to stabilize the attitude. Since alternate rotors are not counter rotating, yaw motion is controlled by extra inputs, i.e., by tilting these small rotors. In short, this uncommon configuration is designed to combine the mechanical simplicity of a quadrotor and efficiency of a tandem rotor helicopter.

Since this configuration is not common, flight control requires dynamical model of this vehicle. In Chapter 2, motion equations of this vehicle are derived for that purpose. In this study, aim is to use this vehicle at slow velocities around hover position. Therefore, a linear model can resemble the actual dynamics sufficiently around hover position. In Chapter 3, this linear model is obtained. Resulting model is statically decoupled using pseudoinverse based input decoupling (rotor mixing) matrix to simplify the flight dynamics. Next, control structures for attitude and position are explained.

System model and associated uncertainty are occasionally found by using system identification and model validation methods in flight control designs. On the contrary, model based on physical principles are frequently used. In this case, bounds on model parameters are widely used, and control designs should give sufficient performance under these parameter variations. But, required performance may not be

achieved with fixed controller if variations in these parameters are large. In that case, some parameters should be determined more accurately. Therefore, understanding which parameters mostly disturb the robust stability or performance is essential. In Chapter 4, structured singular value sensitivity analysis is introduced for that purpose. In addition, some of the parameters in the model are much more difficult to estimate. Maximum allowable uncertainty in these parameters for closed loop stability can also be calculated. This is mostly valuable in aerospace control applications where there are large uncertainties in the parameters, and identification tests are difficult and expensive. In Chapter 4, parameters of the uncommon quadrotor model are analyzed, and important ones in terms of robust stability are found. It is observed that when easily determined parameters are known more accurately, allowable uncertainties increase for the remaining parameters that are difficult to estimate.

The approximate linear model developed based on physical principles in Chapter 3 is ideal, and it does not include dynamics such as finite bandwidth of motor speed control and gyro sensor delay. Also, inexact decoupling of axes, flexible modes of the structure and uncertain parameters could not be handled properly with this ideal model. Therefore, a more accurate model of this vehicle in hover is derived by an identification method.

In aerospace applications, attitude control of vehicles should satisfy necessary robustness to cope with large uncertainties in the models and possible nonlinearities. Therefore, a robust control technique is used for attitude stabilization. When a robust control method is used, nominal model and uncertainty structure selections are very important to obtain high robust performance. In other words, uncertain model set should enable high robust performance. For that purpose, robust control objectives should be considered during system identification and uncertainty modeling. Robust-control-relevant identification discussed in Chapter 5 gives an uncertain model set which facilitates high performance robust control design. This method uses specific coprime factors in the dual-Youla-Kucera uncertainty structure. For that particular model, nominal model identification and quantification of model uncertainty together minimize the robust control criterion with respect to the uncertain model set. In this way, resulting control synthesis can be performed in a non-conservative manner, and similar high performance can be obtained for the entire model set.

Robust-control-relevant nominal model identification problem is usually ill-conditioned

for standard monomials. Therefore, parameters of nominal model can not be obtained accurately for this polynomial basis. For that reason, an alternative method is used to improve the numerical conditioning of the least squares problem. Using data-dependent orthonormal polynomials, optimally conditioned linear least squares problem is obtained as introduced in Chapter 6. By solving this problem, more accurate model is estimated compared to standard monomials. This estimate and orthonormal polynomials are also used in the subsequent Gaus-Newton iterations. Since resulting nonlinear least squares problem also remains close to optimal, accuracy of the estimate can be improved using Gaus-Newton algorithm.

Nominal model is parametrized in Chapter 5 and estimated in Chapter 6. But, this nominal model should be accompanied by minimum uncertainty to satisfy all available input output relations of the true system. In fact, this problem ill-posed since correctly allocating model residuals between perturbation and disturbance is not clear. This problem is solved by applying the validation-based uncertainty modeling procedure explained in Chapter 7. Therefore, minimum uncertainty is computed such that measured outputs from the true system and the uncertain model are consistent.

Visualization of an uncertain model set can be helpful to understand the control relevance of this set. For that purpose, method introduced in Chapter 8 is used.

In robust control methods, uncertain model and required robustness are already known before controller synthesis. However, standard μ synthesis optimizes robustness and performance at the same time. Therefore, this method is not suitable for problems where the required robustness is already known. Therefore, skewed-μ synthesis introduced in Chapter 9 is used for robust controller design.

In Chapter 2, theoretical model of the uncommon quadrotor configuration is introduced. Similarly, the first prototype is investigated both in hardware and software sides in Chapter 10. This prototype is used to test and verify the required flight functionalities of the proposed configuration.

When plant model is unknown, PID controller is usually preferred since it can be tuned manually by looking at system responses. In this study, PI rate controller is tuned manually in flight by investigating the command tracking performances of attitude control loops. Later, system model is estimated from flight tests when the quadrotor is stabilized by this controller as explained in Chapter 11. By evaluating the attitude rate loop constructed with manually tuned PI rate controller and estimated

model, sufficient gain and phase margins are obtained as disccussed in Chapter 11. Herein, phase loss due to finite bandwidth of motor speed control and gyro sensor delay does not allow any gain increase in this PI controller. Moreover, PID controller is not used to satisfy required roll-off to attenuate high frequency measurement noise. Therefore, extra lead and lag filters must be added to PI controller to enlarge the achieved bandwidths according to classical control design. If similar robustness can be obtained, double PI may improve the performance. Similarly, notch filter may be used for the yaw axis. But they are not in the scope of this thesis. Therefore, performances of standard PI controller and robust controller based on robust-control-relevant model set are compared in Chapter 11. As discussed previously, this uncertain model set enables non-conservative control design, and similar high performance can be obtained for all possible plants. Attitude stabilization and torque disturbance rejection performances are analyzed for these two controllers. Results of several flight experiments indicate that the designed robust controller improves the attitude control performance significantly compared to the standard PI controller. As explained in Chapter 11, the robust controller has double integral behavior in the low frequencies in roll and pitch axes. In yaw axis, the robust controller gives higher bandwidth. In addition, this controller has multivariable characteristics in yaw axis. Roll and yaw axes coupling can be treated more accurately in this case compared to single variate PI controller. These properties are the main reasons of performance improvement with the designed robust controller.

In conclusion, the proposed quadrotor configuration can be very useful over the conventional configuration, and it is worthy of further research. In addition, the robust control technique can be helpful to improve the performance achieved with common control methods.

In this thesis, an uncommon quadrotor configuration is introduced, and concept is proven experimentally using the prototype vehicle. Also, sufficient attitude control performance is obtained with the robust controller. But some parts require further attention. Firstly, efficiency of this vehicle should be calculated theoretically and compared with the standard case. Later, these results should be verified with experimental measurements. Secondly, battery powered large brushless DC motors should be replaced with gasoline engines to achieve significantly large flight endurance, and results of these two cases should be reported. Thirdly, system identification should

be performed more accurately by increasing the number of frequencies in the grid especially in the high frequency region. Frequency grid should also be constructed by considering dynamics of the system. Next, dynamics of rotor speed and tilt angle control should be included in the system model. Finally, aerodynamic effects and larger deviations from hover position should also be considered.

REFERENCES

[1] R. Mahony, V. Kumar, and P. Corke, "Multirotor aerial vehicles: Modeling, estimation, and control of quadrotor," *IEEE Robotics and Automation magazine*, vol. 19, no. 3, pp. 20–32, 2012.

[2] K. Karydis and V. Kumar, "Energetics in robotic flight at small scales," *Interface focus*, vol. 7, no. 1, p. 20160088, 2017.

[3] Y. Mulgaonkar, M. Whitzer, B. Morgan, C. M. Kroninger, A. M. Harrington, and V. Kumar, "Power and weight considerations in small, agile quadrotors," in *Micro-and Nanotechnology Sensors, Systems, and Applications VI*, vol. 9083, p. 90831Q, SPIE, 2014.

[4] S. Driessens and P. E. Pounds, "Towards a more efficient quadrotor configuration," in *2013 IEEE/RSJ International Conference on Intelligent Robots and Systems*, pp. 1386–1392, IEEE, 2013.

[5] G. Hoffmann, H. Huang, S. Waslander, and C. Tomlin, "Quadrotor helicopter flight dynamics and control: Theory and experiment," in *AIAA guidance, navigation and control conference and exhibit*, p. 6461, 2007.

[6] J. Du Plessis and P. E. Pounds, "Rotor flapping for a triangular quadrotor," in *ACRA*, 2014.

[7] S. Driessens and P. Pounds, "The triangular quadrotor: a more efficient quadrotor configuration," *IEEE Transactions on Robotics*, vol. 31, no. 6, pp. 1517–1526, 2015.

[8] T. Kim and S. Hong, "Control system design and experimental validation of hybrid multicopter for endurance enhancement," *Asia-pacific Journal of Modeling and Simulation for Mechanical System Design and Analysis (AJMSM)*, vol. 2, no. 1, pp. 15–20, 2017.

[9] A. Bondyra, S. Gardecki, P. Gasior, and W. Giernacki, "Performance of coaxial propulsion in design of multi-rotor uavs," in *International Conference on Automation*, pp. 523–531, Springer, 2016.

[10] T. Pang, K. Peng, F. Lin, and B. M. Chen, "Towards long-endurance flight: Design and implementation of a variable-pitch gasoline-engine quadrotor," in *2016 12th IEEE International Conference on Control and Automation (ICCA)*, pp. 767–772, IEEE, 2016.

[11] T. Haus, M. Orsag, and S. Bogdan, "Design considerations for a large quadrotor with moving mass control," in *2016 International Conference on Unmanned Aircraft Systems (ICUAS)*, pp. 1327–1334, IEEE, 2016.

[12] "Yeair." `https://yeair.de/`.

[13] S. Bouabdallah, A. Noth, and R. Siegwart, "Pid vs lq control techniques applied to an indoor micro quadrotor," in *2004 IEEE/RSJ International Conference on Intelligent Robots and Systems (IROS)(IEEE Cat. No. 04CH37566)*, vol. 3, pp. 2451–2456, IEEE, 2004.

[14] N. Michael, D. Mellinger, Q. Lindsey, and V. Kumar, "The grasp multiple micro-uav testbed," *IEEE Robotics & Automation Magazine*, vol. 17, no. 3, pp. 56–65, 2010.

[15] S. Bouabdallah and R. Siegwart, "Backstepping and sliding-mode techniques applied to an indoor micro quadrotor," in *Proceedings of the 2005 IEEE international conference on robotics and automation*, pp. 2247–2252, IEEE, 2005.

[16] H. Voos, "Nonlinear control of a quadrotor micro-uav using feedback-linearization," in *2009 IEEE International Conference on Mechatronics*, pp. 1–6, IEEE, 2009.

[17] G. V. Raffo, M. G. Ortega, and F. R. Rubio, "An integral predictive/nonlinear h_∞ control structure for a quadrotor helicopter," *Automatica*, vol. 46, no. 1, pp. 29–39, 2010.

[18] Y. Zhang, Z. Chen, X. Zhang, Q. Sun, and M. Sun, "A novel control scheme for quadrotor uav based upon active disturbance rejection control," *Aerospace Science and Technology*, vol. 79, pp. 601–609, 2018.

[19] S. Bouabdallah and R. Siegwart, "Full control of a quadrotor," in *2007 IEEE/RSJ International Conference on Intelligent Robots and Systems*, pp. 153–158, Ieee, 2007.

[20] M. Labbadi and M. Cherkaoui, "Robust adaptive backstepping fast terminal sliding mode controller for uncertain quadrotor uav," *Aerospace Science and Technology*, vol. 93, p. 105306, 2019.

[21] H. Liu, D. Li, J. Xi, and Y. Zhong, "Robust attitude controller design for miniature quadrotors," *International Journal of Robust and Nonlinear Control*, vol. 26, no. 4, pp. 681–696, 2016.

[22] L. Derafa, T. Madani, and A. Benallegue, "Dynamic modelling and experimental identification of four rotors helicopter parameters," in *2006 IEEE International Conference on Industrial Technology*, pp. 1834–1839, IEEE, 2006.

[23] J. C. Morris, M. Van Nieuwstadt, and P. Bendotti, "Identification and control of a model helicopter in hover," in *Proceedings of 1994 American Control Conference-ACC'94*, vol. 2, pp. 1238–1242, IEEE, 1994.

[24] W. Wei, M. B. Tischler, and K. Cohen, "System identification and controller optimization of a quadrotor unmanned aerial vehicle in hover," *Journal of the American Helicopter Society*, vol. 62, no. 4, pp. 1–9, 2017.

[25] T. Oomen and O. Bosgra, "System identification for achieving robust performance," *Automatica*, vol. 48, no. 9, pp. 1975–1987, 2012.

[26] T. Oomen and O. Bosgra, "Selecting uncertainty structures in identification for robust control with an automotive application," *IFAC Proceedings Volumes*, vol. 45, no. 16, pp. 601–606, 2012.

[27] T. Oomen, R. van Herpen, S. Quist, M. van de Wal, O. Bosgra, and M. Steinbuch, "Connecting system identification and robust control for next-generation motion control of a wafer stage," *IEEE Transactions on Control Systems Technology*, vol. 22, no. 1, pp. 102–118, 2014.

[28] M. Baskın and K. Leblebicioğlu, "Combined system identification and robust control of a gimbal platform," *Turkish Journal of Electrical Engineering & Computer Sciences*, vol. 29, no. 4, pp. 2247–2262, 2021.

[29] R. van Herpen, T. Oomen, and O. Bosgra, "Numerically reliable frequency-domain estimation of transfer functions: A computationally efficient methodology," *IFAC Proceedings Volumes*, vol. 45, no. 16, pp. 595–600, 2012.

[30] M. Baskın and K. Leblebicioğlu, "Robust control for line-of-sight stabilization of a two-axis gimbal system," *Turkish Journal of Electrical Engineering & Computer Sciences*, vol. 25, no. 5, pp. 3839–3853, 2017.

[31] T. Oomen and O. Bosgra, "Well-posed model uncertainty estimation by design of validation experiments," *IFAC Proceedings Volumes*, vol. 42, no. 10, pp. 1199–1204, 2009.

[32] J. C. Morris and M. P. Newlin, "Model validation in the frequency domain," in *Proceedings of 1995 34th IEEE Conference on Decision and Control*, vol. 4, pp. 3582–3587, IEEE, 1995.

[33] T. Luukkonen, "Modelling and control of quadcopter," *Independent research project in applied mathematics, Espoo*, vol. 22, 2011.

[34] A. Sanchez, J. Escareno, O. Garcia, and R. Lozano, "Autonomous hovering of a noncyclic tiltrotor uav: Modeling, control and implementation," *IFAC Proceedings Volumes*, vol. 41, no. 2, pp. 803–808, 2008.

[35] M. Ryll, H. H. Bülthoff, and P. R. Giordano, "A novel overactuated quadrotor unmanned aerial vehicle: Modeling, control, and experimental validation," *IEEE Transactions on Control Systems Technology*, vol. 23, no. 2, pp. 540–556, 2014.

[36] M. Elfeky, M. Elshafei, A.-W. A. Saif, and M. F. Al-Malki, "Modeling and simulation of quadrotor uav with tilting rotors," *International Journal of Control, Automation and Systems*, vol. 14, no. 4, pp. 1047–1055, 2016.

[37] J. P. Hespanha, *Linear systems theory*. Princeton university press, 2009.

[38] N. S. Özbek, M. Önkol, and M. Ö. Efe, "Feedback control strategies for quadrotor-type aerial robots: a survey," *Transactions of the Institute of Measurement and Control*, vol. 38, no. 5, pp. 529–554, 2016.

[39] X. Chen, *Flight controller design, automatic tuning and performance evaluation of quadrotor UAVs*. PhD thesis, RMIT University, 2017.

[40] G. Ferreres, *A practical approach to robustness analysis with aeronautical applications*. Kluwer Academic/Plenum Publishers, 1999.

[41] A. Marcos, D. Bates, and I. Postlethwaite, "Control oriented uncertainty modelling using μ sensitivities and skewed μ analysis tools," in *Proceedings of the 44th IEEE Conference on Decision and Control*, pp. 6436–6441, IEEE, 2005.

[42] K. Stahl Gunnarsson, J. Hansson, F. Karlsson, A. Hansson, and R. Wallin, "Clearance of flight control laws using linear fractional transformations," in *AIAA Guidance, Navigation, and Control Conference and Exhibit*, p. 4867, 2004.

[43] L. S. Brown and D. M. Bevly, "Allowable parametric uncertainty in the closed loop for the yaw-roll vehicle model: A skew-μ based approach," in *2017 American Control Conference (ACC)*, pp. 4309–4315, IEEE, 2017.

[44] L. Brown, *Determination of the Allowable Parametric Uncertainty in the Closed Loop Via a Skew-μ Based Technique with an Application to the Yaw-Roll Vehicle Model*. PhD thesis, Auburn University, 2017.

[45] M. Kuhn, Y. Ji, and D. Schrder, "Stability studies of critical dc power system component for more electric aircraft using μ sensitivity," in *2007 Mediterranean Conference on Control & Automation*, pp. 1–6, IEEE, 2007.

[46] K. Zhou, J. C. Doyle, K. Glover, *et al.*, *Robust and optimal control*, vol. 40. Prentice hall New Jersey, 1996.

[47] P. Lambrechts, J. Terlouw, S. Bennani, and M. Steinbuch, "Parametric uncertainty modeling using lfts," in *1993 American Control Conference*, pp. 267–272, IEEE, 1993.

[48] M. Steinbuch and M. L. Norg, "Advanced motion control: An industrial perspective," *European Journal of Control*, vol. 4, no. 4, pp. 278–293, 1998.

[49] T. Oomen and M. Steinbuch, "Model-based control for high-tech mechatronic systems," in *Mechatronics and Robotics*, pp. 51–80, CRC Press, 2020.

[50] R. Braatz and M. Morari, "μ-sensitivities as an aid for robust identification," in *1991 American Control Conference*, pp. 231–236, IEEE, 1991.

[51] S. Skogestad and I. Postlethwaite, *Multivariable feedback control: analysis and design*, vol. 2. Wiley New York, 2007.

[52] R. D. Braatz, P. M. Young, J. C. Doyle, and M. Morari, "Computational complexity of μ calculation," *IEEE Transactions on Automatic Control*, vol. 39, no. 5, pp. 1000–1002, 1994.

[53] P. M. Young, "Structured singular value approach for systems with parametric uncertainty," *International Journal of Robust and Nonlinear Control: IFAC-Affiliated Journal*, vol. 11, no. 7, pp. 653–680, 2001.

[54] C. Roos, "Systems modeling, analysis and control (smac) toolbox: An insight into the robustness analysis library," in *2013 IEEE Conference on Computer Aided Control System Design (CACSD)*, pp. 176–181, available with the SMAC toolbox at http://w3.onera.fr/smac/smart, IEEE, 2013.

[55] T. Oomen and M. Steinbuch, "Identification for robust control of complex systems: Algorithm and motion application," *Control-oriented modelling and identification: theory and applications, IET*, 2015.

[56] T. Oomen, R. van Herpen, and O. Bosgra, "Robust-control-relevant coprime factor identification with application to model validation of a wafer stage," *IFAC Proceedings Volumes*, vol. 42, no. 10, pp. 1044–1049, 2009.

[57] R. A. De Callafon and P. M. Van den Hof, "Suboptimal feedback control by a scheme of iterative identification and control design," *Mathematical modelling of systems*, vol. 3, no. 1, pp. 77–101, 1997.

[58] R. J. Schrama, "Accurate identification for control: The necessity of an iterative scheme," *IEEE Transactions on automatic control*, vol. 37, no. 7, pp. 991–994, 1992.

[59] P. M. Van Den Hof and R. J. Schrama, "Identification and control—closed-loop issues," *Automatica*, vol. 31, no. 12, pp. 1751–1770, 1995.

[60] C.-C. Chu, "On discrete inner-outer and spectral factorizations," in *1988 American Control Conference*, pp. 1699–1700, IEEE, 1988.

[61] J. R. Rice and K. H. Usow, "The lawson algorithm and extensions," *Mathematics of Computation*, vol. 22, no. 101, pp. 118–127, 1968.

[62] T. Oomen and O. Bosgra, "Robust-control-relevant coprime factor identification: A numerically reliable frequency domain approach," in *2008 American Control Conference*, pp. 625–631, IEEE, 2008.

[63] J. Brewer, "Kronecker products and matrix calculus in system theory," *IEEE Transactions on circuits and systems*, vol. 25, no. 9, pp. 772–781, 1978.

[64] R. A. de Callafon, D. de Roover, and P. M. Van den Hof, "Multivariable least squares frequency domain identification using polynomial matrix fraction descriptions," in *Proceedings of 35th IEEE Conference on Decision and Control*, vol. 2, pp. 2030–2035, IEEE, 1996.

[65] C. Sanathanan and J. Koerner, "Transfer function synthesis as a ratio of two complex polynomials," *IEEE transactions on automatic control*, vol. 8, no. 1, pp. 56–58, 1963.

[66] M. Van Barel and A. Bultheel, "Orthonormal polynomial vectors and least squares approximation for a discrete inner product," *Electronic Transactions on Numerical Analysis*, vol. 3, pp. 1–23, 1995.

[67] A. Bultheel and M. Van Barel, "Vector orthogonal polynomials and least squares approximation," *SIAM Journal on Matrix Analysis and Applications*, vol. 16, no. 3, pp. 863–885, 1995.

[68] T. Oomen, *System identification for robust and inferential control: with applications to ILC and precision motion systems*. PhD thesis, Eindhoven University of Technology, 2010.

[69] R. van Herpen, *Identification for control of complex motion systems: optimal numerical conditioning using data-dependent polynomial bases*. PhD thesis, Eindhoven University of Technology, 2014.

[70] R. Voorhoeve, *Identification for advanced motion control: numerically reliable algorithms for complex systems*. PhD thesis, Eindhoven University of Technology, 2018.

[71] L. Reichel, G. Ammar, and W. Gragg, "Discrete least squares approximation by trigonometric polynomials," *Mathematics of Computation*, vol. 57, no. 195, pp. 273–289, 1991.

[72] R. Voorhoeve, R. de Rozario, and T. Oomen, "Identification for motion control: Incorporating constraints and numerical considerations," in *2016 American Control Conference (ACC)*, pp. 6209–6214, IEEE, 2016.

[73] D. S. Bayard, "High-order multivariable transfer function curve fitting: Algorithms, sparse matrix methods and experimental results," *Automatica*, vol. 30, no. 9, pp. 1439–1444, 1994.

[74] R. S. Smith and J. C. Doyle, "Model validation: A connection between robust control and identification," *IEEE Transactions on automatic control*, vol. 37, no. 7, pp. 942–952, 1992.

[75] M. P. Newlin and R. S. Smith, "A generalization of the structured singular value and its application to model validation," *IEEE Transactions on Automatic Control*, vol. 43, no. 7, pp. 901–907, 1998.

[76] T. Oomen and O. Bosgra, "Estimating disturbances and model uncertainty in model validation for robust control," in *2008 47th IEEE Conference on Decision and Control*, pp. 5513–5518, IEEE, 2008.

[77] F. Paganini and J. Doyle, "Analysis of implicitly defined systems," in *Proceedings of 1994 33rd IEEE Conference on Decision and Control*, vol. 4, pp. 3673–3678, IEEE, 1994.

[78] J. Doyle, M. Newlin, F. Paganini, and J. Tierno, "Unifying robustness analysis and system id," in *Proceedings of 1994 33rd IEEE Conference on Decision and Control*, vol. 4, pp. 3667–3672, IEEE, 1994.

[79] A. Packard and J. Doyle, "The complex structured singular value," *Automatica*, vol. 29, no. 1, pp. 71–109, 1993.

[80] R. Pintelon and J. Schoukens, *System identification: a frequency domain approach*. Wiley-IEEE Press, 2012.

[81] E. Grassens, "System identification for robust inferential control applied to a prototype motion system," Master's thesis, Eindhoven University of Technology, 2010.

[82] M. Crowder and R. de Callafon, "Coprime factor perturbation models for closed-loop model validation techniques," *IFAC Proceedings Volumes*, vol. 36, no. 16, pp. 519–524, 2003.

[83] T. Oomen, S. Quist, R. van Herpen, and O. Bosgra, "Identification and visualization of robust-control-relevant model sets with application to an industrial wafer stage," in *49th IEEE Conference on Decision and Control (CDC)*, pp. 5530–5535, IEEE, 2010.

[84] M. K. Fan and A. L. Tits, "A measure of worst-case h∞ performance and of largest acceptable uncertainty," *Systems & Control Letters*, vol. 18, no. 6, pp. 409–421, 1992.

[85] G. J. Balas, J. C. Doyle, K. Glover, A. Packard, and R. Smith, "μ-analysis and synthesis toolbox," *MUSYN Inc. and The MathWorks, Natick MA*, 1993.

[86] "Px4 autopilot user guide." `https://docs.px4.io/master/en/index.html`.

[87] "Copter home." `https://ardupilot.org/copter/index.html`.

[88] T. Oomen and S. van der Meulen, "High performance continuously variable transmission control through robust control-relevant model validation," *Journal of Dynamic Systems, Measurement, and Control*, vol. 135, no. 6, 2013.

[89] J. A. Karl and H. Tore, "Pid controllers: theory, design, and tuning," *Instrument Society of America, North Carolina*, 1995.

[90] O. H. Bosgra, H. Kwakernaak, and G. Meinsma, "Design methods for control systems," *Notes for a Course of the Dutch Institute of Systems and Control, Winter term*, 2007.

[91] D. McFarlane and K. Glover, "A loop-shaping design procedure using h_∞ synthesis," *IEEE transactions on automatic control*, vol. 37, no. 6, pp. 759–769, 1992.

[92] K. Glover and D. McFarlane, "Robust stabilization of normalized coprime factor plant descriptions with h∞-bounded uncertainty," *IEEE transactions on automatic control*, vol. 34, no. 8, pp. 821–830, 1989.

CURRICULUM VITAE

PERSONAL INFORMATION

Surname, Name: Baskın, Mehmet

EDUCATION

Degree	Institution	Year of Graduation
MS	METU Electrical and Electronics Engineering	2015
BS	METU Electrical and Electronics Engineering	2013

PUBLICATIONS

M. Baskın and K. Leblebicioğlu, "Combined system identification and robust control of a gimbal platform," *Turkish Journal of Electrical Engineering & Computer Sciences*, vol. 29, no. 4, pp. 2247–2262, 2021.

M. Baskın and K. Leblebicioğlu, "Robust control for line-of-sight stabilization of a two-axis gimbal system," *Turkish Journal of Electrical Engineering & Computer Sciences*, vol. 25, no. 5, pp. 3839–3853, 2017.